ERL17

The 59th ICFA Advanced Beam Dynamics Workshop on Energy Recovery Linacs

18 - 23 June 2017
CERN, Geneva, Switzerland

SPC Chair : Oliver Brüning *(CERN)*

WG1 : ERL injectors (Gun/Cathode/Laser) : Kurt Aulenbacher *(Uni Mainz)*, Erdong Wang *(BNL)*

WG2 : ERL Optics, beam dynamics and instrumentation : Daniel Schulte *(CERN)*, Alex Bogacz *(JLAB)*

WG3 : Test Facilities around the world : Georg Hoffstaetter *(Cornell)*, Achille Stocchi *(LAL)*

WG4 : Superconducting RF : Ilan Ben-Zvi *(BNL)*, Frank Gerigk *(CERN)*

WG5 : Applications : Ivan Konoplev *(ADAMS)*, Peter McIntosh *(STFC)*

For more information please contact: erl17@cern.ch
www.cern.ch/ERL17

International Organizing Committee :

Erk Jensen *(CERN), ERL17 Chair*
Sergey Belomestnykh *(FNAL)*
Stephen Benson *(JLab)*
Ilan Ben-Zvi *(BNL/SBU)*
Ryoichi Hajima *(QST)*
Georg Hoffstaetter *(Cornell)*
Hiroshi Kawata *(KEK)*
Kwang-Je Kim *(ANL & U. of Chicago)*
Jens Knobloch *(HZB)*
Gennady N. Kulipanov *(BINP)*
Kexin Liu *(Peking U.)*
Elias Metral *(CERN)*
Susan Smith *(STFC/DL/ASTeC)*

Local Organizing Committee :

Laurie Hemery *(CERN), ERL17 LOC Chair*
Sergey Belomestnykh *(FNAL)*
Ilan Ben-Zvi *(BNL)*
Oliver Brüning *(CERN), SPC Chair*
Nuria Catalan Lasheras *(CERN)*
Mick Draper *(CERN)*
Erk Jensen *(CERN), Chair*
Hervé Martinet *(CERN)*
Elias Metral *(CERN)*
Sotirios Papadopoulos *(CERN)*
Suitbert Ramberger *(CERN), Editor*

ICFA

CERN

Contents

Workshop Chair

Erk Jensen   CERN

Scientific Program Committee (SPC)

Oliver Brüning	CERN, SPC Chair	Ivan Konoplev	ADAMS
Nuria Catalan-Lasheras	CERN, SPC Secretary	Vladimir Litvinenko	SBU/BNL
Michael Abo-Bakr	HZB	Kexin Liu	Peking U.
Andre Arnold	HZDR	Chris Mayes	Cornell
Kurt Aulenbacher	Mainz U.	Peter Macintosh	STFC
Ivan Bazarov	Cornell	Nobuyuki Nishimori	Tohoku U.
Ilan Ben-Zvi	BNL	Takashi Obina	KEK
Alex Bogacz	JLAB	Vadim Ptitsyn	BNL/SBU
Andrew Burrill	SLAC	Hiroshi Sakai	KEK
Dave Douglas	JLab	Daniel Schulte	CERN
Bruce Dunham	SLAC	Achille Stocchi	LAL
Frank Gerigk	CERN	Nikolay Vinokurov	BINP
Georg Hoffstaetter	Cornell	Jiuqing Wang	IHEP
Dmitry Kayran	BNL	Erdong Wang	BNL
Thorsten Kamps	HZB		

International Organizing Committee (IOC)

Erk Jensen	CERN, ERL17 Chair
Sergey Belomestnykh	FNAL
Stephen Benson	JLab
Ilan Ben-Zvi	BNL/SBU
Ryoichi Hajima	QST
Georg Hoffstaetter	Cornell
Hiroshi Kawata	KEK
Kwang-Je Kim	ANL & U. of Chicago
Jens Knobloch	HZB
Gennady N. Kulipanov	BINP
Kexin Liu	Peking U.
Elias Metral	CERN
Susan Smith	STFC/DL/ASTeC

Local Organizing Committee (LOC)

Laurie Hemery	CERN, ERL17 LOC Chair
Sergey Belomestnykh	FNAL
Ilan Ben-Zvi	BNL
Oliver Brüning	CERN, SPC Chair
Nuria Catalan Lasheras	CERN, SPC Secretary
Mick Draper	CERN, Editor
Erk Jensen	CERN, Chair
Hervé Martinet	CERN
Elias Metral	CERN
Sotirios Papadopoulos	CERN
Suitbert Ramberger	CERN, Editor

DEVELOPMENT OF SRF GUN APPLYING NEW CATHODE IDEA USING A TRANSPARENT SUPERCONDUCTING LAYER

T. Konomi[†], Y. Honda, E. Kako, Y. Kobayashi, S. Michizono, T. Miyajma, H. Sakai, K. Umemori, S.Yamaguchi, M.Yamamoto, KEK, Tsukuba, Japan

R. Matsuda, Mitsubishi Heavy Industries, Ltd. Takasago, Japan

T. Yanagisawa, Mitsubishi Heavy Industries Mechatronic Systems, Ltd., Kobe, Japan

Abstract

KEK has been developing a superconducting RF gun for CW ERL since 2013. The SRF gun is a combination of a 1.3 GHz, 1.5-cell superconducting RF cavity and a backside excitation type photocathode. The photocathode consists of transparent substrate $MgAl_2O_4$, transparent superconductor $LiTi_2O_4$ and bi-alkali photocathode K_2CsSb. The reason for using transparent superconductor is to reflect RF by using the feature of penetration depth of superconductor, which is defined from London equation. It protects optical components from RF damage. The critical DC magnetic field of the cathode, quantum efficiency and initial emittance were measured. These show the cathode can be used for the SRF gun. The gun cavity was designed to satisfy the photocathode operation. Eight vertical tests of the gun cavity have been performed. The surface peak electric field reaches to 75 MV/m with the dummy cathode rod which was made of bulk niobium.

INTRODUCTION

The SRF gun is a key device for the future linac base electron accelerator. KEK start a SRF gun development for KEK 3 GeV ERL project [1]. We apply the backside excitation scheme. There are two advantages. One is RF and beam line structures are simpler than conventional design using metal substrate photocathode. It is not necessary to bend the excitation laser or electron beam trajectory so as not to overlap each other as compared with the front excitation. Second advantage is that the excitation laser is able to be controlled more precisely and increase the pointing stability by using short focal length lenses. It helps the space charge effect compensation.

PHOTOCATHODE IDEA

In order to develop the back side excitation photocathode, it is necessary to use a transparent substrate such as sapphire glass. However SiC and GaN substrate seems to be difficult to operate in a high RF voltage because breakdown field is 3.5 MV/cm [2]. And RF leakage to back side of the photocathode is a risk of damaging a light fibre and lens mounted at the back of the photocathode. The photocathode substrate should have the metallic properties to reflect the RF in order not to reduce the electric field on the photocathode. It increases the initial electric gradient at low beam energy and suppresses the space charge effect.

We propose a photocathode using a transparent superconductor (Fig.1). It is suit to the superconducting technology. A transparent superconductor $LiTi_2O_4$ can block the RF leakage and transmit the excitation visible light at the same time [3]. RF penetration depth of superconductor is defined by London penetration depth. It is about several tens of nanometers. $LiTi2O4$ is an epitaxial thin film deposited by pulsed laser deposition on $MgAl_2O_4$ (111). The transition temperature is about 12 K. The transmittance is about 70% at a wavelength of 477 nm. The lattice constant is 0.8405 nm. It is close to the famous photocathode surface K_2CsSb (0.861 nm) [4].
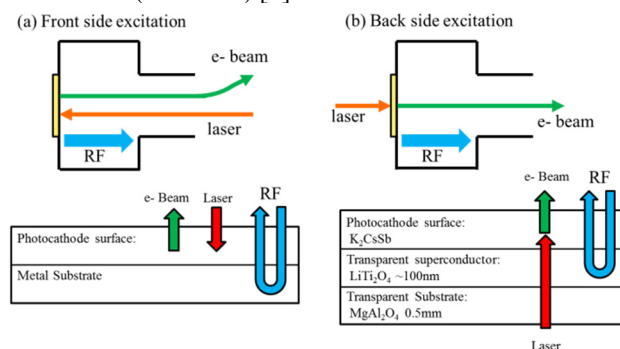
Figure 1: Front and back side excitation type photocathode structure. (a) Conventional method using metal substrate. (b) Transparent photocathode using a transparent superconductor.

SRF GUN CAVITY PERFORMANCE

The superconductor used in the photocathode needs to be cooled down. The SRF gun cavity also operates at 2 K. an effective cathode cooling system could be designed. MHI and KEK designed the KEK SRF gun #1 to test the maximum electric field and Q value [5]. It consists of 1.5 accelerating elliptical cells, choke cell and cathode plug. First cells are designed with the cathode cell to test. The accelerating cell shape was designed to minimize the energy spread and emittance by adjusting the cell taper angle. Table 1 shows the parameters of the KEK SRF gun #1. Target Q values are estimated from ILC target. Peak electric and magnetic field located on accelerating cell. On the photocathode, maximum electric field is 70% of the peak electric field of the accelerating cell and maximum magnetic field is 3.3 mT.

Figure 2 shows the KEK SRF gun #1. High gradient tests were done with dummy cathode plug, which was shaved out from bulk niobium and doesn't have the cathode mount structure. The cathode plug cleaning is important to

MOIACC002

achieve high gradient. Figure 3 shows the vertical test with and without high pressure rinsing (HPR) after mounting the dummy cathode plug. The peak surface electric field reached 75 MV/m and X-ray couldn't be observed with HPR. We understood it is important to ultra-clean the head of the dummy cathode plug up. However HPR should not apply to the transparent superconductor cathode substrate because it is very thin and delicate. We have to search other method for cleaning for example hydrogen cleaning or sputtering.

Table 1: KEK SRF gun #1 parameters

Parameter	Value
Beam energy	2 MeV
Project emittance	0.6 π mm. mrad
Project energy spread	0.09% (1.84 keV)
Peak electric field	41.9 MV/m
Peak magnetic field	95.2 mT
RF phase	55°
Geometrical factor	135.6 Ω
Target surface resistance	30 nΩ
Target Q value	4.5×10^9
Target cavity loss	8 W
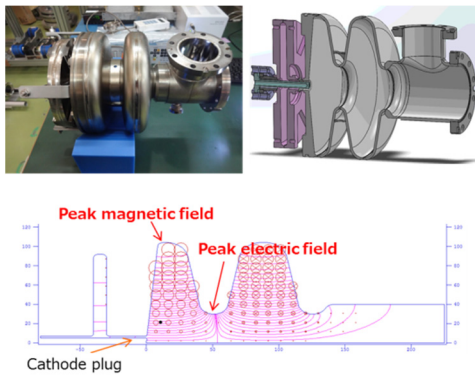
Figure 2: KEK SRF gun #1
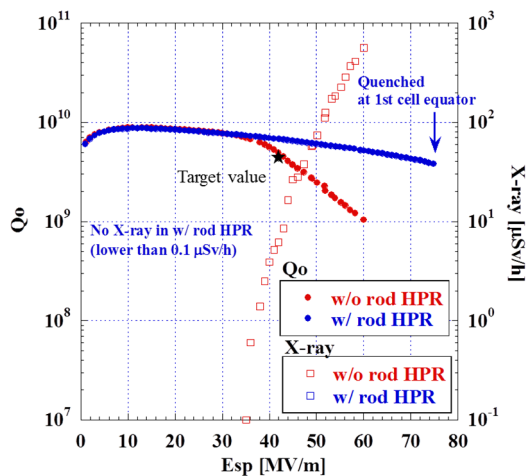
Figure 3: Vertical test results.

PHOTOCATHODE DEVELOPMENT

The practical performance of the photocathode using transparent superconductor was evaluated by measuring the quantum efficiency, initial emittance and critical DC magnetic field.

Deposition and Quantum Efficiency

The photocathode evaporation chamber has SAES cesium, SAES potassium and bulk antimony evaporation sources. The photocathode substrates are heated and cleaned at 500 $^\circ$C, 3 hours before deposition. The photocathode temperature stays about 100 $^\circ$C during deposition. Excitation laser and xenon lamp can inject from front and back side of the photocathode. The chamber vacuum is $6\times10^{-8}\sim1\times10^{-7}$ Pa during the deposition. Base pressure is 1×10^{-8} Pa.

Typical evaporation procedure is following. First, deposit antimony 10 nm at 150 $^\circ$C. The thickness was measured by quartz crystal micro balance and transparent efficiency of 405 nm laser. Then, deposit potassium at 120 $^\circ$C until observing the maximum quantum efficiency. Finally, deposit caesium at 100 $^\circ$C until observing the maximum quantum efficiency. We achieved 7% quantum efficiency at 405 nm.

Figure 4 shows the quantum efficiency changes during the cooling to 6.7K. The photocathode substrate is SiTiO$_3$. K$_2$CsSb deposition procedure discussed above. The initial quantum efficiency is 10% with 405 nm laser at room temperature. The cooling chamber pressure is 3.6×10^{-8} Pa. This quantum efficiency is not reversible manner with temperature. We supposed residual gas absorbed photocathode surface and increase the surface work function. Further study of photocathode performance at cryogenic temperatures and ways to improve this performance is essential for the photocathode development.
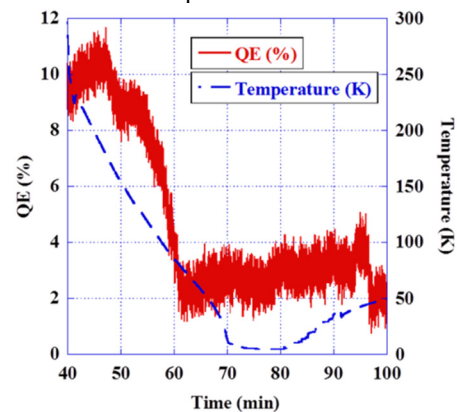
Figure 4: Changes of quantum efficiency during cooling down.

Initial Emittance

The initial emittance is measured based on the LBNL method [6]. The laser spot size is smaller than the beam size at far from parallel plate DC gun. Emittance can be measured from the beam divergent angle.

Figure 5 shows the initial emittance at room temperature. The energy threshold of the photocathode is 1.85±0.15e V.

The initial emittance with 405 nm is larger than with 532 nm laser. It agrees with the theoretical value. Figure 6 shows the temperature dependence of the initial emittance with 405 nm laser. The measurement temperature is room temperature and 6.7K. Quantum efficiency decreased during the cooling down. 532 nm laser couldn't emit enough electrons. 6.7 K initial emittance is smaller than room temperature. It is not enough to prove the temperature dependence because the threshold energy is not measured. Considering the emittance difference between room temperature and 6.7K is 0.02 µrad /mm by the theory. There is no contradiction in the measurement result.
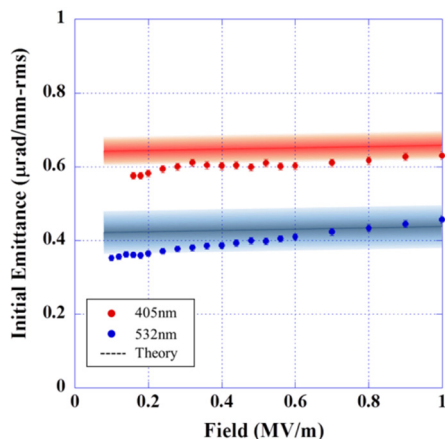
Figure 5: Initial emittance measured with 405 nm and 532 nm laser.
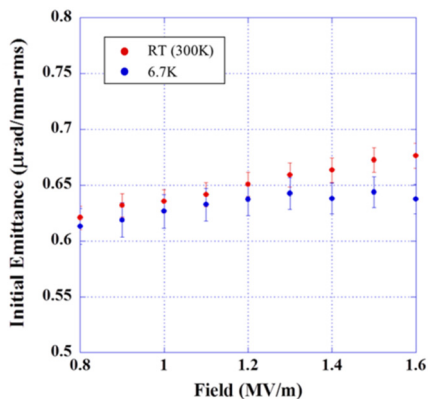
Figure 6: Temperature dependence of the initial emittance with 405 nm

Critical DC Magnetic Field

Both the transparent superconductor and bi-alkali photocathode use the alkali metal. We are concerned the change of superconducting properties after K_2CsSb deposition. Figures 7 and 8 show the critical temperature and lower critical magnetic field before and after K_2CsSb deposition. They were measured by magnetic property measurement system (MPMS-7) (Quantum design, Inc.). The transition temperature is 11.4K. The lower critical temperature is 9.5 mT at 2K. Although they are slightly decreased than before deposition, they satisfy the use condition in KEK-SRF gun usage.
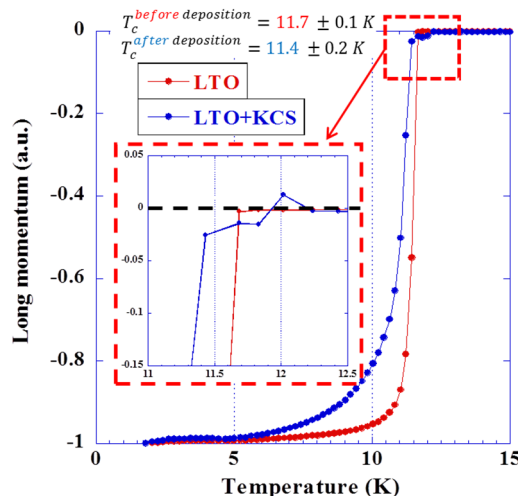
Figure 7:Transition temperature
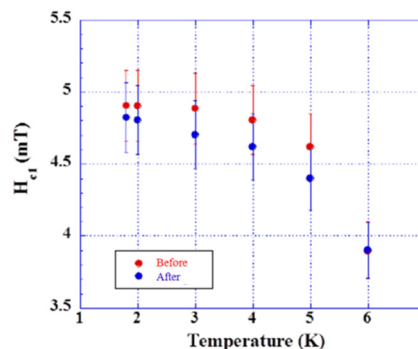
Figure 8: Lower critical magnetic field

SUMMARY AND FUTURE PLANS

KEK starts SRF gun development using the transparent superconductor. The gun cavity and photocathode have been developed individually. The surface peak electric field reached 75 MV/m which is about twice the target value. Although the photocathode critical magnetic field is enough higher than target value, it has many problems for practical use. Further study at cryogenic temperatures and ways to improve this performance is essential for SRF gun development. We will develop the KEK SRF gun #2 and new cathode deposition chamber for evaluating the photocathode in RF condition and beam parameter.

REFERENCES

[1] ERL Conceptual Design Report, KEK Report 2012-4 (2012)
[2] M.Golio, RF and Microwave Semiconductor Device Handbook, CRC Press, 2013.
[3] A. Kumatani et al, Appl. Phys. Lett. 101, 123103 (2012)
[4] Li Xu-Dong et al, Chinese Physics, Letter vol.30 (2013).
[5] R.Matsuda et al., Proc. of the 11th Annual Meeting of Particle Accelerator Society of Japan, MOOL13, (2014).
[6] T. Vecchione et al, APL. 99, 034103 (2011).

MOIACC002

INVESTIGATION OF K$_2$CsSb PHOTOCATHODES *

V. Bechthold[†], K. Aulenbacher, M.A. Dehn, S. Friederich

Institut für Kernphysik, Johannes Gutenberg Universität-Mainz, Germany

Abstract

The interest in multi alkali antimonide photocathodes, e.g. K$_2$CsSb, for future ERL projects like BERlinPRO (Berlin Energy Recovery Linac Prototype) and MESA (Mainz Energy-Recovering Superconducting Accelerator) has grown in recent years. In particular for the case of RF-sources the investigation of the time response is of great importance.

In Mainz we are able to synthesize these kinds of photocathodes and investigate their pulse response at 1 picosecond level using a radio frequency streak method. We present on the one hand the cathode plant which is used for synthesizing the multi alkali antimonide photocathodes and on the other hand first measurements showing pulse responses of K$_2$CsSb at $\lambda = 400$ nm laser wavelength. Furthermore, an analyzing chamber has been installed, which allows investigation of lifetime under laser heating and in-situ measurements of the work function using a UHV Kelvin Probe.

INTRODUCTION

High average brightness beam applications all need a photocathode with high QE, long lifetime, low emittance and fast response. If no spin polarization is needed, these figures of merit all may be fulfilled by the group of (multi) alkali antimonide cathodes [1].

Having PEA (Positive Electron Affinity) conditions, the nature of these cathodes promises to have a faster response time ($10^{-13} < \tau < 10^{-12}$ s) than NEA (Negative Electron Affinity) cathodes like Cs(O):GaAs because the average electron energy is thermalized quickly below the energy threshold for photoemission [2]. Besides the commonly investigated FWHM or RMS pulse response, we present measurements of the longitudinal tail of these cathodes. Such tails could be generated for instance by temporal trapping in localized electronic states inside the cathode, which may lead to a delayed response albeit at very low intensity levels. High current machines have to minimize this effect to be able to run without damage or high radioactivity.

Fast response for alkali antimonides has been shown to be compatible with < 1 ps response of a Cs$_3$Sb cathode at an instrumental resolution of $\sigma = 2$ ps [3]. Our results below will confirm this for a K$_2$CsSb cathode at a improved resolution of $\sigma \approx 1$ ps. Monte Carlo simulations indicate a sub-ps response [4].

Time response measurements have been carried out at the MAMI (Mainzer Mikroton) test source PKAT (Polarisierte Kanone Test) successfully for a long time [5], [6]. During the last years, we have improved the ability for measuring long tails of the initial bunch at a high dynamic range [7].

It is difficult to manage the purchase and transport of alkali antimonides under vacuum if a commercial vendor is part of the process. We have therefore decided to synthesize the cathodes in our own lab, a similar decision has also been made by others groups, e.g. [8], [9]. Therefore, a separate cathode preparation chamber, the cathode plant, has been commissioned in Mainz with the goal to qualify cathodes for our ERL project MESA.

Since the generation of 10 mA average currents needs considerable laser intensities, we have additionally investigated the effects of laser induced cathode heating.

EXPERIMENTAL SET-UP

Photocathode Plant

UHV is essential for the cathode growing process. Semiconductor photocathodes are very sensitive tow water and oxygen; therefore, we use an combination of IGP (GammaVacuum TiTan300T) and a NEG Pump (SAES CapaciTorr). Baking out is limited to 150 °C due to the used AlfaVakuo (formerly Alvatec) dispensers, which contain an indium sealing protecting the alkali alloy from handling in air. As residual gas should not contaminate the alloy during baking, the indium sealing must not melt.

An RGA (Dycor LC-D 200) and a Bayard-Alpert gauge (Vacom Atmion) control the pressure conditions. Vacuum in the low $p = 1 \times 10^{-10}$ mbar range can be achieved with H$_2$ as the dominating gas. During potassium evaporation the pressure rises to 5×10^{-8} mbar, $p(\text{H}_2\text{O})$ and $p(\text{O}_2)$ are in the 5×10^{-11} mbar region. Vacuum conditions for cesium and antimony steps are even better.

Partial pressure of antimony and the alkalis cannot be detected with the RGA during evaporation. Therefore, a thickness monitor (LewVac) is essential for providing information about the metal flux.

In the present set-up, further information on the status of the growth process can only be inferred from the photo electron yield. Due to budget restrictions, equipment yielding structural information of the deposited layer like XPS has not been purchased so far.

Figure 1 shows a schematic inner view of the preparation chamber. K$_2$CsSb photocathodes are synthesized by sequential deposition mainly after the classical recipe of Sommer [10] beginning with a thin antimony film on a metal substrate reacting with K and Cs vapor at an elevated temperature.

The substrate is positioned in a MAMI standard cathode holder (puck). Its position can be changed by a UHV manipulator. The crystal wheel allows storage of eight different pucks, in practice up to four pucks are used.
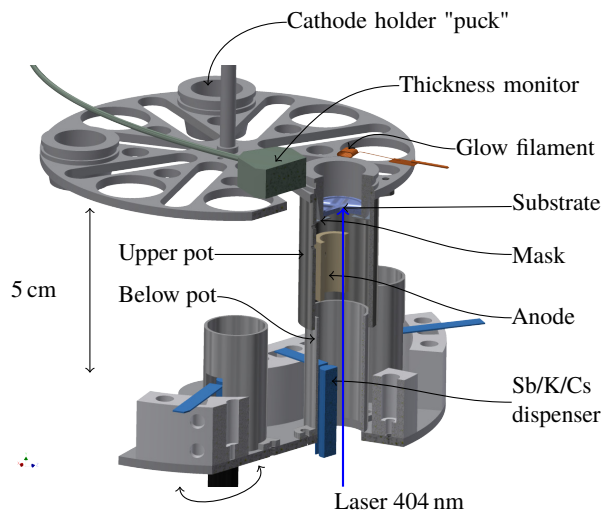
Figure 1: Schematic inner view of the cathode plant. The two stacked pots should prevent a coating of the whole chamber.

A glow filament (OSRAM 64663 HLX) heats the substrate from a distance of ≈ 15 mm.

We have used SUS (Steel Special Use Stainless), Mo, Cu, GaAs as substrate materials so far, achieving highest QE with SUS. At a distance of ≈ 5 cm V-shaped AlfaSources are mounted, the needed flux is adjusted and controlled via thickness monitor.

QE is measured in reflective mode using a blue laser diode (Thorlabs CPS405, $P = 4.7$ mW) illuminating through a window below the glow filament position.

The typical procedure is

- cleaning the substrate with high temperature (> 300 °C) at least 1 h

- deposition of 10 nm − 20 nm Sb

- deposition of K until QE reaches a plateau

- deposition of Cs until QE reaches a plateau

Spectral Response

Using a cold (Thorlabs LEDWE-15) and a warm white LED (CREE XP-L U2) with bandpass filter allows a cheap, fast and easy set-up for a spectral response measurement. QE for the major values of the interesting wavelength spectrum (450-650 nm) can be determined, see Fig. 4. Using an iris and two lenses (concave and convex), the beam spot can be focused to a diameter of 3 mm achieving power values (9- 35 µW) which are sufficient to get a photo electron yield.

Lifetime Measurements

Two lifetime conditions have been investigated: The first one is the vacuum lifetime, which is expected to be months or even years if vacuum conditions are stable and no charge is extracted from the cathode. For the second condition, one has to consider that the MESA source will be operated with

currents exceeding 10 mA, which requires laser intensities of the order 1 W. Cathode lifetime must not be shortened by this intensity. Otherwise, the decrease of lifetime will be accelerated due to the necessity of increasing the laser power to keep the current constant. This would quickly lead to the collapse of QE. We therefore have investigated the lifetime under relevant laser powers.

For these investigations, an additional UHV analyzing chamber has been added to the cathode plant. Additionally an EPICS based control system has been commissioned. It controls the experiment in the following way: A large heating laser power is applied only when the cathode is grounded, i.e. no electron current is produced during the irradiation. Periodically, the heating laser is reduced in intensity and the cathode is biased, which allows to observe the development of QE over many hours/days.

A schema of the set-up is presented in Fig. 2. The used
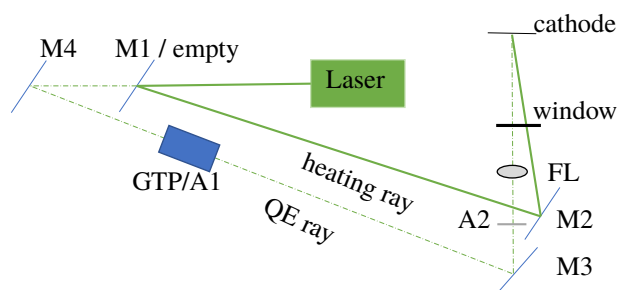
Figure 2: Schema of lifetime measurement under laser heating. M1-M4: mirrors, A1-A2: attenuator, FL: focusing lense.

diode pumped solid state laser (Roithner RLTMGL) is capable of up to 2 W heating power at $\lambda = 532$ nm. The heating ray passes two mirrors (M1, M2) before entering the vacuum window. The laser beam was directed towards the cathode without the need of focusing elements, which resulted in a diameter of ≈ 3 mm on the cathode.

Sitting on a dual-position slider, M1 can be swapped with an empty position, allowing the beam to be used for QE measurements. To ensure low power, a Glan-Thomson polarizer (GTP) is used as an attenuator, where only the extraordinary ray is transmitted and passes an optional additional attenuator A2.

Lifetime τ is defined as the time when QE is reduced to a factor 1/e of the initial value QE_0. One can identify τ as the reciprocal value of the exponential decay constant λ

$$QE(t) = QE_0 \times e^{-\lambda t} = QE_0 \times e^{\frac{-t}{\tau}} \tag{1}$$

By fitting the parameter τ, the lifetime can be determined.

Time Response Measurements

Usually, the transport from the cathode plant to PKAT takes about 1 hour. We use a load lock, which is baked

out at $120\,°C$ for 2 days and a four-way cross as transport chamber pumped by an IGP (GammaVacuum TiTan45S) and a NEG module (GammaVacuum N50) to below $p = 1 \times 10^{-11}$ mbar. Before the cathode can be moved to the actual source, it has to pass a GaAs preparation chamber.

Figure 3 illustrates the measurement principle at PKAT, a detailed description of the apparatus is given in earlier publications [5], [7].
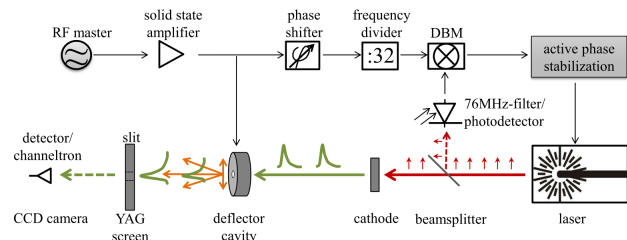
Figure 3: Schema of the time response measurements at PKAT. [11]

Here, only the basic ideas are presented: The radio frequency streak method is based on deflecting the temporal (longitudinal) bunch into a transverse one using a deflecting cavity. Femtosecond laser pulses are produced in phase with the RF ($2.449\,GHz$) and generate electron bunches with a repetition rate of $76\,MHz$ (32nd subharmonic of RF). Since laser and cavity are synchronized, shifting the phase of the laser allows to record the bunch profile sequentially by a channeltron after passing a slit or directly on a YAG screen. The detected intensity distribution represents a convolution of the real response of the cathode with the resolution of the apparatus and other effects, e.g. transit time spread. The experimental resolution is estimated to be 1-2 ps. One key to high resolution is to have a very small beam spot at the slit, since this is one of the biggest contributions to the measured signal. We have achieved an effective contribution of 0.431 ps (see Fig. 7) of the beam size to the time resolution.

RESULTS AND DISCUSSION

Cathodes Properties

Many cathode preparations with QE above $10\,\%$, some above $20\,\%$ have been achieved. Nevertheless, we are still improving reproducibility since the production is not yet ideal. On the one hand, for a long time the substrate temperature during preparation was not clear due to a lack of glow filament calibration. On the other hand, though they have some advantages over SAES dispensers like a larger capacity, AlfaSources dispensers are known for reproducibility issues [8]. Glow filament calibration has been carried out. We expect more reproducibility in the future. Figure 4 shows QE measurements at different wavelengths for three cathode samples along with values from Sommer [10].

We have used two cathodes (grown on Mo and SUS) for time response and one (grown on SUS) for lifetime measurements.
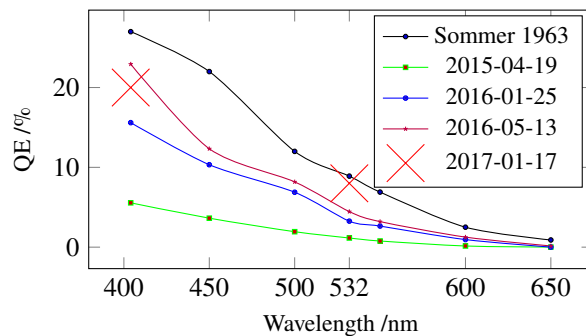
Figure 4: Spectral analysis for three example cathodes are shown. QE for cathode #2017-01-17 reached $9\,\%$ at $\lambda = 532\,nm$. Lines are to guide the eye only.

Cathode #2017-01-17 was measured with nearly $QE = 9\,\%$ for green light. This is comparable to results obtained by other groups [4].

Lifetime

All produced cathodes were stable at the cathode plant chamber pressure. Some cathodes even improved QE during storage indicating reorganization of the crystal structure over time, e.g. QE of cathode #2016-01-25 rose in a few weeks from $QE = 16\,\%$ up to $QE = 20\,\%$. Vacuum lifetime for K_2CsSb can be extrapolated to months, even years.

Nevertheless, alkali antimonides are known to decrease in QE after transport using a baked out load lock system [9], which we can also confirm.

The lifetime under laser heating was expected not to be very high for the investigated cathode since the thermal conductivity of the cathode holding system has not been optimized for this application. Assuming $25\,\%$ reflection at green light for K_2CsSb [12], a considerable fraction of laser power is absorbed by the thin cathode layer ($< 100\,nm$). Transmitted laser power can be reflected or absorbed by the substrate. Due the to low thermal conductivity of SUS, the heat would not dissipate as effectively as for instance with Mo as substrate, as simulations in [13] indicate.

Figure 5 illustrates the QE decay for $P_{Heat} = 300\,mW$, a fit to the data obtains a lifetime of $\tau \approx 31$ h.
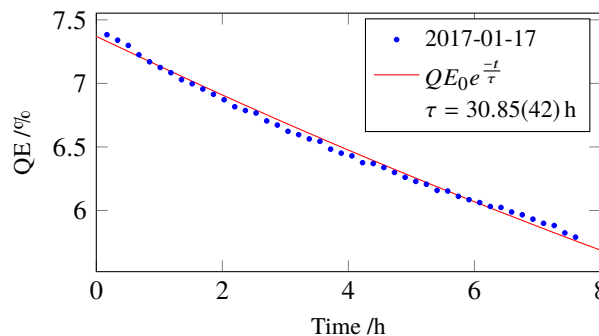
Figure 5: Representative lifetime measurement under laser heating with $P_{heat} = 300\,mW$.

The intensity used in this experiment can be considered typical for 10 mA operation at MESA with a blue laser since a $QE = 10\,\%$ cathode would yield 33 mA W^{-1}. The corresponding lifetime is not sufficient to sustain long-term experiments. Notice that for laser powers up to ≈ 200 mW QE even improved for a while, which indicates a faster reorganization at elevated temperature until crystal defects begin to dominate and lower the performance of the cathode.

As Fig. 6 indicates, increased laser power is reducing lifetime of the cathode. At 500 mW, the K$_2$CsSb would survive only a few hours.
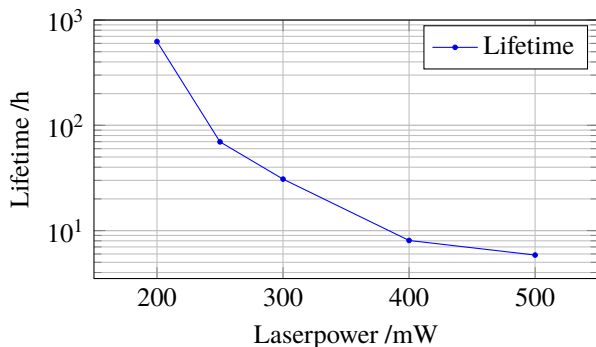
Figure 6: Lifetime measurements for cathode #2017-01-17. Lifetime drops significantly with higher laser power. Line is to guide the eye only

The results show mainly two things:

- a high QE cathode is indispensable, the higher the QE the lower the laser power

- though non thermal effects like non-linear photochemistry could also explain the observations, the most probable explanation seems to be thermal decomposition of the photocathode. It therefore seems necessary to achieve a better thermal conductivity.

Time Response

Time response measurements of two K$_2$CsSb cathodes have been performed so far. We measured a massive QE decrease (down to 0.0001 %) for the first cathode due to a vacuum incident after opening the valve to the GaAs preparation chamber, where the pressure rose to 1×10^{-6} mbar for about 30 s. It is remarkable that in spite of the very serious reduction of the QE, the pulse response was roughly similar to the cathode investigated later. Due to unknown crystal properties, time response results of this cathode will not be discussed here.

We were able to successfully measure the time response of another K$_2$CsSb cathode, though QE dropped also this time (1 % at $\lambda = 405$ nm) after transport, probably due to a small leakage of the oxygen valve at the GaAs preparation chamber. Notice that time response experiments are limited to a small bunch charge (< 0.1 fC) due to space charge effects, so a high QE cathode is not needed necessarily.

Two measurements of the same cathode are presented in Fig. 7.
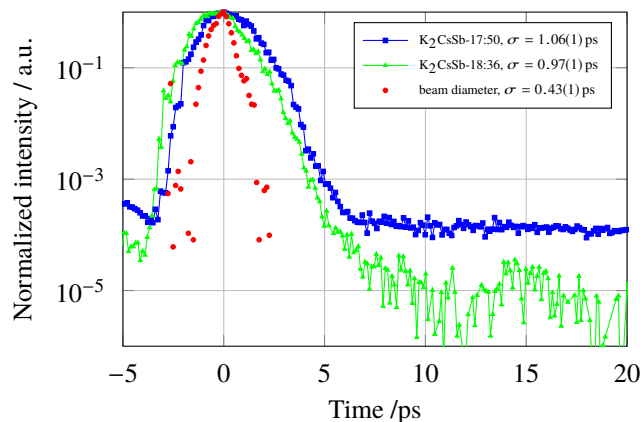
Figure 7: Time response and longitudinal halo of K$_2$CsSb. The blue curve represents the measurement with the largest halo observed. The green curve is the typical measurement with a very small halo. The red curve represents the transverse beam diameter, which contributes $\sigma \approx 0.43$ ps to the time resolution.

The result show a very fast response of $\sigma = 970$ fs for K$_2$CsSb, which is within the resolution of our apparatus. Thus, the upper limit of 1 ps can be confirmed.

Time response is faster than the NEA photocathode Cs:GaAs, and also the longitudinal halo is about a factor 3-10 lower than we have found for CsO:GaAs, making this photocathode favorable for RF sources. See also [11].

The fluctuations given in Fig. 7 (green curve) for the time > 10 ps are assigned to background of the channeltron. Artifacts of laser reflections e.g. at the vacuum window are responsible for the remaining signal.

CONCLUSION AND OUTLOOK

In conclusion, K$_2$CsSb shows the expected potential for a high QE cathode with sub-picosecond response time and a very low longitudinal halo, qualities which are very important for SRF/RF electron sources. Lifetime under laser heating is relatively short on a SUS substrate, probably indicating fast chemical reactions taking place at elevated temperature which damage the optimal conditions for the photo electron yield. In the near future, we will try better thermal arrangements with the goal to improve the lifetime under high intensity laser irradiation.

Furthermore, it is planned to install a Kelvin Probe (McAllister KP6500) at the analyzing chamber to measure the work function in-situ. This tool will also give information about changes of the surface conditions.

ACKNOWLEDGMENT

REFERENCES

[1] D. Dowell, I. Bazarov, B. Dunham, K. Harkay, C. Hernandez-Garcia, R. Legg, H. Padmore, T. Rao, J. Smedley, and W. Wan, "Cathode R&D for future light sources," *Nuclear Instruments and Methods in Physics Research Section A: Accelerators, Spectrometers, Detectors and Associated Equipment*, vol. 622, no. 3, pp. 685 – 697, 2010. [Online]. Available: http://www.sciencedirect.com/science/article/pii/S0168900210006868

[2] W. E. Spicer and A. Herrera-Gomez, "Modern theory and applications of photocathodes," in *Proc. SPIE Int. Soc. Opt. Eng.*, vol. 2022, no. SLAC-SSRL-0042, 1993, pp. 18–33.

[3] L. Cultrera, I. Bazarov, A. Bartnik, B. Dunham, S. Karkare, R. Merluzzi, and M. Nichols, "Thermal emittance and response time of a cesium antimonide photocathode," *Applied Physics Letters*, vol. 99, no. 15, p. 152110, 2011.

[4] H. Xie, I. Ben-Zvi, T. Rao, T. Xin, and E. Wang, "Experimental measurements and theoretical model of the cryogenic performance of bialkali photocathode and characterization with Monte Carlo simulation," *Physical Review Accelerators and Beams*, vol. 19, no. 10, p. 103401, 2016.

[5] P. Hartmann, J. Bermuth, D. v. Harrach, J. Hoffmann, S. Köbis, E. Reichert, K. Aulenbacher, J. Schuler, and M. Steigerwald, "A diffusion model for picosecond electron bunches from negative electron affinity GaAs photocathodes," *Journal of applied physics*, vol. 86, no. 4, pp. 2245–2249, 1999.

[6] K. Aulenbacher, J. Schuler, D. v. Harrach, E. Reichert, J. Röthgen, A. Subashev, V. Tioukine, and Y. Yashin, "Pulse response of thin III/V semiconductor photocathodes," *Journal of applied physics*, vol. 92, no. 12, pp. 7536–7543, 2002.

[7] M. A. Dehn, K. Aulenbacher, and V. Bechthold, "Pulse response measurements of NEA photocathodes at different laser wavelengths," in *7th International Particle Accelerator Conference (IPAC'16), Busan, Korea, May 8-13, 2016*. JACOW, Geneva, Switzerland, 2016, pp. 3931–3933.

[8] S. Karkare, I. Bazarov, L. Boulet, M. Brown, L. Cultrera, B. Dunham, N. Erickson, G. Denham, A. Kim, B. Lillard *et al.*, "Advances in photocathode technology at Cornell university," in *North Amer. Particle Accelerator Conf.*, 2013, pp. 391–393.

[9] T. Rao, "Multialkali cathode for high current electron injector: Fabrication, installation and testing," in *MOIBCC004, presented at The 59th ICFA Advanced Beam Dynamics Workshop on Energy Recovery Linacs (ERL17)*, 2017.

[10] A. Sommer, *Photoemissive materials. Preparation, properties and uses*, N. York, Ed.   Wiley, 1968.

[11] M. A. Dehn, V. Bechthold, and K. Aulenbacher, "Longitudinal halo from NEA and PEA photocathodes," in *MOIBCC002, presented at The 59th ICFA Advanced Beam Dynamics Workshop on Energy Recovery Linacs (ERL17)*, 2017.

[12] D. Motta and S. Schönert, "Optical properties of bialkali photocathodes," *Nuclear Instruments and Methods in Physics Research A*, vol. 539, pp. 2017–235, 2005.

[13] J. McCarter, "Photocathode research for electron accelerators," Ph.D. dissertation, Department of Materials Science and Engineering School of Engineering and Applied Science University of Virginia, 2012.

THE SMALL THERMALIZED ELECTRON SOURCE AT MAINZ (STEAM)

S. Friederich*, K. Aulenbacher, Johannes Gutenberg-Universität, Mainz, Germany

Abstract

The Small Thermalized Electron Source at Mainz (STEAM) is a photoelectron source which will be operated using NEA GaAs excited near its band gap with an infrared laser wavelength to reach smallest emittances. CST simulations indicate that emittance growth due to vacuum space charge effects can be controlled up to bunch charges of several tens of pC. The goal of the project is to demonstrate that the intrinsic high brightness can still be achieved at such charges. The current status will be presented.

INTRODUCTION

The brightness of a particle source can be calculated by the fraction of the emitted electron current I, the transverse emittances ε_x and ε_y and the relative energy spread $\frac{\Delta E}{E}$, see Eq. 1. It is a figure of merit for an ERL accelerator source.

$$B \propto \frac{I}{\varepsilon_x \, \varepsilon_y \, \Delta E/E} \propto \frac{QE(\lambda) \, P_L}{\varepsilon_x \, \varepsilon_y \, \Delta E/E} \qquad (1)$$

The current of a photoemission electron source is mainly given by the power of the laser and the quantum efficiency $QE = N_{electrons}/N_{photons}$, which depends on the laser wavelength λ. The normalized thermal residual-mean-square (rms) emittance can be derived from the exciting laser spot size σ_0 and the thermal energy $k_B T$, see Eq. 2 [1].

$$\varepsilon_{n,rms} = \frac{\sigma_0}{2} \sqrt{\frac{k_B T}{m_e c^2}} \qquad (2)$$

The thermal energy decreases with increasing laser wavelength [2], therefore the smallest emittance can be achieved at the maximum possible exciting wavelength near the band gap energy E_g of the used semiconductor material, e.g. for NEA GaAs ($E_g = 1.4\,eV$) $\lambda_L \approx 800\,nm$ is only 130 meV above the band gap, which should result in high QE but still low thermal energy and corresponds to the typical wavelength of powerful semiconductor lasers. Seen from this solid state physics point of view, it is important for high current accelerators how the emittance develops with increasing bunch charges. To investigate this aspect further, a high extracting field gradient is needed to suppress space charge effects, which is above all a low energy issue.

THE DESIGN OF STEAM

STEAM was designed and optimized to operate at 200 kV with an extracting field gradient of 5 MV m⁻¹. Its vertical design was inspired by the existing photoemission electron source Polarisierte Kanone (PKA) at the Institute of Nuclear Physics in Mainz and it uses the "inverted" R30 insulator

adopted by the Jefferson Laboratory [3], see Fig. 1. The simulation program Computer Simulation Technology (CST) [4] was used to find an applicable cathode and anode geometry so that the field gradient on any point of the electrode structure stays below 10 MV m⁻¹, see Fig. 2. This is to reduce the risk of field emission.
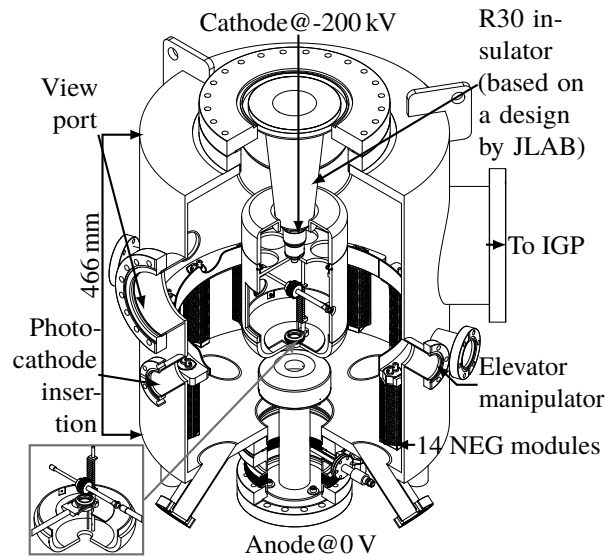
Figure 1: STEAM chamber, cathode and anode design. A working sketch of the elevator is shown in the lower left corner.
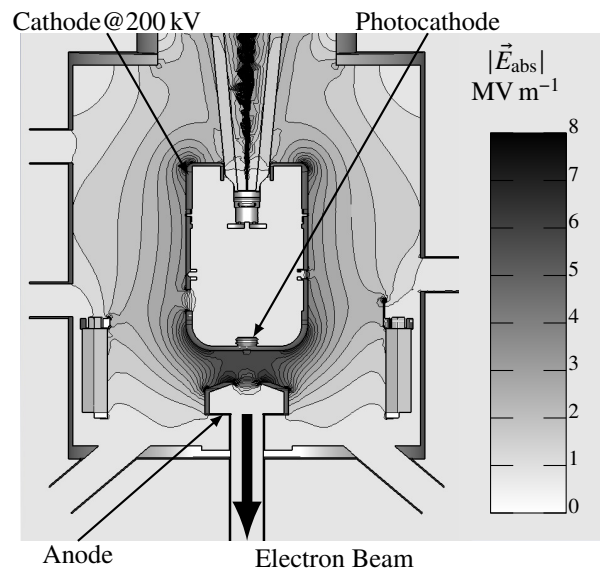
Figure 2: Electrostatic simulation using CST. The absolute field gradient in STEAM @ $U = 200\,kV$ stays below 10 MV m⁻¹, while an extracting field gradient of $|\vec{E}|_{acc} \approx 5\,MV\,m^{-1}$ is achieved. The HV cable is also simulated.

---

* sifriede@uni-mainz.de

PIC SIMULATION RESULTS

The source performance was simulated using the Particle-in-Cell (PIC) code of CST Particle Studio and compared to the geometry of the PKA. With respect to the same cathode potential of 100 kV, the main difference between the sources is the extracting field gradient, i. e. $|\vec{E}|_{\text{acc}}^{\text{STEAM}} \approx 2.5 |\vec{E}|_{\text{acc}}^{\text{PKA}}$. The simulation parameters are listed in Tab. 1 and Fig. 3 shows a scheme of the longitudinal bunch profile used in the simulation. The normalized thermal rms emittance $\varepsilon_{\text{x,n,rms}}$ and the energy spread were calculated using Eq. 3 and 4, and the results are shown in Fig. 4.

$$\varepsilon_{\text{x,n,rms}} = \beta\gamma\sqrt{\langle x^2\rangle \cdot \langle x'^2\rangle - \langle x \cdot x'\rangle^2} \qquad (3)$$

$$\frac{\Delta E}{E} = \frac{E_{\max} - E_{\min}}{eU + m_{\text{e}}c^2} \qquad (4)$$

Table 1: CST PIC simulation parameters

Source	STEAM	PKA
Number of particles	$\approx 450\,000$	$\approx 570\,000$
Thermal start energy kT	200 meV	
Radius of emitting area	0.5 mm	
Interaction point $\approx d_{\text{cathode-anode}} + $ Drift	240 mm	400 mm
$|\vec{E}_{\text{acc}}|$ @ 100 kV	2.5 MV m^{-1}	1 MV m^{-1}
Gaussian emission model	$t_\sigma = 100$ ps	

When increasing the bunch charge, the space charge affects the emittance growth and therefore the brilliance. The higher extracting field gradient of STEAM accelerates the electrons faster and allows to reach higher bunch charges at practical accelerator emittances below 1 μm.

Figure 3: Longitudinal gaussian bunch profile used in CST. As indicated, t_{cutoff} limits the longitudinal dimension of the emitted bunch.

Figures 5 and 6 show examples for 1 fC and 7.7 pC of the transverse phase space and for the longitudinal bunch profile. The extracted bunches are more divergent at STEAM because the shape of the puck that holds the photocathode crystal has a flat geometry, which is due to the trade-off for the higher extracting field gradient. At the PKA the puck is concave-formed. To compensate for that a little, the anode at STEAM is formed slightly convex.

CURRENT PROGRESS

A platform was built in January 2016 and the fully assembled STEAM with its photocathode preparation chamber was put on top of it. After finishing the bake-out procedure the source has reached ultra high vacuum condition, i. e. its pressure is at 5×10^{-12} mbar. As soon as the 200 kV high voltage power supply (HVPS) is ready, the source will be processed with krypton gas based on a technique by JLAB [5].
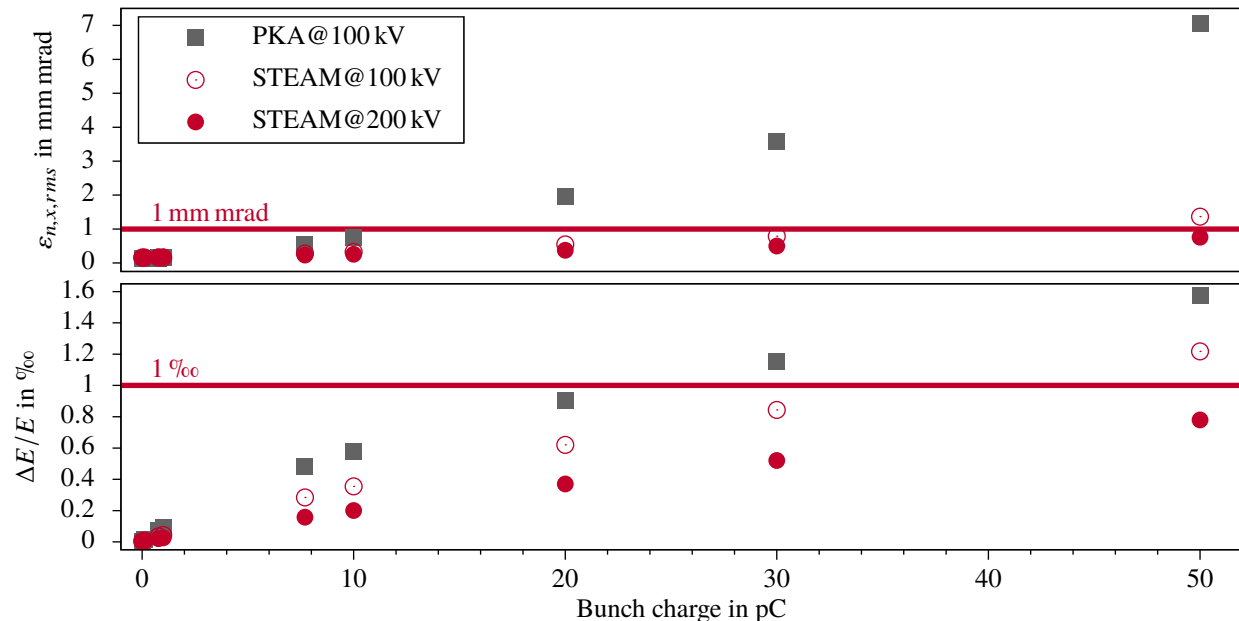
Figure 4: (Above) Normalized transverse rms emittance and (below) energy spread calculated from PIC simulations of PKA and STEAM for increasing bunch charges. Further simulation parameters are given in Tab. 1.
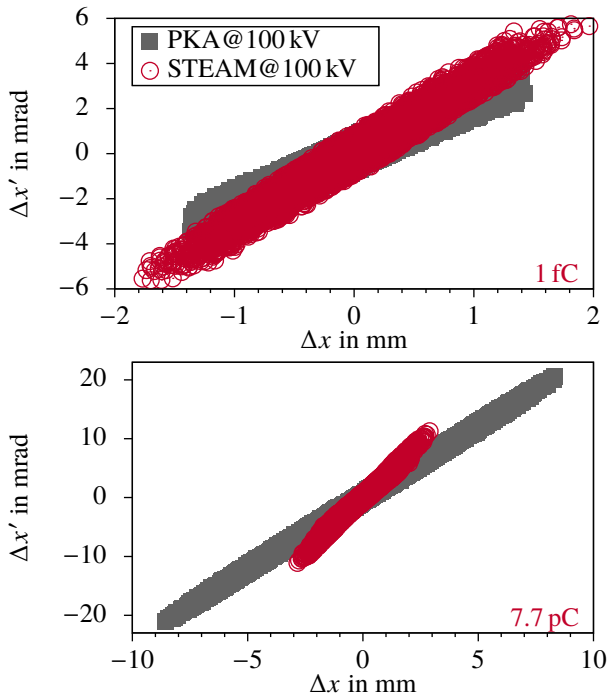
Figure 5: Examples of the transverse phase space for 1 fC (above) and 7.7 pC (below). Only every 50th particle is plotted. The higher divergency at STEAM can be explained by the flat puck geometry, which is concave-formed at PKA. The STEAM anode is formed convex.
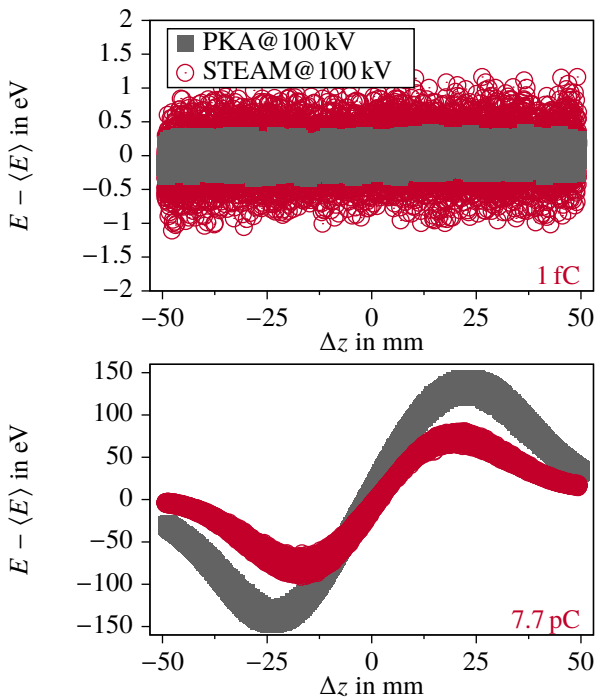
Figure 6: Examples of the longitudinal phase space for 1 fC (above) and 7.7 pC (below). Only every 50th particle is plotted. The effect of the non-linearities of space charge can be seen in the lower plot. STEAM's higher field gradient compensates for that more.

Testing the preparation chamber, the first NEA bulk GaAs photocathode was prepared and its lifetime was measured. The quantum efficiency reached 5 % at 635 nm but decreased rapidly down to 1.7 % within 16.5 h. This was due to a comparatively high gas pressure inside the preparation chamber ($\approx 1 \times 10^{-10}$ mbar).

The 200 kV HVPS was tested concerning its interlock mechanism and the remote controllability. Due to difficulties with the remote communication and problems with the sustainability of the HV near the maximum output level, the HVPS was sent back to the vendor for repair. The problems have been solved recently and operation is starting.

FUTURE PLANS

The STEAM will be investigated using the Mainz Energy-Recovering Superconducting Accelerator (MESA) Low-Energy Beam Apparatus (MELBA). This diagnostic and spin manipulating beam line offers i. a. the possibility to measure the transverse emittance using the quadrupole scan or the slit-and-grid method. The MELBA is fully assembled and is currently being baked out. Preparations for the laser system are going on. The control system will be based on the Experimental Physics and Industrial Control System (EPICS) and first experiences for MESA will be gathered in this context. After the HV krypton gas processing, the MELBA will be ready, so that the first electron beam coming from STEAM can be expected in summer 2017. Further information about the MELBA is presented in [6].

ACKNOWLEDGMENT

REFERENCES

[1] M. Reiser, *Theory and design of charged particle beams*. John Wiley & Sons, 2008.

[2] I. Bazarov, B. Dunham, F. Hannon, Y. Li, X. Liu, T. Miyajima, D. Ouzounov, and C. Sinclair, "Thermal emittance measurements from negative electron affinity photocathodes," in *Particle Accelerator Conference, 2007. PAC. IEEE*. IEEE, 2007, pp. 1221–1223.

[3] P. A. Adderley, J. Clark, J. Grames, J. Hansknecht, K. Surles-Law, D. Machie, M. Poelker, M. L. Stutzman, and R. Suleiman, "Load-locked dc high voltage GaAs photogun with an inverted-geometry ceramic insulator," *Phys. Rev. ST Accel. Beams*, vol. 13, p. 010101, Jan 2010. [Online]. Available: https://link.aps.org/doi/10.1103/PhysRevSTAB.13.010101

[4] Computer Simulation Technology, http://www.cst.com/.

[5] C. Hernandez-Garcia, S. Benson, G. Biallas, D. Bullard, P. Evtushenko, K. Jordan, M. Klopf, D. Sexton, C. Tennant, R. Walker *et al.*, "DC high voltage conditioning of photoemission guns at Jefferson Lab FEL," in *AIP Conference Proceedings*, vol. 1149, no. 1. AIP, 2009, pp. 1071–1076.

[6] C. Matejcek, K. Aulenbacher, S. Friederich, and L. Hein, "Low-energy beam transport system for MESA." Institute of Nuclear Physics, Mainz, ERL'17, MOPSPP008.

SPOCK - A TRIODE DC ELECTRON GUN
WITH VARIABLE EXTRACTION GRADIENT

L.M.Hein†, V.Bechthold, M.A.Dehn, S.Friederich, C.Matejcek, K.Aulenbacher

Institut für Kernphysik, Johannes Gutenberg-Universität Mainz, Mainz, Germany

Abstract

The electron source concept SPOCK (**S**hort **P**ulse **So**urce at **K**PH) is a 100kV DC source design with variable extraction gradient. Due to its triode inspired design the extraction gradient can be reduced for e.g. investigations of cathode physics, but also enhanced to mitigate space charge effects. In the framework of the MESA-Project (**M**ainz **E**nergy-Recovering **S**uperconducting **A**ccelerator) [1] its design has been further optimized to cope with space charge dominated electron beams. Although it injects its electron beams directly into the LEBT (**L**ow **E**nergy **B**eam **T**ransport) matching section, which excludes any adjustments of the electron spin, the source SPOCK will allow higher bunch charges than the MESA standard source.

CONCEPT

The concept of the horizontal DC electron gun SPOCK [2] is based on the design of triodes developed beginning 20th century. By means of an additional control plate in-between anode and cathode the extraction voltage can be altered, see Fig. 1.
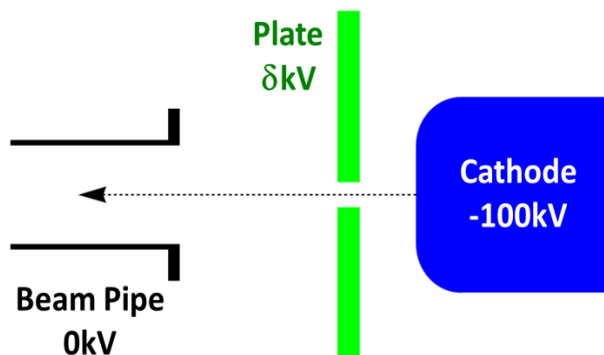
Figure 1: Concept of SPOCK

The basic design idea has been developed [3] in order to clarify the contribution of photocathode energy spread to the time response [4] of photocathodes. Due to variations of the extraction field gradient its contribution can be isolated from other effects and separately investigated. Further details to this subject will be recapitulated in e.g. [4]. Simultaneously, this layout possesses a potential for high brilliance electron beams. A major challenge is the preservation of the transverse emittance in presence of space charge. By setting the control plate at a high potential the extraction field at the cathode surface is significantly amplified. Hence the electron acceleration is considerably enhanced mitigating the space charge impacts on the beam qualities such as the transverse emittance and the energy spread.

Design and Dimensions

The design of the source is based on the design of the JLAB source [5]. It features electrode supporting insulators extending into the interior of the grounded vacuum vessel. This is known as an "inverted" source. An overview of the specific features and technical advantages of such a design is given in [5]. The main components of the source are the cathode, the anode and the control plate. By means of two ceramic isolators the cathode and plate are electrically separated. Anode and beam pipe are grounded. As in case of high intensity beam operations an early transverse focusing is beneficial, a plug-in vacuum vessel is designed containing space for a double-solenoid. This double solenoid will be placed approximately s=220mm downstream the cathode. In order to ensure the vacuum condition of p≈10⁻¹¹mbar ten NEG (Non Evaporable Getter) modules grouped in two half circles are surrounding this plug-in vessel. Two additional IGP (ion getter pumps) will be attached to the main chamber. A scheme of the source design is given in Fig 2.
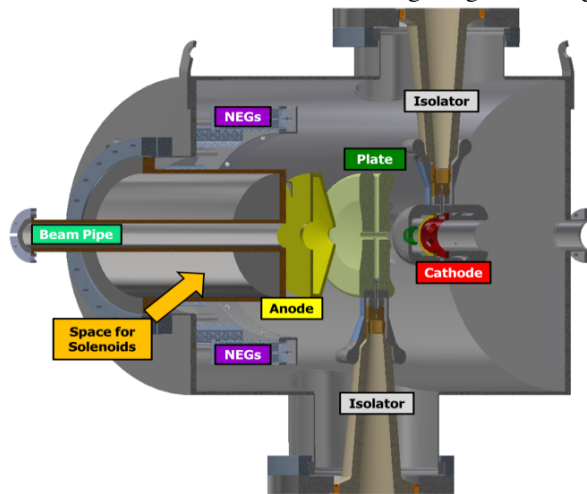
Figure 2: Design SPOCK

The dimensions of the main source vessel are length L=620mm and diameter D=410mm. A CF200 flange connects the main source chamber with the plug-in vessel. In the design phase the diameter of the plug-in vessel is set to d=170mm. Apart from hosting the double solenoid and the CF40 beam pipe the plug-in vessel also serves as a support for the extraction anode, whose shape is adapted from the source STEAM (**S**mall **T**hermalized **E**lectron Source **At** **M**ainz) [6]. The isolators are type R30 isolators with a height of h≈240mm. Numerous minor variations in the design of the control plate and the cathode were required to mitigate potential field emissions and to allow a

straightforward assembly of the components. The design of the control plate is currently in the final stage.

Field Maps

A major challenge of DC particle sources is the control of field emission. In order to avoid field emission during operation the design field gradients at the source SPOCK and STEAM were limited to E<10MV/m. At the source SPOCK the highest field gradients are located at the front plane of the cathode, at the rounding of the voltage shoes of the cathode and control plate as well as at the back plane of the control plate. In case of a grounded control plate the field gradients do not exceed 6MV/m. The peak fields are at the rounding of the cathode front plane, the upper part of the plate and at the cathode voltage shoe, see Fig. 3.
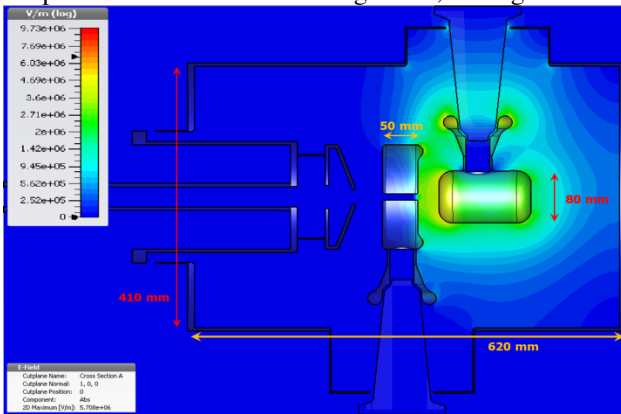
Figure 3: Field Map – $U_{plate}=\pm 0kV$

By setting the plate potential to $U_{plate}=+80kV$ the field gradients are close to the limitation of $E_{max}=10MV/m$. They are concentrated at the rounding of the cathode front plane and the upper part of the plate, see Fig. 4.
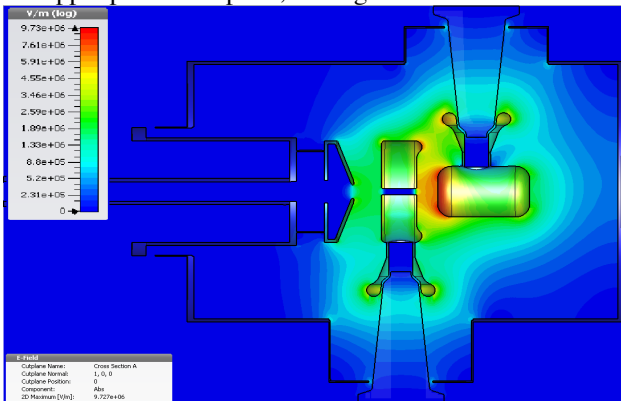
Figure 4: Field Maps – $U_{plate}=+80kV$

The field calculations were conducted using the code Computer Simulation Technology (CST) [7].

SIMULATION PARAMETERS

The simulations of the electron bunch generation were conducted using the code CST as well. Due to the unique properties of the source the generation of two mainly different types of electron beams is contemplated. For investigations of the cathode physics mostly low intensity, short bunches will be generated. The investigation of this

scenario is work in progress, in the following the focus is on bunches characterised by larger bunch charges and bunch lengths. For this scenario the rms bunch length is defined to $\sigma_t=50ps$. This leads to a total bunch length of $\Delta T=200ps$ to $\Delta T=300ps$. In both scenarios the longitudinal density distribution is defined by Gaussian profiles, which are truncated at $L=\pm 3\sigma_t$. The transverse laser profile at the cathode surface is also characterised by Gaussian functions. Most simulations were conducted assuming a laser spot size of $R_{laser}=0.3mm$. Studies with $R_{laser}=0.5mm$ are in preparation. Further initial beam parameters are $E_{kin}=0.2eV$, $E_{spread}/E_{kin}=95\%$ and angular spread $\Delta\vartheta=89.9deg$. The simulations were conducted using the CST Particle in Cell (PIC) solver with at least 150.000 particles for the high bunch charge studies.

SOURCE BEAM DYNAMICS

The beam dynamics of the DC source SPOCK is mainly determined by the potential setup of the cathode and the control plate as well as the settings of the laser. Major parameters of the laser such as its pulse length and its transverse cross section are maintained constant during the parameter sweeps. Hence, the electron bunch length within the first 200mm downstream the cathode is defined by the particle acceleration respectively deceleration. At high bunch charge operations higher extraction field gradients are beneficial, since the superior acceleration near the cathode extends the initial bunch length, i.e. the distance from the first emitted particles of the bunch to the last emitted particles leaving the cathode, and so it leads to a lower charge density during the electron extraction. A grounded control plate, i.e. $U_{plate}=0kV$, specifies an average extraction field gradient of approximately 3.3MV/m. It results in a total, initial bunch length of L=35 mm. A control plate potential of $U_{plate}=+80kV$ extends the bunch length to approximately L=55mm. Its impact on the normalised transverse emittance of a bunch with charge of q=1pC is illustrated in Fig. 5.
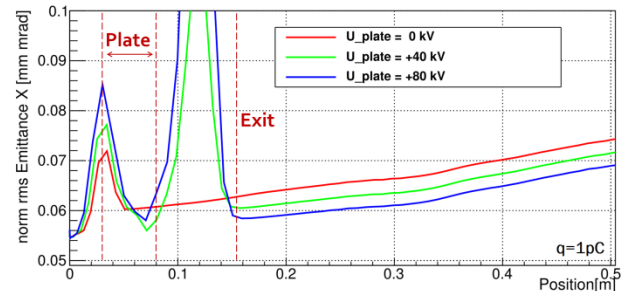
Figure 5: Emittance Development along the Source

Position s=0m indicates the position of the cathode surface. The control plate covers the distance from s=0.03m to 0.08m. At position s=0.16m the beam enters completely the extraction cathode and at approximately s=0.2m the solenoid edge field. Upstream the extraction anode the transverse normalised emittance varies significantly. Since the bunch length is comparable with the drift lengths between cathode and control plate respectively between control plate and anode, the particle energy varies significantly

along the bunch. During the passage through the control plate major fractions of the electric field induced energy spread are cancelled, which leads to the drop of the emittance at position s= 0.07m. As the initial bunch length of the setting U_{plate}=+80kV exceeds the length of the control plate of L=50mm, its electric field induced energy spread is not completely compensated.

At position s=0.16m the beam enters the extraction anode, its average kinetic energy is set to E_{kin}=100keV and the correlated energy spread induced by the acceleration/deceleration field is cancelled. The deceleration or acceleration downstream the control plate to the final energy also adjusts the initial bunch length. Due to the enhanced acceleration at settings with a positively charged control plate space charge effects near the cathode are mitigated, which leads to superior transverse emittance preservations. Moreover, the higher extraction field gradients also lead to lower energy spread values and lower longitudinal emittances. A brief quantitative recapitulation of the beam parameters at the source exit, i.e. at position s=0.2m, is given in the next paragraph. Fig. 6 shows exemplarily a phase space plot of two particle distributions at position s=0.2m, i.e. inside the extraction anode.
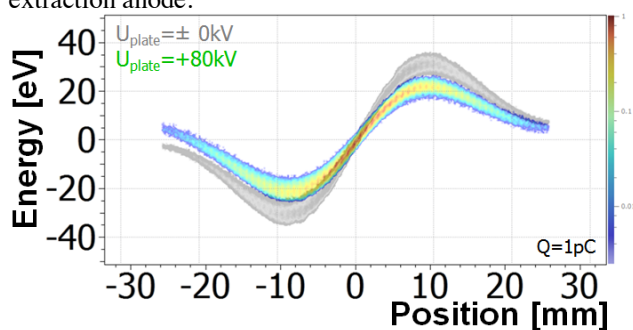
Figure 6: Longitudinal Phase Space Plot [8]

The non-linear space charge effects are causing a characteristic dependency between the particle energy and its position within the bunch [9].

PARAMETER SWEEPS

A non-finalised design parameter is the shape of the control plate. Its modelling can be used to further enhance the extraction field gradient as well as to apply additional beam focussing. A summary is given in [2]. Additional parameters are the bunch charge, the potential of the control plate, the radius of the laser spot at the cathode and its time pattern. In the framework of the MESA Project the source STEAM is foreseen as primary source to generate polarised electron beams. Since this source is designed as a high brilliance electron source, its parameters are used to benchmark the transverse emittance values of the SPOCK source. Therefore, the beam parameters are recorded at the source exit at position s=0.2m. The extraction gradient of STEAM [6] at $U_{cathode}$=100kV is comparable with the SPOCK field gradient with grounded control plate. Hence, comparable transverse emittance values are expected. A sweep of the total bunch charge indicates the similar dependency as well as the benefit of the extraction field enhancement, Fig 7.
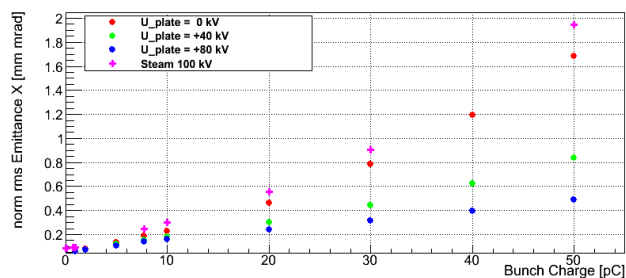
Figure 7: Transverse Emittance

Especially at high bunch charges q≥10pC the field enhancements of 40% and above lead to superior preservations of the transverse emittance. As a result of the transverse emittance growth at high bunch charges the growth of the longitudinal emittance is mitigated, Fig. 8.
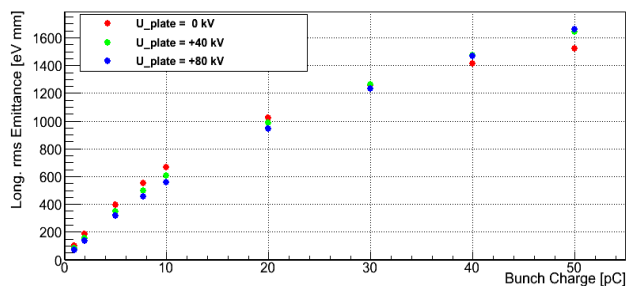
Figure 8: Longitudinal Emittance

However, at bunch charges below q=20pC lower transverse and longitudinal emittances are feasible by means of amplified initial acceleration. The impact of the acceleration gradient and the bunch charge on the rms energy spread is plotted in Fig. 9.
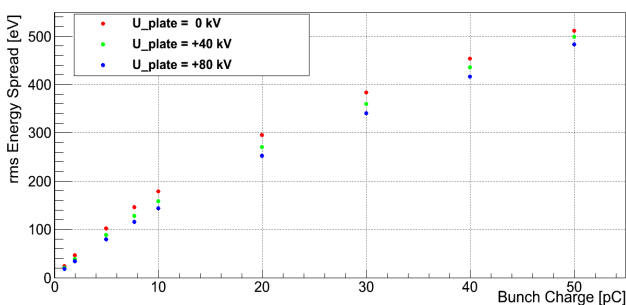
Figure 9: rms Energy Spread

REDUCED MELBA

The length of the entire MELBA (**ME**SA **L**ow Energy **B**eam **A**pparatus) section accounts to approximately 10m. Its first half is dedicated to the source diagnostics, vacuum separation and the manipulation of the electron spin. The second half (MELBA-2) is used to match the beam to the downstream accelerator [10]. Since the SPOCK electron beams will be injected directly into the matching section, the significant length reduction of the low energy transfer section will be beneficial to preserve the beam quality in presence of space charge effects. The layout of the SPOCK MELBA is illustrated in Fig. 10.

The remaining 4.7m long section between the cathode and the MAMBO accelerator (**M**illi**am**pere **Bo**oster) [11] con-

Figure 10: Scheme LEBT

tains the chopper, the buncher and the transverse matching elements, i.e. quadrupole magnets and solenoids. In order to minimise the length of the MELBA-2 section in favour of emittance preservation and the integration into the MESA facility an alternative design of the differential pumping stage is under investigation. In between the source and the MELBA injection a dipole section with a 12 deg deflection angle and a reduced aperture from CF40 down to CF16 will be inserted. The aperture reduction in combination with the bending section will reduce the residual gas load from the MELBA and in particular from the chopper collimator. Moreover, the 12 deg deflection also allows a head-on laser injection into the source. Further details to the laser injection and laser adjustments are recapitulated in [2]. However, due to this dipole section the transverse symmetry is broken. The dispersion causes an increase of the horizontal emittance and an additional focusing in the horizontal plane. Its impact on the development of the transverse beam sizes for a q=1pC bunch is shown in Fig. 11.

Figure 11: rms Beam Size along the LEBT

An enhancement of the optics distortion is given at higher bunch charges as well as settings of the source solenoid, which are leading to a larger horizontal beam size at the dipole entrance. Another critical part of the MELBA section is the chopper, which consists of adjustable collimator embedded into a double solenoid with a focal length of f≈0.17m. In order to mitigate its impact on the transverse beam size two double solenoids surrounding the chopper are foreseen to minimise the transverse beta function around the collimator. The optimised settings of the chopper are not defined so far and require further detailed studies of the downstream accelerator. In the presented simulation the beam is not collimated. In terms of emittance preservation the XY-matching section downstream the buncher is especially crucial. By means of the buncher [12] a correlated energy spread is imprinted. Along the XY-matching section the bunch length decreases, which leads to an increase of the charge density and an amplification of the space charge forces. Hence, any strong and rapid

variations of the transverse beam sizes have to be avoided while matching the transverse Twiss parameters.

CONCLUSION AND OUTLOOK

Compared to the standard source for MESA it has been demonstrated that with the new source SPOCK significant advantages can be achieved. Moreover the shortening of the injection beam line by about a factor 2 will also help to increase the bunch charge for MESA even if no increase of the source energy is envisaged. Shortly the shape of the electrodes will be finalized. The potential for higher bunch charges injected into the second half of the MESA-LEBT will soon be fully explored and a decision if SPOCK will be integrated in MESA will be taken.

ACKNOWLEDGEMENT

REFERENCES

[1] K.Aulenbacher et al., "Elementary Design Report for the Mainz Energy Recovering Superconducting Accelerator MESA", Institut für Kernphysik, Mainz, Germany, Oct. 2014.

[2] L.M.Hein, "SPOCK - Short Pulse Source at KPH, Technical Design Report", Institut für Kernphysik, Mainz, Germany, to be published.

[3] M.A.Dehn, ""Bau einer Elektronenquelle mit variablem Extraktionsgradienten zur Femtosekunden-Elektronenemissionsspektroskopie", Dissertation Thesis, Institut für Kernphysik, Johannes Gutenberg-Universität Mainz, Mainz, Germany, in preparation.

[4] V.Bechthold et al., "Time Resonse Investigations of K2CsSb Photocathodes" presented at ERL17, CERN, Switzerland, MOPSPP004, this workshop.

[5] M.Poelker et al., "Load-locked dc high voltage GaAs photogun with an inverted-geometry ceramic insulator" Phys. Rev. ST Accel. Beams 13, 2010.

[6] S.Friederich et al., "The Small Thermalized Electron Source at Mainz (STEAM)" presented at ERL17, CERN, Switzerland, MOPSPP005, this workshop.

[7] Computer Simulation Technology, Darmstadt, Germany.

[8] *PlotWin (V4)*, D.Uriot, CEA Saclay, France, April 2017 http://irfu.cea.fr/en/Phocea/Page/index.php?id=263

[9] K.Schindl, "Space Charge", in Proc. CERN Acclerator School, DESY, Zeuthen, Germany, Sept. 2003, pp. 305-320.

[10] C. Matejcek et al., "Low Energy Beam Transport System for MESA" presented at ERL17, CERN, Switzerland, MOPSPP008, this workshop.

[11] R.Heine et al., "Current Status of the Milliampere Booster for the Mainz Energy-Recovery Superconducting Accelerator", in Proc. *7th Int. Particle Accelerator Conf. (IPAC'16)*, Busan, Korea, May 2016, paper TUPOW002, pp. 1741-1743.

[12] P.Heil, "Longitudinale Emittanzanpassung durch Geschwindigkeitsmodulation im Injektionssystem am MESA", Master Thesis, Johannes Gutenberg-Universität Mainz, Mainz, Germany, 2015.

BEAM DYNAMICS AND COLLIMATION FOLLOWING MAGIX AT MESA

Ben Ledroit*, Kurt Aulenbacher, Johannes Gutenberg-Universität, 55128 Mainz, Germany

Abstract

The Mainz Energy-recovering Superconducting Accelerator (MESA) will be an electron accelerator allowing operation in energy-recovery linac (ERL) mode. After the beam hits the target at the MESA Internal Gas Target Experiment (MAGIX), the beam is phase shifted and recirculated back into the linac sections. These will transfer the kinetic beam energy back to the RF-field by deceleration of the beam and allow for high beam power with low RF-power input. Since most of the beam does not interact with the target, the beam will mostly just pass the target untouched. However, a fraction of the scattered electrons may be in the range outside the accelerator and detector acceptances and therefore cause malicious beam dynamical behavior in the linac sections or even damage to the machine. The goal of this work is to determine the beam behavior upon target passage by simulation and experiment and to protect the machine with a suitable collimation system. The present status of the investigations is presented.

MESA

An overview of MESA is given in [1]. MESA will supply the P2 experiment in external beam (EB) mode with a beam current of 150 µA at 155 MeV [1,2]. In EB mode, the whole beam is dumped after interaction with the target. A second beamline is set up for the ERL mode, where the beam passes the MAGIX target and is then phase shifted 180° to the RF and recirculated through the cryomodules for energy recovery. MESA will maintain a 1 mA beam current in the first stage and 10 mA after upgrade at 105 MeV.

MAGIX

ERL operation is possible since MAGIX provides a low density target and only a small fraction of the beam actually interacts with the gas. The target is designed as a gas jet of nearly homogenous density and allows to reach luminosities in the region of 10^{35} cm^{-2} s^{-1} [3]. The jet is of cylindrical shape with 4 mm in height and diameter [4]. The jet is produced by accelerating gas to supersonic speeds in a Laval nozzle perpendicular to the beam axis. A gas catcher is set up opposite to the Laval nozzle to collect the major part of the injected gas in order to keep vacuum conditions at a tolerable level. MAGIX is designed to operate with various elementary gases for fundamental physics experiments, e.g. the search for the dark photon as well as investigations on the proton form- and astrophysical S-factor [5]. The setup is shown in Fig. 1.

_____

* bledroi@uni-mainz.de
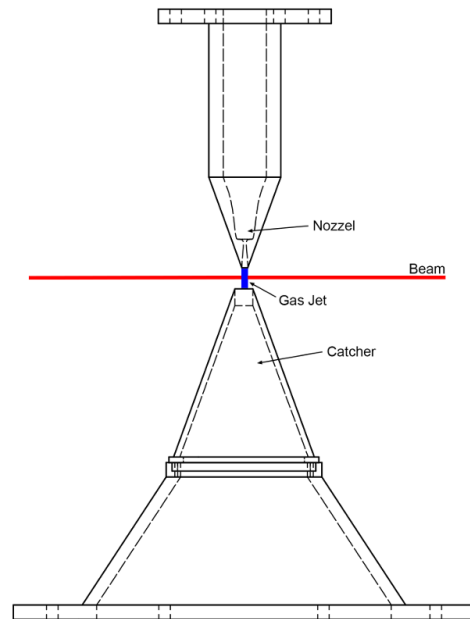
Figure 1: Schematic drawing of the MAGIX gas target [6].

Luminosity Limit Estimation

Target scattering and beam optics limit the luminosity of targets in ERL operation. Luminosity and target density limits for MAGIX can be estimated as presented in [7]. The luminosity limit then depends on beam and target properties as well as the beam power lost in the accelerator. It is therefore important to examine these parameters to ensure reliable ERL operation.

TARGET INDUCED HALO

Scattering on the gas target widens the angle and energy distribution of the electron beam in a way that a halo forms around the original beam cross-sectional area as shown in Fig. 2. The halo is therefore called "Target Induced Halo" (TAIL). TAIL might cause malicious beam dynamical behavior when passing the cryomodules, such as inducing Higher Order Modes (HOMs) in the cavity, or directly damage machine parts when electrons get dumped in the cavities and beam pipes. Radiation produced by dumping electrons may further lead to damage especially to electronic components and generate background noise in the detectors of the experiments reducing measurement precision. It is therefore crucial to carefully investigate on the effects originating from the beam passage of MAGIX and formulate a collimation approach downstream the target to encounter impacts on machine operation safety and reliability. The collimation contributes to power losses as described above and have to be minimized in order to maximize luminosity available for the experiment.
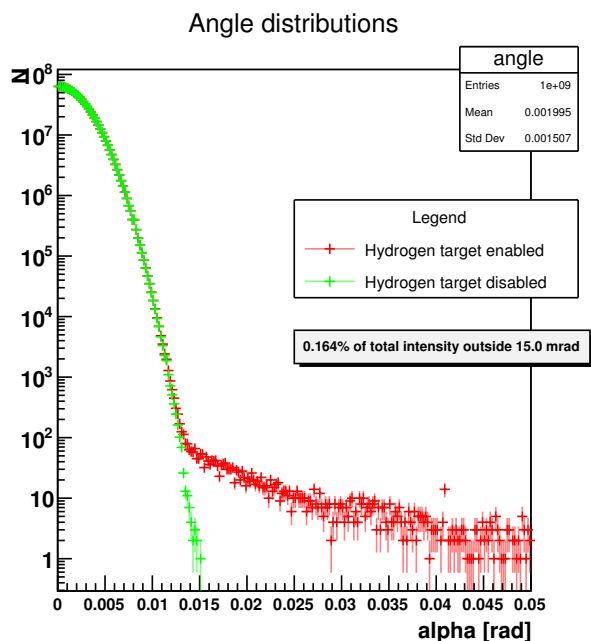
Figure 2: Geant4 simulation of the angle distributions with (red) and without (green) a hydrogen target as designed for MAGIX. TAIL region starts at 15 mrad.

Simulation of the MAGIX target

Statistical scattering models such as the Moliere distribution in practice quickly get complicated to evaluate owing to the degree of idealization on which these models are based. Simulating the target hence is a key part in understanding the formation of the TAIL. The Open Source simulation toolkit Geant4 is used for this purpose since it offers the greatest flexibility, high precision and high performance in simulating passage of particles through matter. The simulation is developed on an Intel Core i7 workstation providing four cores and eight threads allowing to run simulations in multithreaded mode to reduce runtime significantly. By now the design parameters of the MAGIX target are not finalized, hence the development process has concentrated on performance optimization and automation rather than generating results. The simulation program is capable of processing beam, target and analysis configuration input on runtime and therefore improve the performance of the simulation routine when setup parameters are available. Furthermore efficient data handling and analysis is possible with the utilization of the ROOT analysis framework, which allows writing universal evaluation routines for popular scenarios.

Preliminary results

Although there are no final results, some qualitative statements on beam-target interaction can be made. Atomic hydrogen (H_2) with a particle density of 10^{19} cm^{-2} is used in this scenario. The beam transverse profile is modeled as an rotationally symmetrical 2-dimensional gaussian with $\sigma = 100\,\mu$m in width. Beam energy and angle distribu-

tions are gaussian with $E = 105$ MeV, $\sigma_E = 100$ keV and $\sigma_\alpha = 2.5$ mrad respectively. The beam RMS emittance is $0.25\,\pi$ mm mrad.

Angle distribution   The impact of target passage on the angle distribution is shown in Fig. 2. A mentionable broadening of the distribution is visible starting from ~ 14 mrad to higher angles. The region outside 15 mrad is identified with the TAIL region. A fraction of 1.64 ‰ of the total intensity is scattered into this region in the case of a hydrogen target, which corresponds to losses of 172 W with 1 mA total beam current. These effects are expected to enlarge with higher mass target gases.

Energy distribution   Energy distributions before and after target passage have been extracted to investigate on the effects on the energy distribution. The distributions were fitted with gaussian distributions yielding no net widening of energy deviation in the region of the initial beam design energy. The scattering process yet produces low energy electrons potentially reaching downstream accelerator sections as shown in Fig. 3. By now there is no correlation analysis between energy and angle available to get a clearer picture of the properties of TAIL electrons.
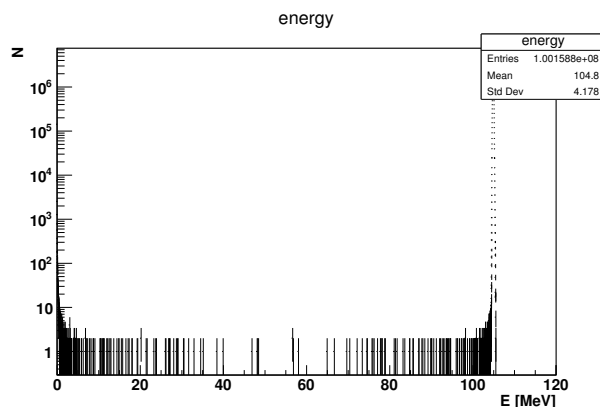
Figure 3: Electron energy spectrum after target passage. At beam energy are no visible changes, while few low energy particles are produced through scattering.

Phase space   Transverse phase spaces before and after target passage were extracted and RMS emittance ellipses fitted in ROOT as shown in Fig. 4. The fit parameters show that no net RMS emittance growth is observable at such low target densities. The effect of more dense gases has to be investigated.

COLLIMATION STRATEGY

Collimation should take place after the first dipole downstream from MAGIX as shown in Fig. 5. The dipole allows to filter low energy electrons and dispersion. Movable collimators in both transverse directions are planned to account for the use of several gases at MAGIX. Further studies on
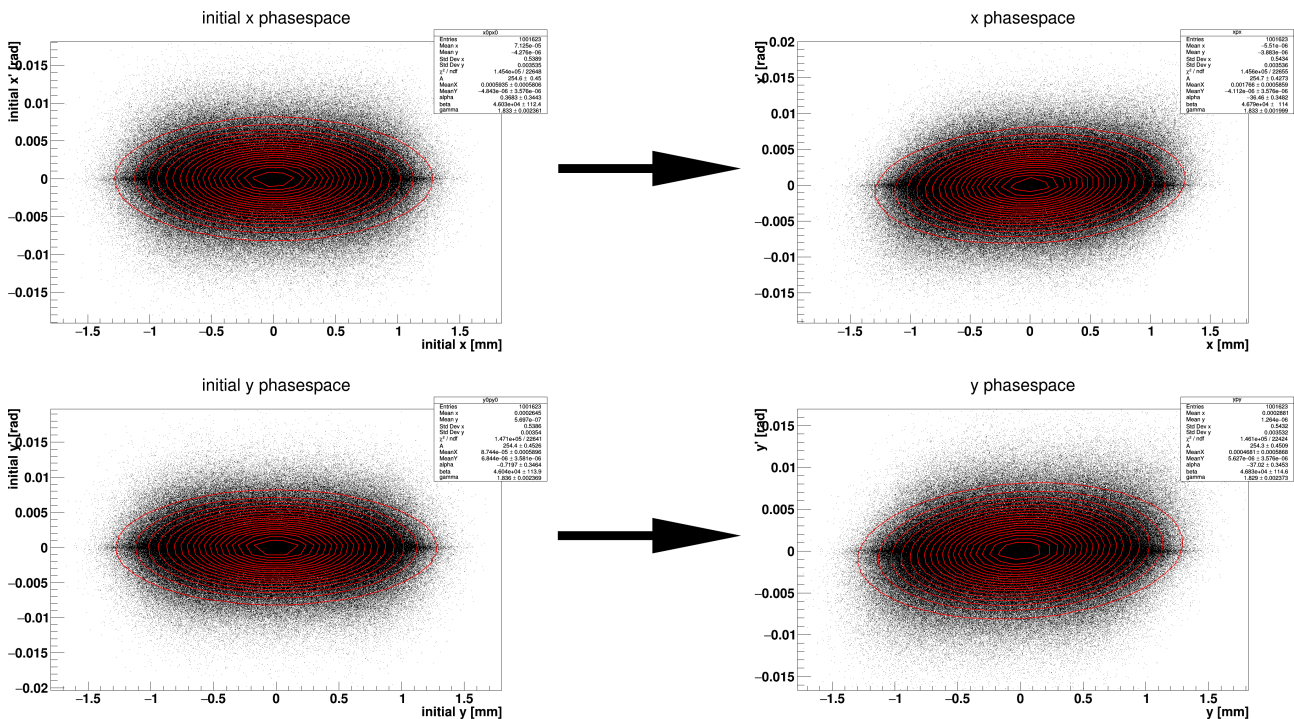
Figure 4: Transverse phase spaces before (left) and after target passage (right). The red RMS ellipses are fitted and show no RMS emittance growth.

the impact of different target gases have to be conducted to formulate a precise design of the collimation elements.
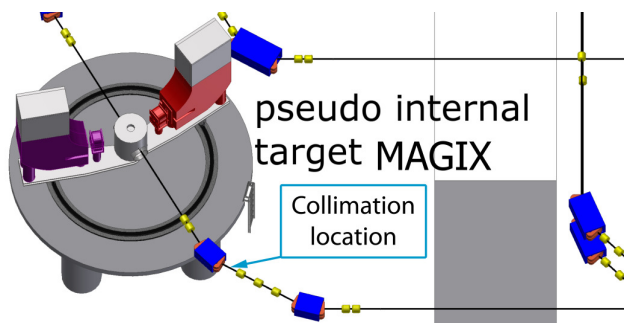
Figure 5: The region behind the first of the two foreseen deflection magnets seems to be favorable for collimation, lying neither in the direct line of sight to the target nor the cryomodules [1].

CONCLUSION

Simulation development as basis for this thesis has reached production level and rough statements on beam-target interaction could be made. The simulation process allows automated simulation routines to be run time efficient to prepare for when final design parameters are available for input. TAIL leads to significant beam losses potentially limiting the luminosity available for MAGIX, especially when operating with higher mass gases. When machine development is approaching the final design, more studies will be conducted to start collimation design. Collimator con-

struction will be accompanied with simulations of radiation levels caused by the collimation process. Collimation experiments are intended to be conducted at the Mainz Microtron (MAMI) before MESA is commissioned.

ACKNOWLEDGEMENT

REFERENCES

[1] T. Stengler *et al.*, "Status of the Superconducting Cryomodules and Cryogenic System for the Mainz Energy-recovering Superconducting Accelerator MESA" in *Proc. IPAC'16*, Busan, Korea, May 2016, paper WEPMB009.

[2] D. Simon, "Beamline Design for MESA", Diploma thesis, Institute for Nuclear Physics, Johannes Gutenberg-University, Mainz, Germany, 2014.

[3] MAGIX group, private communication, Jun. 2017.

[4] S. Aulenbacher, private communication, Sep. 2016.

[5] K. Aulenbacher, "Nuclear Physics Experiments at MESA", presented at the 59th ICFA Advanced Beam Dynamics Workshop on Energy Recovery Linacs, CERN, Geneva, Switzerland, June 2017, this conference.

[6] MAGIX, http://wwwa1.kph.uni-mainz.de

[7] G. Hoffstaetter, "Applications for CBETA at Cornell", presented at the 59th ICFA Advanced Beam Dynamics Workshop on Energy Recovery Linacs, CERN, Geneva, Switzerland, June 2017, this conference.

LOW-ENERGY BEAM TRANSPORT SYSTEM FOR MESA*

C. Matejcek, K. Aulenbacher, S. Friederich, L. Hein, Institut für Kernphysik, Mainz, Germany

Abstract

An important part of the new accelerator MESA (Mainz energy-recovering superconducting accelerator) is the low-energy beam transport system connecting the 100 keV electron source with the injector accelerator. Here the spin manipulation and the bunch preparation for the injector accelerator take place. Due to the low energy, space charge will be an challenging issue in this part. Therefore, start-to-end simulations were done with a combination of the two particle dynamics codes PARMELA [1] and CST [2]. At the moment, a test setup is being built up to check the functionality of devices and compare the beam parameters with the simulation. Here the focus lies on the bunch preparation system because at this part we expect high impact of the space charge by reason of the necessary bunch compression. The advance of the test setup, the simulations and measurements done so far will be shown.

INTRODUCTION

A layout of the lattice of MELBA (MESA low-energy beam apparatus) can be seen in Figure 1. The electrons will be focused by quadrupoles and solenoids. Two times the beam will be bended by 270° by two alpha magnets. Several steerer magnets will correct the orbit of the electrons if it deviates from the reference orbit. Misalignment of the devices and magnetic stray fields will lead to such a deviation. One important part of MELBA is the spin manipulation consisting of two Wien filters and one solenoid. After the electrons are produced in the source, their spin is oriented in the longitudinal direction. The first Wien filter and the

solenoid will align the spin in the horizontal direction. Compensation of further precession in the accelerator will be done by the second Wien filter. In principle the spin can be aligned in any direction with this arrangement. The reason for manipulation of the spin in this section is that the rotation angle of the Wien filter $\phi_{\text{spin, Wien}} \propto \frac{1}{\beta\gamma^2}$ and that of the solenoid $\phi_{\text{spin, sole}} \propto \frac{1}{\beta\gamma}$ [3]. So the required fields for spin rotation are small in this section. A challenging issue in this low-energy region is the transport of moderate bunch charges ($O(1\,\text{pC})$) demanded by the experiment MAGIX (MESA gas internal target experiment). This is due to the fact that the space charge forces scale with $\frac{1}{\gamma^3}$. For offline characterisation of the beam, there are scanners installed, whereas for the online characterisation, there will be a xy monitor and a phase monitor. The second big part is the chopper and the buncher system responsible for matching the beam with the longitudinal acceptance of the injector where the beam will accelerated to an energy of 5 MeV. The chopper system consists of two circular deflecting cavities with a resonance frequency of 1.3 GHz, a solenoid ,and a collimator. For longitudinal bunching also two cavities are used, the first one with a resonance frequency of 1.3 GHz and the second one with double the frequency.

SIMULATIONS

Alpha magnet

First the alpha magnet was modelled and simulated with CST (Computer simulation technology) to calculate the elements of the transport matrix. In Figure 2, the results are shown and compared with old simulations of Ref. [4]. The simulated magnet deflects the electrons by 270° in the horizontal plane. The discrepancy between the two results may explained by the fact that different algorithms are used. Furthermore the position of the beginning and the end of the alpha magnet can be different. The operating point will be chosen between 300 and 400 G to have little focusing in the x-direction and little dispersion. Furthermore the optical properties in both planes are quite similar.

Start-to-end

Simulation of the whole beamline is done successively with PARMELA (Phase and radial motion in electron linear accelerators) and CST. Both are particle in cell (PIC) codes. The resulting particle distribution of one program is used as a start distribution for the other one. In a first simulation, the source was simulated with CST [5] followed by a simulation with PARMELA of the beamline from the source to the first alpha magnet, which again is simulated with CST. The beamline downstream to the second alpha magnet, which is also simulated with CST, is simulated with PARMELA. The last part from the second alpha magnet to the injector
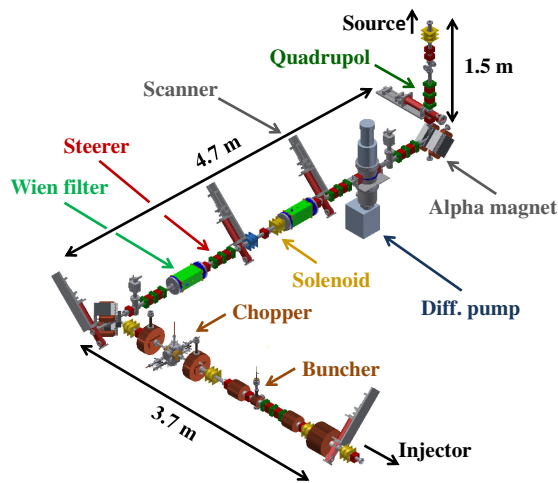
Figure 1: Layout of the low energy beam transport system for MESA.
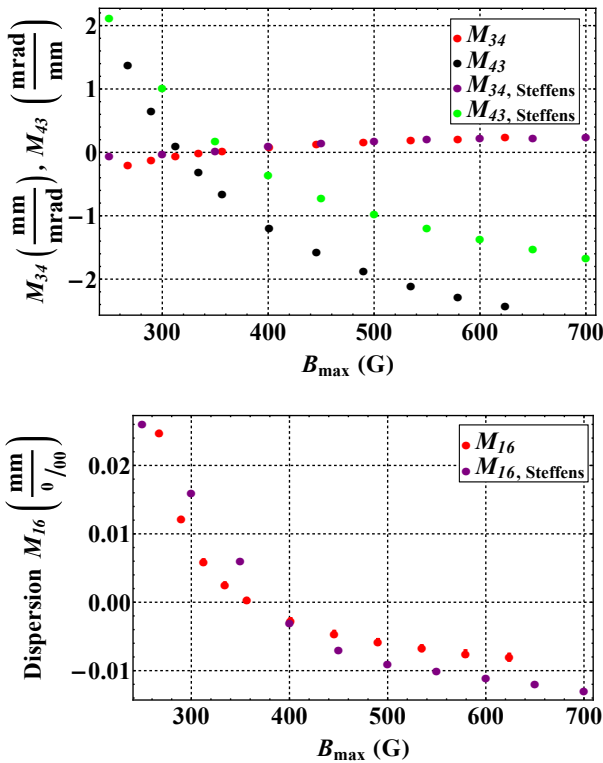
Figure 2: Elements of the transport matrix of the alpha magnet for different magnetic fields for an energy of 100 keV.

is simulated with PARMELA (see Fig. 3). Table 1 lists the beam parameters at the end of MELBA for 1.3 mA and 10 mA. For the smaller current, the beam has symmetric parameters in the x and the y plane, the emittances stay below our goal of 1.0 mm mrad, the loss of particles is 0 %.
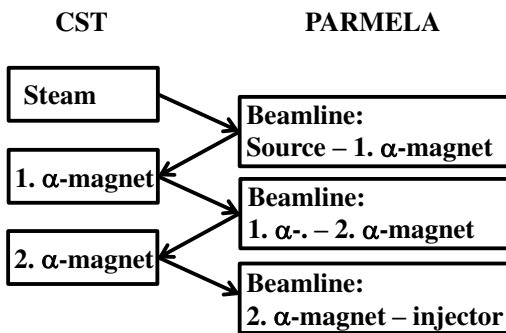
Figure 3: Parts of the beamline simulated with the two PIC codes CST and PARMELA.

In contrast, the parameters are higher and asymmetric, the goal of 1.0 mm mrad is exceeded, and there is a tremendous loss of 31.2 % with a beam current of 10 mA. The reason is the much higher space charge force, which can also be seen in Figure 7. Here in the xx' and yy' phase space of the

Table 1: Beam parameter at the end of MELBA, in front of the injector for two different currents. 1.3 mA and 10 mA correspond to 1 pC and 7.7 pC of bunch charge.

	1.3 mA	10 mA
x_{rms}	1.429 mm	1.713 mm
y_{rms}	1.442 mm	1.396 mm
x'_{rms}	5.887 mrad	6.190 mrad
y'_{rms}	5.854 mrad	4.804 mrad
$\epsilon_{x,rms,n}$	0.576 mm mrad	1.165 mm mrad
$\epsilon_{y,rms,n}$	0.484 mm mrad	1.111 mm mrad
$\Delta\phi_{rms}$	2.044°	3.947°
$\Delta E_{kin,rms}$	1.777 keV	2.084 keV
Loss of particle	0 %	31.2 %
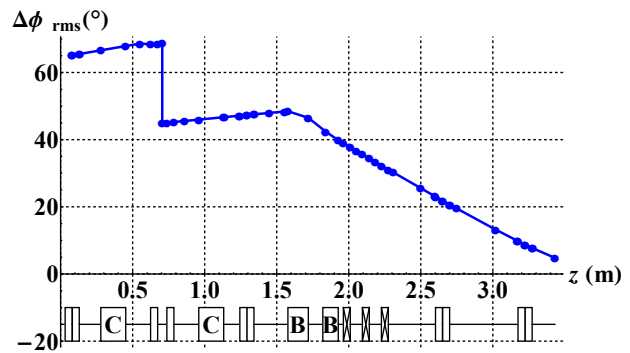
Figure 4: Longitudinal dimension along the beamline from the second alpha magnet to the injector for 10 mA.

10 mA beam, a strong filamentation is recognizable that is the result of the nonlinear space charge force.The explanation for the huge loss of particles is the natural elongation of the bunches due to the space charge. During the first 7.4 m of beamline from the source to the chopper system the longitudinal dimension ϕ_{rms} of the beam increases from 24° to 69°. The chopper system allows the passing of particles only with
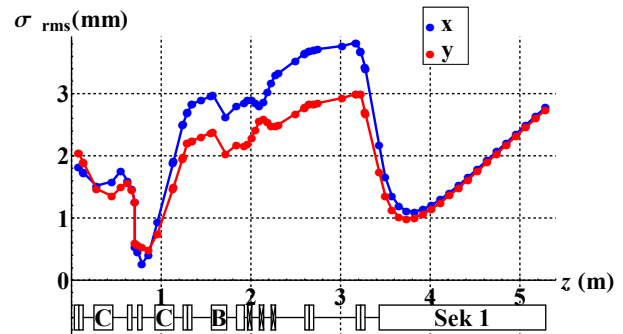
Figure 5: Transverse dimension along the beamline from the second alpha magnet to the end of the first section of the injector for 10 mA with 31.2 % of beam loss at the chopper collimator.

a maximum longitudinal phase distribution of ±80° around

the reference phase to match the beam with the longitudinal acceptance of the buncher system. Figure 4 depicts the rms value of the longitudinal dimension of the beam along the last part of the beamline behind the second alpha magnet. At the position of the collimator of the chopper system, a drop is observable. Nearly the complete loss of 31.2 % is dumped here as the beam has excessive longitudinal dimension. The decreasing longitudinal dimension afterwards is because of the longitudinal focusing of the buncher system. In addition the longitudinal focusing of the buncher causes increasing transverse space charge forces in front of and inside the injector. To avoid losses in this region, the transverse dimensions of the beam will be very large to minimize transverse space charge forces and then direct in front of the injector the beam will be strongly focused. With this the remaining 6.8 mA can pass the first section of the injector which depicts figure 5. In order to increase the possible beam current, decrease emittance growth and bunch elongation, the transverse beam size along the beamline should in general be as large and constant as possible. An approach to estimate the bunch
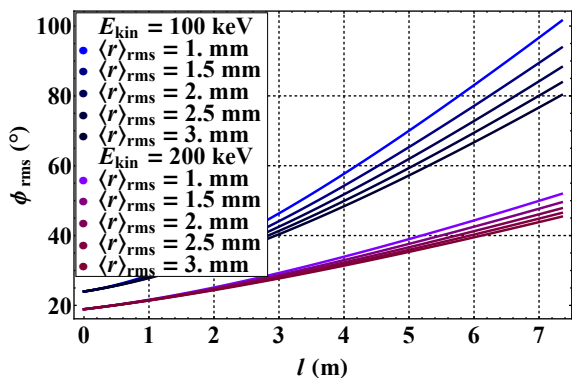
Figure 6: Bunch elongation along the beamline to the chopper collimator for 10 mA.

elongation can be the K-V equation [6]. In the transverse planes the dimensions were assumed to stay constant. Figure 6 shows the advantage of higher beam energy, larger average beam size, and shorter beamline.

Simulations of the whole beamline from the source to the injector show that 1.3 mA of beam current are possible to transport to the injector, whereas 10 mA are not because of the strong defocussing due to space charge.

STATUS MELBA

Currently, the source and the vertical part of MELBA consisting of a solenoid, a quadrupole triplet, a scanner, an alpha magnet and a part of the horizontal beamline consisting of two quadrupole triplets, a second scanner, and a differential pumping station is built up and baked out. The beamline ends with a small beam dump. The overall length is about 4 m. A sketch of the beamline can be seen in figure 8.
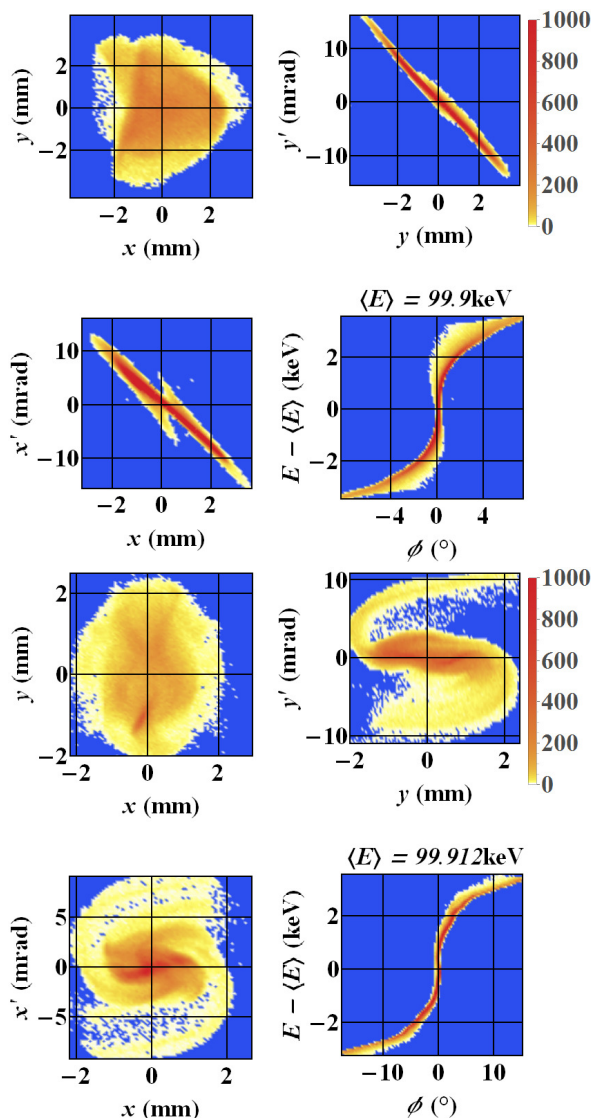
Figure 7: The upper four figures show the phase space for 1.3 mA and the lower ones the phase space for 10 mA. The unit of the legend is number of particle.
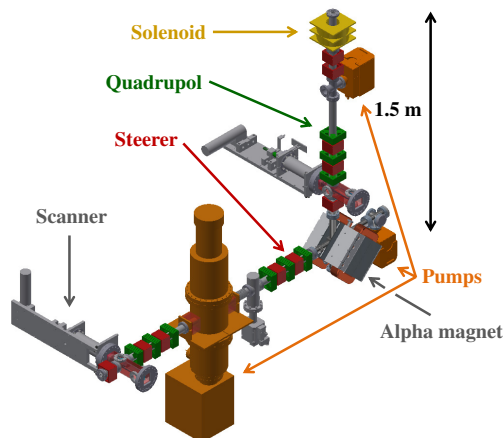
Figure 8: Current test setup of MELBA.

Diagnostics

At the moment, the only beam diagnostic devices are scanners. In comparison to the latest model of scanner at the institute, the needed bellows are guided to avoid twisting, and the target vacuum chamber is larger to allow the welding of a larger window flange to get a better sight inside. The available instruments are scintillator monitors made of YAG:Ce, wires (300 µm), and grids (25 µm). The scintillator monitors are couted with aluminium to ensure discharging of the electrons. A picture of them can be seen in Figure 9 (see also [7]). In addition to that, a moveable slit (71, 200 µm) was installed in the beamline 942 mm downstream of the source allowing to measure the emittance by shifting the beam over it by magnetic deflection. These techniques are similar to the ones in [8].
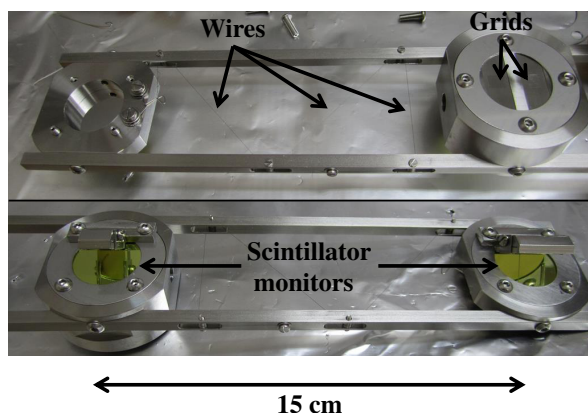
Figure 9: Mount with the diagnostic instruments. At the top the front of the instruments and at the bottom the back.

Vacuum System

As mentioned before, there is a differential pumping station [9] ensuring a good vacuum on the source side. Upstream to the source, there are two additional IGPs (ion getter pumps) and two pneumatic valves, which can separate the vacuum of the beamline. After baking out the whole beamline the pressure upstream of the differential pumping station reached 3×10^{-10} mbar and downstream 4×10^{-10} mbar. The pressure in vacuum chamber of the source stays on a lower level, namely 6×10^{-12} mbar. This is important to ensure a longer lifetime of the cathodes.

Quadrupoles

Since the Wien filters have an asymmetric aperture and one is very small, the use of quadrupoles was choosen. The beam will be focussed stronger in one plane in order to minimize space charge forces in the Wien filter. The yokes of the used quadrupoles are made of alternating aluminum and μ-metal plates. On the one hand this fabrication method allows a small remance and on the other hand an increased length of homogeneous field compared to the fringe field.
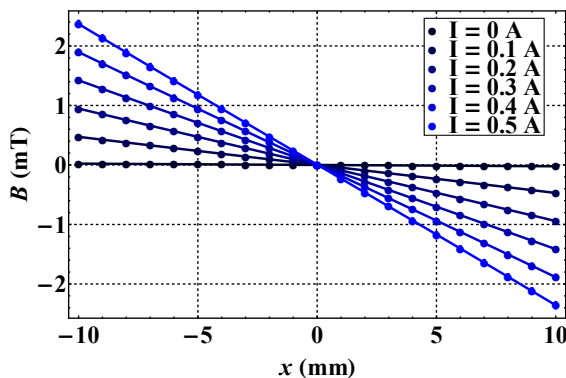
Figure 10: Measurement of the magnetic field along the transvers axis yields $\frac{dB}{dx \cdot I} = 0.4688(4)\,\mathrm{T\,m^{-1}\,A^{-1}}$.

Chopper System

An essential part of the chopper system are the cavities that deflects the beam circularly. The prototype [10] was improved by using copper instead of indium gaskets so the cavities are bakeable. Furthermore, the tuner flange now has the correct thickness for a better tuning of the cavity.
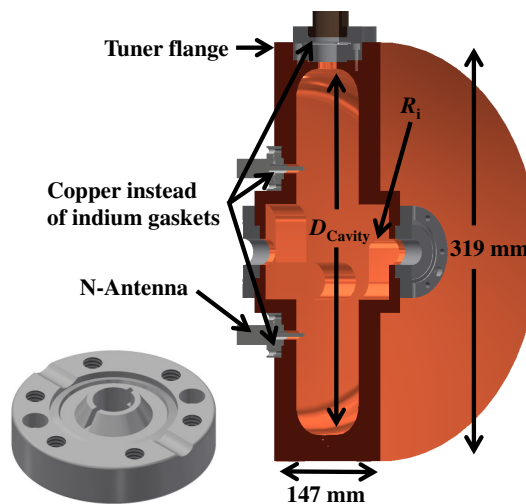
Figure 11: Half view of one chopper cavity.

Manufacturing is done in several steps, because only with the correct geometric form the resonance frequency and the field shape are the required ones, namely 1.3 GHz and a circular-deflecting field. With the chopper cavities the opportunity was taken to test flanges with nose cones shown in figure 11. They can help to avoid wake fields. Figure 12 shows electric field measurements (blue) and simulations with the current geometry (red) and the nominal field (black) before the last fabrication step of the cavities. In order to measure the field, a bead is pulled through the cavity, disturbing the field. This leads to an shift of the resonance frequency Δf which is proportional to E^2. Additionally the behaviour of the frequency while moving the tuner was measured. Figure 13 presents the measurement, that is in good agreement with the simulation result of $1.455 \times 10^5\,\mathrm{Hz\,mm^{-1}}$. More-

MOPSPP008
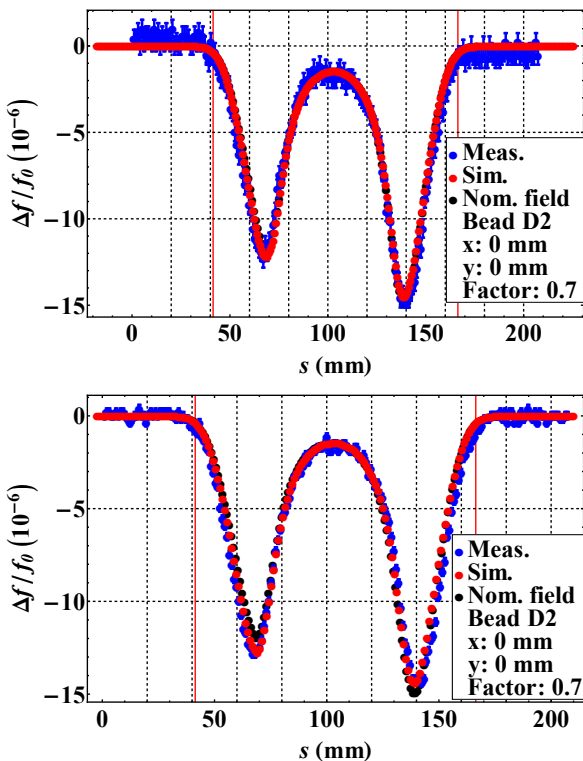
Figure 12: Measurements and simulations of the electric field on the reference axis in the chopper cavities.
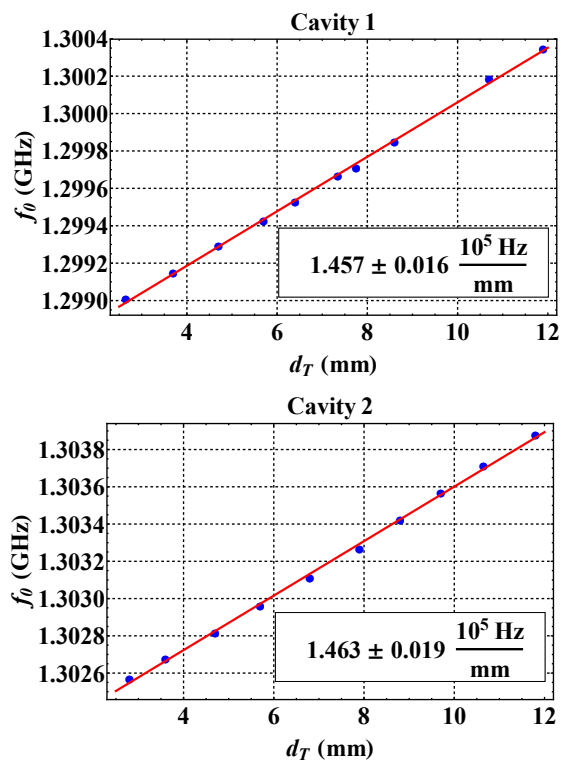
Figure 13: Tuner range measurement with line of best fit.

over the collimator system and the solenoids are fabricated and tested ([11], [12]).

CONCLUSION

In the first stage of MESA the current will be limited to about 1 mA since the modified ELBE (Elektronen Linearbeschleuniger für Strahlen hoher Brillanz und niedriger Emittanz) Cryomodules foreseen for the main accelerator cannot stand the HOM (higher order modes) power of currents significantly exceeding this value [13]. The analysis in the second chapter show that operating MELBA at the relatively low kinetic energy of 100 keV is compatible with this conditions. However, operating at currents of the order of 10 mA, planned in second stage of MESA, require either a source providing electrons with higher energy or a shorter low energy beamline. The latter will result in lower flexibilty concerning spin rotation. The source and first 4 m of beamline of MELBA have successfully been built up. The next steps will be the krypton gas processing of the source, assembling a LASER system, implementation of the control system and an interlock system. After first measurements, the beamline will be extended with the chopper and buncher system to prove their functionality.

REFERENCES

[1] PARMELA, Phase and radial motion in electron linear accelerators, 2005

[2] CST STUDIO SUITE 2016, Computer simulation technology

[3] K. Aulenbacher, *Erzeugung intensiver hochpolarisierter Elektronenstrahlen mit hoher Symmetrie unter Helizitaetswechsel*. Mainz, Germany, Shaker, 2007.

[4] K. Steffens, "Konzeption und Optimierung eines 100 keV Injektionssystems zur Erzeugung eines longitudinalen polarisierten Elektronenstrahls an MAMI", Ph.D. thesis, Phys. Dept., Institut für Kernphysik, Mainz, Germany, 1993.

[5] S. Friederich and K. Aulenbacher, "The Small Thermalized Electron source At Mainz STEAM", in *Proc. ERL'17*, Genf, Switzerland, June 2017, paper MOPSPP005.

[6] M. Reiser, *Theory and Design of Charged Particle Beams*. Weinheim, Germany, Wiley-VCH, 2008.

[7] I. Alexander, K. Aulenbacher, V. Bechthold, B. Ledroit, and C. Matejcek, "Diagnostic test-beam-line for the mesa injector", in *Proc. ERL'15*, Stony Brook, NY, USA, June 2015, paper THIALH2069, pp. 91-96

[8] E. D. Cantero, W. Andreazza, E. Bravin, A. Sosa, "The status of beam diagnostics for the HIE-ISOLDE linac at CERN", in *Proc. IBIC'14*, Monterey, CA, USA, September 2014, paper WEPF13, pp. 565-568

[9] A. Bünning, "Auslegung einer differentiellen Pumpstufe für das niederenergetische Strahlführungssystem am Mainz energy-recovering superconducting accelerator",

Diploma thesis, Phys. Dept., Institut für Kernphysik, Mainz, Germany, 2016.

[10] V. Bechthold, "Eine Deflektor-Kavität für den MESA-Beschleuniger", Diploma thesis, Phys. Dept., Institut für Kernphysik, Mainz, Germany, 2013.

[11] C. Stoll, "'Solenoid-Fokussierungsmagnete für den niederenergetischen Strahltransport an MESA"', Master thesis, Phys. Dept., Institut für Kernphysik, Mainz, Germany, 2016.

[12] B. Ledroit, "Aufbau und Test des MESA-Choppers", Master thesis, Phys. Dept., Institut für Kernphysik, Mainz, Germany, 2016.

[13] F. Schlander, K. Aulenbacher, R. Heine, and D. Simon, "Investigation of cryomodules for the Mainz energy-recovering superconducting accelerator MESA", in *Proc. IPAC'14*, Dresden, Germany, June 2014, paper WEPRI013, pp. 2505-2507.

BEAM BREAKUP SIMULATIONS FOR THE MESA ACCELERATOR

C. P. Stoll*, F. Hug, D. Simon, Institut für Kernphysik, JGU Mainz, Germany

Abstract

MESA is a recirculating superconducting accelerator under construction at Johannes Gutenberg-Universität Mainz. It will be operated in two different modes: the first is the external beam (EB) mode, where the beam is dumped after being used at the experiment. The required beam current in EB mode is 150 μA with polarized electrons at 155 MeV.

In the second operation mode MESA will be run as an energy recovery linac (ERL) with an unpolarized beam of 1 mA at 105 MeV. In a later construction stage of MESA the achievable beam current in ERL-mode shall be upgraded to 10 mA. To understand the behaviour of the superconducting cavities under recirculating operation with high beam currents simulations of beam breakup have to be performed. Current results for transverse beam break up calculations and simulations with Beam Instability (bi) [1] code are presented.

INTRODUCTION

The Mainz Energy-recovering Superconducting Accelerator (MESA) is currently being built at Johannes Gutenberg-Universität Mainz. The accelerator will be constructed in a double sided layout with two linacs and vertically stacked recirculation arcs. It will be operated in either an external beam mode (EB) with three recirculations or in an ERL mode with up to two recirculations.

Within this contribution we focus on the ERL operation mode which is planned to provide electron beams of 1 mA and later 10 mA at a beam energy of 105 MeV. With an injection energy of 5 MeV up to 100 MeV of beam energy can be recovered from the beam in ERL mode.

Further information on the MESA facility can be found in [2] and in [3]. A sketch of the lattice configuration can be seen in Fig. 1. As there are no SRF multiturn ERLs existing so far, investigations on beam stability in such an operation mode are accessible by simulations or theory only. A thorough understanding of beam stability is necessary for optimizing the layout of the accelerator before construction.
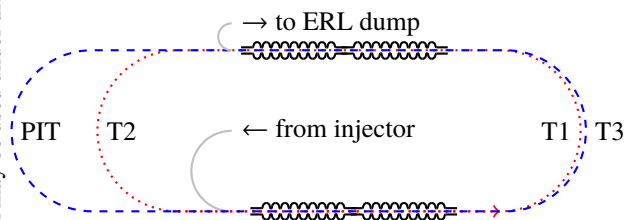
Figure 1: Lattice configuration for the ERL-mode of MESA. T1 to T3 are the return arcs for the different energies while the Pseudo Internal Target (PIT) arc contains the experiment and the 180° phase shift for the energy recovery mode.

SRF Cavities and Cryomodules

For MESA main accelerators two modified ELBE-type cryomodules were chosen [4], which each consist of two 9-cell superconducting radio frequency (SRF) cavities of the TESLA/XFEL-type. The modifications aim on the improved cw-operation of the cryomodules and include the integration of fast piezo tuners as well as an improved cooling of the HOM-coupler antennas [4].

The accelerating cavities will provide a gradient of 12.5 MeV at $Q_0 = 1.25 \times 10^{10}$ while being operated at 1.8 K and 1.3 GHz. A CAD model of the full cavity string is provided in Fig. 2. Besides the wanted accelerating π-mode, also unwanted HOMs with high quality factors can exist in the cavity. For the first calculations presented here the transverse BBU induced by dipole HOMs was investigated as quadrupole and higher order HOMs have weaker influence on the beam unless they are very strong with respect to the dipole HOMs.

Figure 2: CAD Model of the MESA cavity string. In the bottom center the two HF power couplers can be seen, the four other visible ports (bottom left and right, top center) are the HOM couplers.

TRANSVERSE BBU

Electron bunches that enter a SRF cavity with a small deviation from the reference orbit excite dipole HOMs in said cavity. Due to their naturally high Q_L, these modes can persist until the next bunch arrives at the cavity. The magnetic field of an excited mode deflects the following bunches that do not travel on the reference orbit. The deflection angle produced by the mode translates into a transverse displacement at the cavity after recirculation. The recirculated beam induces a HOM voltage, depending on the magnitude and direction of the beam displacement.
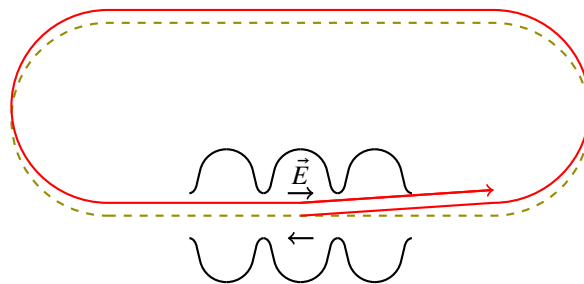
Figure 3: Orbit deviation (red) from the reference orbit (green) induced by dipole HOMs.

This can lead to a periodic unstable growth of the HOM voltage, which finally results in loss of the beam, see Fig. 3, and depends strongly on the bunch charge and thereby the average beam current [5]. Since the beam rigidity is proportional to beam energy, the first cavity behind the injection and the last cavity before the beam dump are of particular concern. This conclusion has been found as well for recirculating accelerators without energy recovery where transverse BBU has been investigated in the past for mictrotrons or normalconducting and superconducting few-turn linacs [6]. As a rule of thumb the onset current for BBU scales linear with the injection energy into the first cavity of the multi-pass linac when keeping the other parameters like recirculation optics or HOM frequencies and quality factors fixed [6].

THRESHOLD CURRENT IN ERLS

An important concept for the description of BBU behaviour is the so-called threshold current, which is the maximum beam current that can be safely transported through the lattice without the risk of beam loss. See Fig. 4 for a visualisation of this behaviour as produced with simulation data of bi.
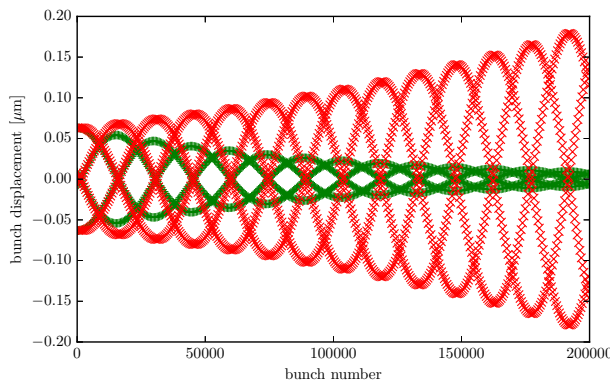
Figure 4: Bunch displacement as a result of subsequent bunches entering the cavity with a transverse offset. The points in green show the typical behaviour below the threshold current, in red an unstable beam current above the threshold. The data was obtained via bi simulation with an early iteration of the MESA lattice.

For multiturn ERLs, the threshold current for a single HOM was described by Hoffstätter et. al. in [7]:

$$I_{\text{th}} = -\frac{2c^2}{e\left(\frac{R}{Q}\right)_\lambda Q_\lambda \omega_\lambda} \frac{1}{\sum_J^{N_P} \sum_I^{N_P} \frac{1}{p_I} \sin(\omega_\lambda[t^I - t^J])T^{IJ}},$$

where I_{th} is the threshold current, $(R/Q)_\lambda$ and Q_λ the shunt impedance and quality factor of the HOM, ω_λ the frequency of the HOM, p the particle momentum and:

$$T^{IJ} = T_{12}^{IJ} \cos^2(\theta) + \frac{1}{2}(T_{14}^{IJ} + T_{23}^{IJ}) \sin(2\theta) + T_{34}^{IJ} \sin^2(\theta),$$

the transport line parameter from the end of one cavity to the end of the next. Assuming worst case for the recirculating

path length $\sin(\omega_\lambda[t^I - t^J]) = -1$ and with an approximation of the lattice matrix elements for a polarisation angle $\theta = 0$ via:

$$T^{IJ} = T_{12}^{IJ} = T_{12} = \sqrt{\frac{\gamma_i \cdot \beta_i \cdot \beta_f}{\gamma_f}},$$

some general information about the strength of certain HOMs and their importance can be obtained. As there are multiple HOMs existing in each cavity the threshold current obtained by using the formula described in [7] needs to be calculated multiple times for the complete HOM spectrum of the accelerating cavities. Doing so the most dangerous HOMs for a given recirculation optic setting can be found.

Wanzenberger et al. presented simulations of the TESLA/XFEL type cavity HOM spectrum in [8]. Those HOM parameters and the knowledge about the twiss β and Lorentz γ at the end of the first cavity and the start of the second were used to identify the most dangerous HOMs with respect to BBU for the MESA ERL. The obtained parameters are presented in table 1 for the two strongest HOMs, with approximated values for Q_{ext}.

Table 1: HOM parameters as stated in [8]

f [GHz]	R/Q [Ω]	Q_{ext}	θ
1.7391	58.604	$2 \cdot 10^4$	127.2°
2.5785	45.064	$5 \cdot 10^4$	11.6°

In table 2 the results for the corresponding threshold currents of the two most dangerous HOMs are presented using the calculation from [7] at twiss $\beta_{i,f} = 10\,\text{m}$. In addition the simulated threshold values using the bi-code are given in table 2.

Table 2: Calculated and simulated threshold currents

f [GHz]	I_{theo} [mA]	I_{simu} [mA]
1.7391	6.11	14.43 ± 0.01
2.5785	2.14	75.35 ± 0.06

The threshold current values presented here should be treated with care. Firstly, the numerical calculation is a big simplification of the process and a worst case approximation. Secondly, the simulations are currently performed with an old iteration of the MESA lattice which is without injection and starts at 30 MeV. Scaling down the injection energy to 5 MeV the threshold current is exspected to be reduced by a factor of 6, which even in the worst case presented in table 2 still would be sufficient for achieving the 1 mA design current of MESA stage 1. For MESA stage 2 running at a design current of 10 mA further optimizations would be necessary.

At the moment, the HOM parameters for MESA are updated. As MESA uses TESLA/XFEL cavities the HOMs are expected to be very similar to those presented in [8]. Nevertheless these values need to be simulated again for the full

MESA cavity string also taking beamline elements, power couplers and HOM-couplers into consideration. Currently the new HOM simulations for the MESA cold string are being performed at TU Rostock. So far the values given in table 1 were used to further develop and test the bi framework for the twice recirculating double-sided MESA design.

Simulations with bi

The code bi uses beam tracking of point-like bunches through a 6×6 transfer matrix representation of the lattice. It calculates the beam position as a function of time and determines the threshold current by variation of the beam current.

A framework for bi was built in python, which handles an arbitrary number of HOMs and scans for the strongest, or performs frequency spread analysis of the HOMs. In reality, each cavity is produced with certain manufacturing tolerances. Since the frequencies of HOMs in a cavity strongly depend on the geometry of the cavity, every cavity can have slightly different HOM frequencies. Consequently the transverse phase advances throughout the recirculations vary slightly, which can increase the threshold current.

For this study, a sample of 4000 frequencies was used, where the frequencies were drawn from a uniform distribution with 1 MHz spread around 1739.1 MHz. Each frequency was assigned to one of the four cavities of MESA, and 1000 sample runs of bi were performed. The $R/Q = 58.604\,\Omega$ and $Q_0 = 20\,000$ were kept constant throughout the runs. The result of the simulation can be seen in Fig. 5. The threshold current without frequency spread was 14.43 mA, with frequency spread included the minimal threshold current was 21.49 mA. As expected an increased threshold current can be observed using more realistic cavity parameters in the simulations.
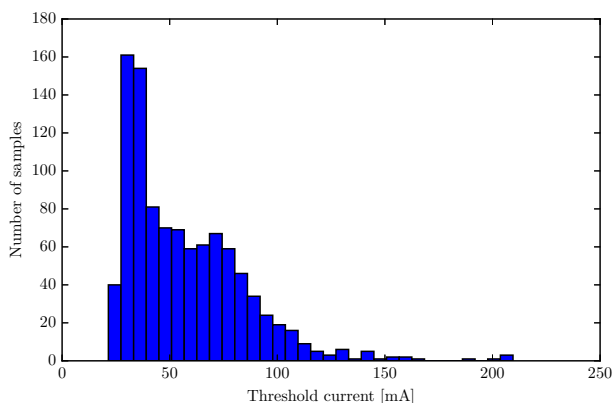
Figure 5: Threshold currents for 1000 runs with frequency spread of 1 MHz.

In all calculations and simulations performed so far the dampening effect of the HOM couplers was not considered, since it has not been measured or simulated for the MESA cryomodules yet.

CONCLUSION

The bi code for simulations of Beam Break Up for MESA was prepared. For future calculations the MESA lattice will be updated and the simulation will start at the injection energy of 5 MeV. As soon as new information on cavity parameters or lattice improvements are available, more realistic threshold currents for MESA can be obtained. Additional simulations with BMAD [9] are currently prepared and should be available soon to further prove the bi numbers. Furthermore with BMAD feedback and optimisation for finding the optimum lattice for maximum current will be possible. Currently, the critical point is the cavity right after injection and right before ejection since the lowest energy beam has the least rigidity. An optimisation of the injection optics will be performed.

REFERENCES

[1] Ivan V. Bazarov. bi - beam instability bbu code. http://www.lepp.cornell.edu/ ib38/bbucode/src.

[2] D. Simon, K. Aulenbacher, R. Heine, and F. Schlander. Lattice and beam dynamics of the energy recovery mode of the Mainz energy recovering superconducting accelerator MESA. *Proceedings of IPAC2015*, 2015.

[3] F. Hug, K. Aulenbacher, R. Heine, B. Ledroit, and D. Simon. MESA - an ERL project for particle physics experiments. *Proceedings of LINAC2016*, 2016.

[4] T. Stengler, K. Aulenbacher, R. Heine, F. Schlander, D. Simon, M. Pekeler, and D. Trompetter. Modified ELBE type Cryomodules for the Mainz Energy-Recovering Superconducting Accelerator MESA. *Proceedings of SRF2015*, 2015.

[5] E. Pozdeyev, C. Tennant, J. J. Bisognano, M. Sawamura, R. Hajima, and T. I. Smith. Multipass beam breakup in energy recovery linacs. 2005.

[6] Roy E. Rand. *Recirculating Electron Accelerators*. harwood academic publishers, 1984.

[7] Georg. H. Hoffstätter and Ivan V. Bazarov. Beam-breakup instability theory for energy recovery linacs. *Physical Review Special Topics - Accelerator and Beams*, 7(054401):13, May 2004.

[8] R. Wanzenberg. Monopole, dipole and quadrupole passbands of the tesla 9-cell cavity. 2001.

[9] D. Sagan. Bmad: A relativistic charged particle simulation library. *Nuclear Instruments & Methods in Physics Research A, 558*, 2006.

DEVELOPMENT OF A MULTIALKALI PHOTOCATHODE DC GUN FOR HIGH CURRENT OPERATION

N. Nishimori[#], Tohoku Univ., 1-2-1 Mikamine, Taihaku, Sendai, Miyagi 982-0826, Japan
R. Nagai, M. Sawamura, R. Hajima, QST, Tokai, Naka, Ibaraki 319-1195, Japan

Abstract

We have developed a DC gun test stand at National Institutes for Quantum Radiological Science and Technology (QST) for high current electron beam generation. The gun test stand consists of an alkali antimonide photocathode preparation chamber, a DC gun with a 250kV-50mA Cockcroft Walton high voltage power supply, and beam line with a water cooled beam dump to accommodate 1.5 kW beam power. We successfully fabricated a Cs_3Sb photocathode with quantum efficiency of 5.8 % at 532 nm wavelength and generated 150 keV beam with current up to 4.3 mA with 500 mW laser at 532 nm wavelength. Unfortunately, we encountered a vacuum incident during beam transport of high current beam and the development has been halted. We will fix the vacuum problem and restart the gun development as soon as possible.

INTRODUCTION

A high-brightness and high-current electron gun has been developed worldwide for the next generation light sources such as a high power EUV FEL for semiconductor lithography based on an energy recovery linac (ERL) [1]. Such a gun can also be used as a compact and high-power THz light source based on coherent Smith Purcell radiation technique in combination with an appropriate grating [2].

We have developed a photoemission DC gun test stand at National Institutes for Quantum Radiological Science and Technology (QST) for generation of high-brightness and high-current electron beam [3]. An alkali antimonide photocathode preparation system was added to the gun test stand, because electron beam generation with current up to 75 mA was demonstrated at the Cornell photoinjector and the charge lifetime of the multialkali photocathode was measured to be greater than 15 kC [4].

In this paper, fabrication result of a Cs_3Sb photocahode is reported. The preparation chamber for Cs_3Sb photocahode has been developed since 2013 [3]. The quantum efficiency (QE) in our latest fabrication reached 5 %, which was more than 15 times greater than our previous value [3]. A photoemission gun system has been prepared for beam generation. A cathode electrode was replaced to accommodate a photocathode puck compatible with the compact ERL (cERL) at KEK as well as to reduce the surface electric field [3]. High voltage at 210 kV has been successfully applied with cathode electrode in place for more than eight hours without any discharge. A beamline for high current beam generation has also been

n_nishim@tagen.tohoku.ac.jp

prepared. We have generated electron beam from the Cs_3Sb photocathode with current up to 4.3 mA at 150 kV. The results of beam generation are described.

FABRICATION OF CAESIUM ANTIMONIDE PHOTOCATHODE

Details of our alkali antimonide photocathode preparation chamber are described elsewhere [3]. The QE obtained in the first fabrication in March 2015 was 0.37 % at 532 nm. The QE decreased to almost zero one year later, though the puck had been kept under vacuum pressure of 2×10^{-9} Pa. A silicon wafer of 0.5 mm thickness is used as the substrate. We decided to reactivate the Si wafer with similar way with our previous procedure. The wafer was heat cleaned at 550-degree C for two hours. The evaporation of antimony and caesium was performed another day.

Figure 1 shows our fabrication procedure. The distance between the wafer and alkali and antimony sources is 3 cm. The temperature during the fabrication was monitored with a thermocouple connected to the puck holder. The antimony was evaporated at monitor temperature of 140-degree C. The duration of evaporation time which
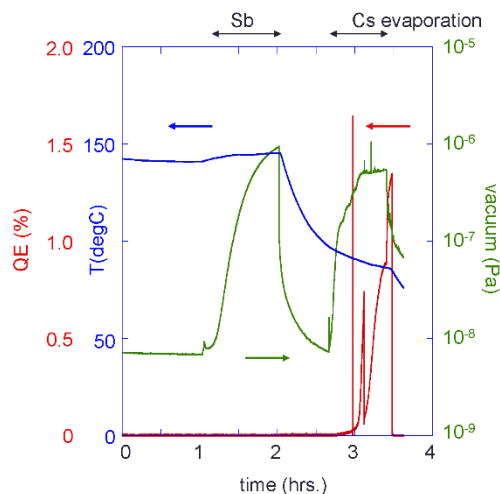
Figure 1: The Cs_3Sb photocathode fabrication procedure. The blue curve shows temperature of puck holder measured with a thermocouple. The green curve shows the vacuum pressure in the fabrication chamber. The antimony is evaporated at the monitor temperature of 140-degree C and caesium is evaporated at 90-degree C. The QE (red curve) is derived from photo current measured with a charge collector in front of a Cs_3Sb photocathode and laser power at 532 nm.

Figure 2:   Gun test stand for high current beam generation at QST. The test stand consists of an alkalai antimonide photocathode preparation chamber, a 250kV dc gun, and a beamline.

corresponds to 40 nm of antimony was calibrated in a separate experiment with a thickness monitor. After the antimony evaporation, the monitor temperature was decreased to 90-degree C for the caesium evaporation. A laser with maximum power of 5 mW was used for the present photo current measurement, while the maximum laser power was 125 μW in the previous fabrication. This allowed us to detect small amount of photo current increase. Once the photo current increase was detected, the heater power for caesium evaporation was increased until optimum condition was established and the laser power was decreased with ND filter. We stopped the caesium evaporation when QE exceeded 1 %. The QE reached 2.5 % two days later. The amount of QE is one order of magnitude higher than our previous value and reaches similar values of Ref. [5] and a textbook [6].

The reason why the QE increased one order of magnitude is unclear at this point. The Cs_3Sb fabrication process is similar and the same wafer is used. The differences are substrate temperature during caesium evaporation and laser power to monitor the photo current. The caesium temperature was roughly 20-degree C below the previous procedure. The increased laser power was helpful for small signal detection.

GUN TEST STAND

We have a dc gun with a 250kV-50mA high voltage power supply (HVPS), as shown in Fig. 2. The gun has been originally developed as a dc gun equipped with a GaAs photocathode to establish fundamental technologies for high-brightness and high-current beam generation for future light sources. Generation of 1 μA beam at 180 kV from a GaAs photocathode was already demonstrated. The details of the gun are described in Refs. [7,8]. The gun system consists of a SF6 tank, a high voltage chamber, a GaAs preparation chamber. The alkali antimonide photocathode preparation system was connected to the GaAs preparation chamber. The gun cathode electrode was replaced to accommodate a photocathode puck compatible with the cERL as well as to reduce the surface

electric fields for high voltage operation. The details of electric field calculation and high voltage test without cathode electrode are described elsewhere [3]. Figure 3 shows the high voltage holding test with cathode electrode in place. The high voltage at 210 kV has been successfully applied for eight hours without any discharge.

We also prepared a beam line shown in Fig. 2 for high current beam generation. The beam line consists of a solenoid magnet followed by a bending magnet, a differential pump system, a beam profile monitor, and a beam dump. Laser beam is injected through a window of the bending magnet chamber onto the photocathode. The differential pump system is used to separate the gun vacuum from the beam dump vacuum. The beam dump is water cooled to handle 1.5 kW beam power and is surrounded by lead radiation shield blocks. The transverse beam size at the beam dump is expanded by a beam expander magnet.
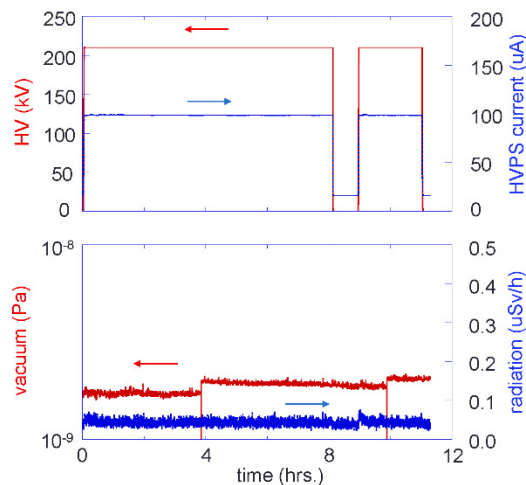
Figure 3:   High voltage (HV) holding test with cathode electrode in place. Top shows HV (red curve) and HVPS current (blue curve). Bottom shows vacuum pressure (red curve) and radiation (blue curve).
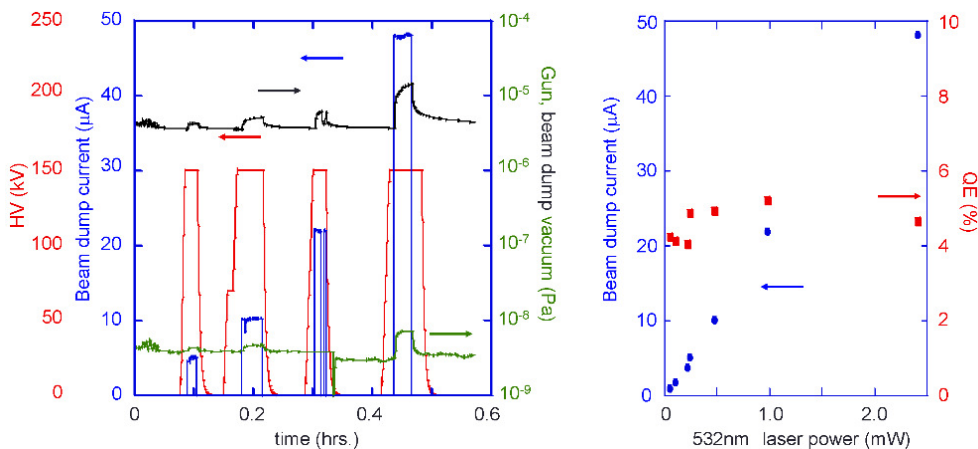
Figure 4:   The left figure shows beam current (blue curve) measured at a beam dump, high voltage (red curve), gun vacuum (green curve) and beam dump vacuum (black curve). The right figure shows beam dump current (blue circles) and QE (red squares) as a function of laser power at 532nm. The laser with maximum power of 5 mW is used for this measurement.

BEAM GENERATION

The first beam generation test was performed in April 2016, one week after the Cs_3Sb photocathode fabrication. After beam profile was observed at the monitor, beam current was measured at the beam dump. The beam current was 1.26 μA for 51 μW laser power at 532nm. This corresponds to QE of 5.8 %. The QE was twice higher than the value measured at the fabrication chamber, even after the photocathode was transferred to the gun chamber from the fabrication chamber. This indicates QE increased under XHV vacuum condition, or photocurrent was not correctly captured in the charge collector in the fabrication chamber. The QE value was derived from the laser power measured in front of the window of the bending magnet and beam dump current.

The second beam generation test with 5 mW laser at 532 nm was performed in August 2016 after the beam dump

was surrounded with lead radiation shield blocks. The beam dump current was measured as a function of laser power, as shown in Fig. 4. The beam dump current was 48 μA for 2.4 mW laser power at 532nm. This corresponds to QE of 5 %. This indicates the dark lifetime of our Cs_3Sb photocathode over four months is pretty long. The QE value was almost constant irrespective of laser power, as shown in Fig 4. The gun high voltage was set to 150 kV, and the gun vacuum pressure was 4×10^{-9} Pa when the beamline valve just after the gun was open. Although the vacuum pressure at the beam dump was three orders of magnitudes higher than that of the gun, the increase of the gun vacuum pressure was roughly twice thanks to the differential pump system.

The third beam generation test was performed in November 2016, after we installed 3W laser at 532 nm for high current beam generation and a water cooling system for the beam dump. Figure 5 shows the beam generation
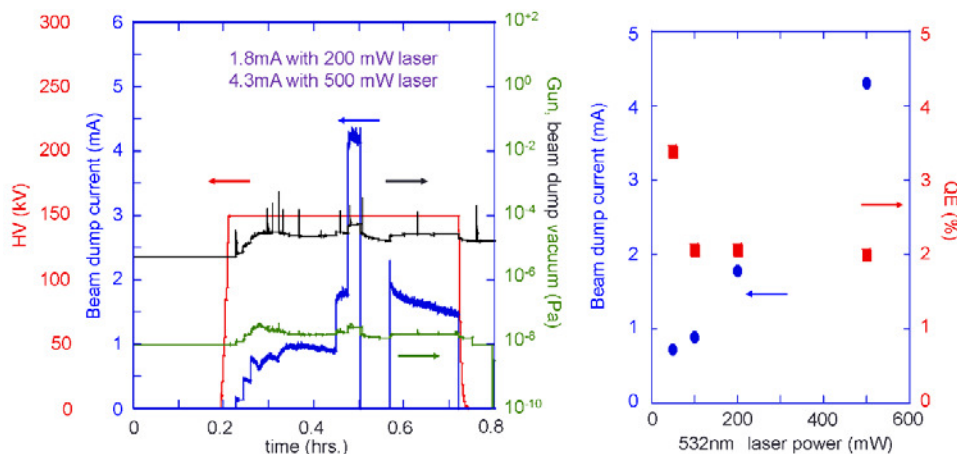
Figure 5:   The left figure shows beam current (blue curve) measured at a beam dump, high voltage (red curve), gun vacuum (green curve) and beam dump vacuum (black curve). The right figure shows beam dump current (blue circles) and QE (red squares) as a function of laser power at 532nm. The laser with maximum power of 3 W is used for this measurement.

test result. Maximum beam current of 4.3 mA was generated with 500 mW laser power. The QE was 2 %.

We tried to decrease radiation level by adjusting beam transport. When we gradually increased the beam current, a vacuum incident suddenly happened. The gun vacuum level went up to 1 Pa from 10^{-8} Pa. We found a small hole on a bellow placed just downstream the gun. We also noticed that only 3.6 mA beam was transported to the beam dump for 500 mW laser, while it was 4.3 mA before adjustment of beam transport. Presumably certain amount of beam hit the bellow and made a leak hole.

SUMMARY

We have developed a DC gun test stand at QST to generate high current beam from the gun. The test stand consists of an alkali antimonide photocathode preparation chamber, a DC gun, and a beam line with a water cooled beam dump. We successfully fabricated a Cs_3Sb photocathode with quantum efficiency of 5.8 % at 532 nm wavelength and generated 150 keV beam with current up to 4.3 mA with 500 mW laser at 532 nm wavelength. Unfortunately, we encountered a vacuum incident during beam transport of high current beam. We will fix the vacuum problem and restart the gun development. Though the photocathode was exposed to air of 1 Pa pressure, we will fabricate the Cs_3Sb with the same wafer to check reproducibility.

ACKNOWLEDGMENTS

REFERENCES

[1] N. Nakamura et al., "S2E Simulation of an ERL-Based High-Power EUV-FEL Source for Lithography", in Proc. of IPAC2017, p. 894-897, MOPVA020, Copenhagen, Denmark, 2017.

[2] J. Gardelle et al., Phys. Rev. STAB 12, (2012) 110701.

[3] N. Nishimori et al., "Development of a Multialkali Photocathode Preparation System", in Proc. of ERL2015, p.100-102, THPTHL073, Stony Brook, NY, 2015.

[4] L. Cultera et al., Appl. Phys. Lett. 103 (2013) 103504.

[5] Luca Cultera, "Fabrication, characterization, and use of alkali antimonides in a dc gun", Photocathode Physics for Photoinjectors 2012, Ithaka, NY, 2012.

[6] A. H. Sommer, "Photoemissive Materials", John Wiley & Sons, Inc. New York (1968).

[7] R. Nagai et al., "Development of a 250-kV Photo-cathode Electron Gun for the ERL Light Sources at JAEA", in Proc. of PAC2009, p. 545-547, Vancouver, BC, Canada, 2009.

[8] R. Nagai et al., Rev. Sci. Instrum. 83 (2012) 123303.

NOVOSIBIRSK ERL FACILITY*

N. A. Vinokurov[†1], V.M. Borin[1], I. V. Davidyuk[1], V.I. Dorokhov[1], O. I. Deichuly, E. N. Dementyev,
B. A. Dovzhenko, Ya. V. Getmanov[1], Ya. I. Gorbachev, B. A. Knyazev[1], E. I. Kolobanov,
A. A. Kondakov, V. R. Kozak, E. V. Kozyrev[1], S. A. Krutikhin, V. V. Kubarev[1],
G. N. Kulipanov[2], E. A. Kuper, I. V. Kuptsov, G. Ya. Kurkin, A.A. Murasev,
L. E. Medvedev, O.I. Meshkov, S. V. Motygin, V. K. Ovchar, V. N. Osipov, V. M. Petrov,
A. M. Pilan, V. M. Popik, V. V. Repkov, T. V. Salikova, M. A. Scheglov, I .K. Sedlyarov,
S. S. Serednyakov[1], O. A. Shevchenko, A. N. Skrinsky, S. V. Tararyshkin, A. G. Tribendis[2],
V. G. Tcheskidov, P. D. Vobly, V. N. Volkov. Budker INP SB RAS, Novosibirsk, Russia
[1]also at Novosibirsk State University, Novosibirsk, Russia
[2]also at Novosibirsk State Technical University, Novosibirsk, Russia

Abstract

The first project of the four turn ERL for Novosibirsk FELs (NovoFEL) was proposed at FEL'90 Conference. Later the project was modified, but the base lines kept: a four turn normal conductance linac with energy recovery, low RF cavities (180 MHz), grid controlled DC gun (Q~1nC, τ=1 nsec, f_{rep} = 10 kHz–50 MHz). The ERL can operate in the three modes, providing an electron beam for the three different FELs (from 300 μm up to 5 μm). Construction and commissioning four-track ERL was divided on three stage: the first stage NovoFEL working in spectral range (90–240) μm, based on one track energy recovery linac (ERL) with energy 12 MeV and current 30 mA, was commissioned in 2003. The second stage of NovoFEL working in spectral range (35–80) μm, based on two track energy recovery linac with energy 22 MeV and current 7 mA, was commissioned in 2009. The third stage of NovoFEL working in spectral range (8–15) μm, based on four track energy recovery linac with energy 42 MeV and current 5 mA was commissioned in 2015.

INTRODUCTION - ERL ACTIVITY IN BUDKER INP

The Energy Recovery Linac (ERL) concept for the free electron laser (FEL) was proposed at Budker INP by N. Vinokurov and A. Skrinsky in 1978 [1]. The first project of the four-turn race-track microtron-recuperator for the FEL was proposed at the FEL'90 Conference (1990) [2].

Later the project was modified, but the base line kept: a four-turn normal conductance linac with energy recovery; normal conducting RF cavities (180 MHz); a grid-controlled DC gun with bunch charge about 1nC, duration 1 nsec, and bunch frequency 10kHz–50 MHz.

Advantages of the low frequency (180 MHz) RF system: high threshold currents for instabilities; operation with long electron bunches (for narrow FEL linewidth); large longitudinal acceptance (good for operation with large energy spread of used beam); relaxed tolerances for orbit lengths and longitudinal dispersion.

Today, the ERL can operate in three modes, providing an electron beam for the three different FELs, from 300 μm up to 5 μm [3,4].

The first stage of the Novosibirsk FEL (NovoFEL) works in the spectral range (90–240) μm, based on a one track Energy Recovery Linac (ERL) with energy 12 MeV, was commissioned in 2003 [5]. It is the most powerful radiation source in terahertz region.

The second stage works in infrared spectral range (35–80) μm, based on two track Energy Recovery Linac with energy 22 MeV, was commissioned in 2009 [6].

The third stage working in spectral range (8–15) μm, based on four track energy recovery linac with energy 42 MeV, was commissioned in 2015 [7].

From 1997 the using an ERL for a fully spatially coherent X-ray source has been discussed at BINP [8]. The feasibility study of the 5.6 GeV machine with two split super-conducting accelerating sections (similar to CEBAF accelerator [9]) was presented at ERL-11 conference in 2011 [10]. The same accelerating scheme was supposed for the project of compact 13.5 nm FEL based on 800 MeV ERL facility for extreme ultraviolet lithography in 2010 [11, 12].

NOVOFEL ACCELERATOR

The NovoFEL facility includes three FELs. All the FELs use the electron beam of the same electron accelerator, a multi-turn energy recovery linac. A simplified scheme of the four-turn ERL is shown in Fig. 1. Starting from low-energy injector 1, electrons pass four times through accelerating radio frequency (RF) structure 2. After that, they lose part of their energy in FEL undulator 4. The used electron beam is decelerated in the same RF structure, and the low-energy electrons are absorbed in beam dump 5.
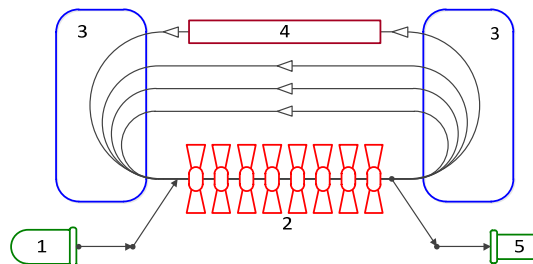
Figure 1: Simplified multi-turn ERL scheme:
1 – injector, 2 – linac, 3 – bending magnets,
4 – undulator, 5 – dump.
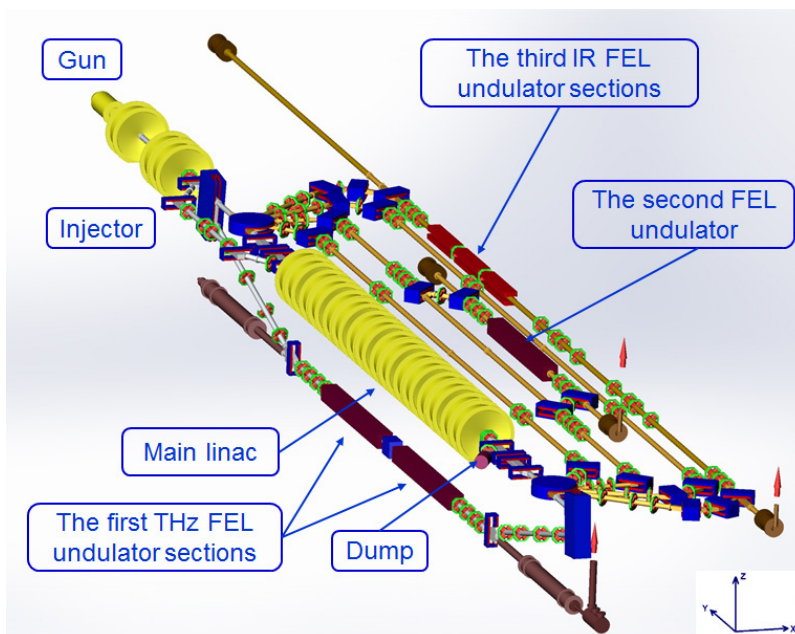
Figure 2: The Novosibirsk ERL with three FELs (top view).

The electron source is a 300 kV electrostatic gun with a grid cathode. It provides 1 ns bunches with a charge of up to 1.5 nC, a normalized emittance of about 20 µm, and a repetition rate of zero to 22.5 MHz. After the 180.4 MHz bunching cavity the bunches are compressed in the drift space (about 3 m length), accelerated in the two 180.4 MHz accelerating cavities up to 2 MeV, and injected by the injection beamline and the chicane into the main accelerating structure of the ERL (see Fig. 2). Parameters of the accelerator is presented in Table 1.

Table 1. NovoFEL accelerator parameters

Modes:	1st	2d	3d
RF frequency, MHz	180.4		
Gun working freq., MHz	5.6-22.4	7.52	3.76
Energy, MeV	10-14	22	42
Average current, mA	30	7.5	3
Recuperation efficiency, %	>95		
Wavelength, µm	90-240	40-80	8-11
Electron efficiency, %	0.6	0.3	0.2

The Magnetic Structure

The Novosibirsk ERL has three modes, one mode for operation of each of the three FELs. The first FEL is installed under the accelerating (RF) structure (see Figs. 2 and 3). Therefore, after the first passage through the RF structure, the electron beam with energy of 12 MeV is turned by 180 degrees in the vertical plane. After the use in the FEL, the beam returns to the RF structure in the decelerating phase. In this mode, the ERL operates as a single-orbit installation.

For operation with the second and third FELs, two round magnets (a spreader and a recombiner) are switched on. They bend the beam in the horizontal plane, as shown in Fig. 2. After four passes through the RF accelerating

structure, the electron beam gets in the undulator of the third FEL. The energy of electrons in the third FEL is about 42 MeV. The used beam is decelerated four times and goes to the beam dump.

If the four magnets on the second track (see Fig. 2) are switched on, the beam with energy of 22 MeV passes through the second FEL. After that, it enters the accelerating structure in the decelerating phase due to the choice of the length of the path through the second FEL. Therefore, after two decelerations the used beam is absorbed in the beam dump. A photo of the accelerator hall with the accelerating RF cavities and the FELs is shown in Fig. 3.

It is worth noting that all the 180 degree bends are achromatic (even second-order achromatic on the first and second horizontal tracks,) but non-isochronous. It enables beam longitudinal "gymnastics" to increase the peak current in the FELs and to optimize deceleration of the used beam.
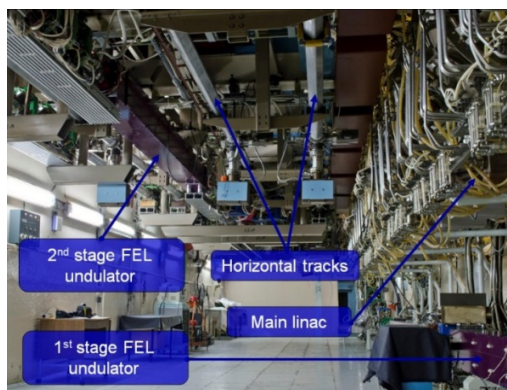
Figure 3: Accelerator hall

The RF System

The main accelerating structure consists of 16 normal-conducting RF cavities, connected by two waveguides. The operation frequency is 180.4 MHz. Such a low frequency allows operation with long bunches and high currents. Even and odd cavities are united into two groups. Each group of cavities is fed from its own RF generator. Project power of each RF generator is 600 kW.

In the RF system, bi-metal copper clad stainless steel cavities are used [13]. The electrical parameters of cavities are given in Table 2.

Table 2. NovoFEL RF cavity parameters

Operating frequency, MHz	180.4
Tuning range, kHz	320
Characteristic impedance, Ohm	133.5
Quality factor	40000
Shunt impedance, MOhm	5.3
Operating gap voltage, kV	950
Power dissipation, kW	85
Transit time factor	0.9

Each RF generator (Fig. 4) consists of four stages. First and second stages of the amplifier are made of tetrodes GU-92A. Third stage is based on GU-101A tetrode, fourth stage is made of modules based on TH-781 tetrodes.

The modular design of the RF generator [14] essentially simplifies the power addition from several tubes, and simplifies manufacturing and adjustment of the whole generator. The 600 kW output stage is assembled with four modules. The single module is used as a third stage of the generator.

Figure 4. NovoFEL generators hall

The feeder system (Fig. 5) is made of rectangular waveguides and coaxial lines. Also it provides power distributing between the cavities in the groups.

The control system adjusts amplitude and phase of the RF voltage of the accelerating cavities, tunes the cavities, and removes RF excitation from the generator in emergency conditions.

Each channel was tested at 7500 kV on the gaps of 8 cavities. The RF power was 630 kW per channel. The efficiency factor of the output stage is 57 %.

Now, the accelerating RF system operates at 13600 kV on 16 cavities. Total power of generators is 1100kW.

Figure 5. NovoFEL feeder system

FELS

The first FEL has been in operation since 2003 [5]. It provides a narrow-band (less than 1%) terahertz radiation in the wavelength range of 80–240 μm at an average power of up to 0.5 kW and a peak power of up to 1 MW (100 ps pulses at a repetition rate of 5.6 MHz). About 30 user research projects in different fields of science were carried out at the facility in recent years; see e.g. [15 – 20].

The radiation of all the three FELs is directed to the same nitrogen-filled beamline to the user stations. The radiation combiner is shown in Fig. 6.

Figure 6. Optical beamline for FELs. Radiation of all FELs is delivered to the same user stations. Switching between FELs is done using retractable mirrors

The second FEL generates a narrow-band (less than 1%) far infrared radiation in the wavelength range of 40–80 μm at an average power of up to 0.5 kW and a peak power of up to 1 MW (50 ps pulses at a repetition rate of 7.5 MHz).
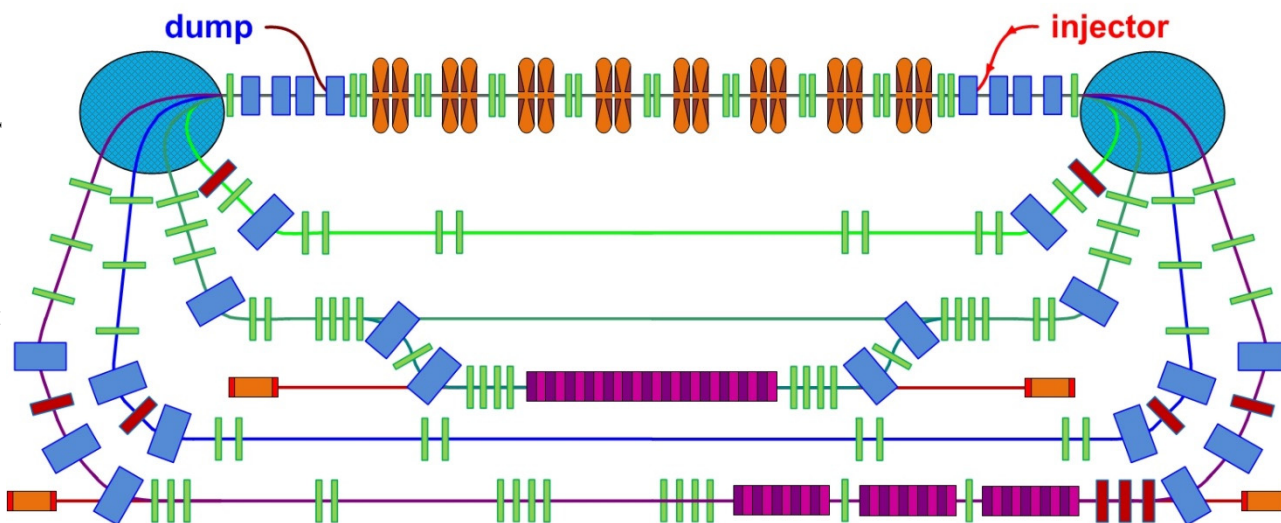
Figure 7. The second and third stages ERL with FEL undulators and optical cavities

The undulator of the third FEL is installed on the fourth track, as shown in Fig. 7 and Fig. 8. The whole undulator is composed of three 28-period sections. Each of them is a permanent magnet undulator with a period of 6 cm and a variable gap. Now the section in the middle is used for phasing of the two other sections. The wavelength range of this FEL is 5–20 μm.
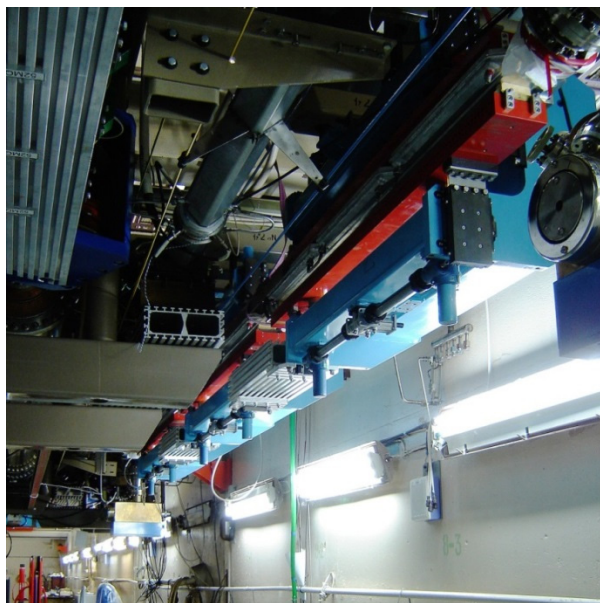
Figure 8. The third FEL undulators

Table 3. NovoFEL radiation parameters

Modes:	1st	2d	3d
Wavelength, μm	90–240	40–80	5–20
Max. radiation power, kW	0.5	0.5	0.1
Max. peak power, MW	1	2	10
Min. pulse duration, ps	70	20-50	10-20
Length between pulses, ns	180	133	267
Rel. linewidth (FWHM), %	0.3–1	0.2–1	0.1–1

FUTURE PLANS

In the future it is planned to improve the x-ray and neutron radiation shielding for regular users operation on high energy mode, install the new variable-period undulator, new injection beamline for RF gun and optical diagnostics of electron beam parameters. Moreover, it is expected to implement an electron out-coupling scheme on the four-turn ERL.

The New RF Gun

The current of the Novosibirsk ERL is now limited by the electron gun. A new RF gun [21] (see Fig. 10) was built and tested. It operates at a frequency of 90 MHz. An average beam current of more than 100 mA was achieved recently [22]. The injection beamline (see Fig. 9) for the RF gun will be manufactured this year.
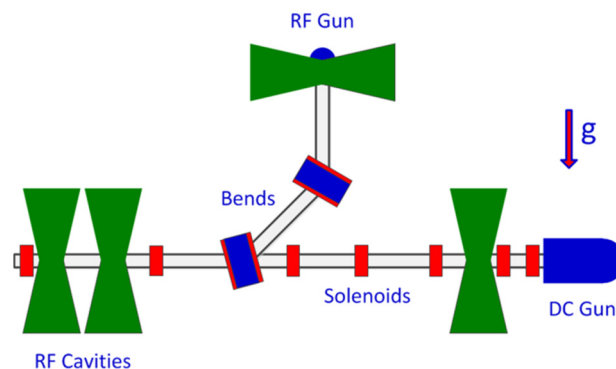
Figure 9. Scheme of NovoFEL injector with new gun

Table 4. Measured RF gun parameters

Energy, keV	100–320
Pulse duration(FWHM), ns	≤ 0.6
Bunch charge, nQ	0.3–1,5
Repetition rate, MHz	0.01–90
Average current, mA	102 max

MOIDCC002

Figure 10: New electron RF gun for Novosibirsk ERL

Variable-Period Undulator

The new variable-period undulator [23] (see Fig. 11) is being prepared to replace the old electromagnetic one of the second FEL [24]. It will allow us to expand significantly the wavelength tuning range.

Figure 11. Variable Period Undulator λ_u=4.8–9.6 cm

FEL Outcoupling

The optical cavity of this FEL is about 40 m long. It is composed of two copper mirrors. The radiation is out-coupled through the holes in the mirror center. We also plan to implement an electron out-coupling scheme here [25] (see Fig. 12). In this scheme, the beam is bunched in the first undulator and then the achromatic bend slightly deflects it in the transverse direction, so that its radiation in the second undulator goes off the axis and passes by the front mirror. It should be noted that this scheme is advantageous only with high power radiation. Typically, the users do not need much power and the out-coupling through the holes is much simpler.

Optical Diagnostics of Electron Beam Parameters

The beam energy at the last track of the ERL is 42 MeV. As a result, a significant part of synchrotron radiation from bending magnets is in the visible range. The transverse beam dimensions were measured with the optical diagnostics before and after the undulator applied for generation of mid-infrared coherent radiation (see Fig. 13 and Fig. 14). The obtained data is used to calculate the beam energy spread and emittance. The longitudinal beam dynamics was studied with electro optical dissector. [26]
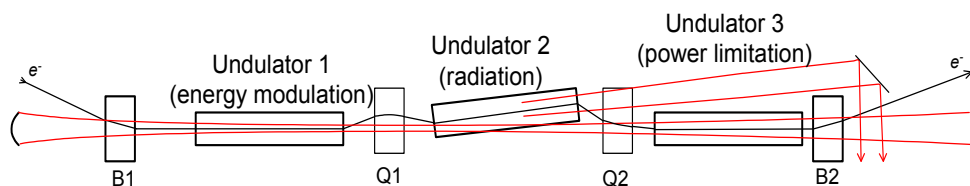
Figure 12: Electron out-coupling scheme
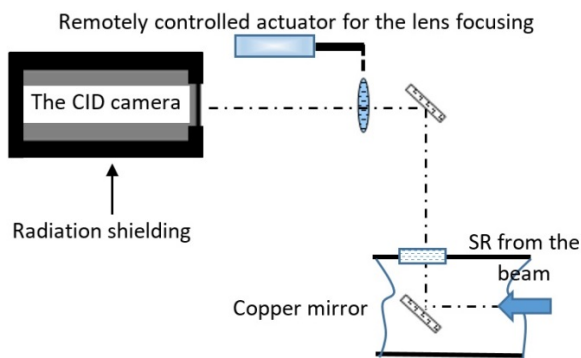
Figure 13. Layout of the diagnostics for acquisition of the transverse profile of the beam
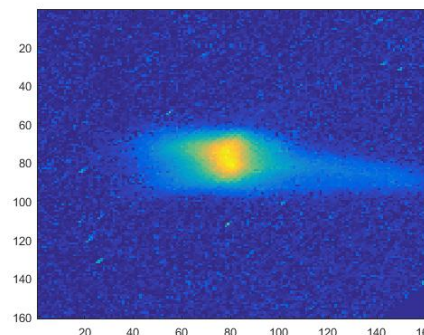
Figure 14. An example of the beam transverse distribution

ACKNOWLEDGMENTS

REFERENCES

[1] N. A. Vinokurov *et al.* Preprint BINP, (1978) 78-88*; Proc. of the 6th Soviet Union Accelerator Conference*, VII (1978) 233-236.

[2] N.G Gavrilov *et al.*, "Project of CW Racetrack Microtron-Recuperator for Free Electron Lasers" *Nucl. Instr. and Meth.* A304 (1991) 228-229.

[3] G. N. Kulipanov *et al.*, "Novosibirsk Free Electron Laser - Facility Description and Recent Experiments", *IEEE Trans. on Terahertz Science and Technology*, 5(5) (2015) 798–809.

[4] O. A. Shevchenko *et al.*, "The Novosibirsk Free Electron Laser – unique source of terahertz and infrared coherent radiation", *Phys. Procedia*, 84 (2016) 13-18.

[5] E. Antokhin *et al.*, "First lasing at the high-power free electron laser at Siberian center for photochemistry research", *Nucl. Instr. and Meth.* A 528(1) (2004) 15–18.

[6] E Vinokurov N.A. *et al.*, Proc. of FEL2009 (2009) 447-451.

[7] O.A. Shevchenko *et al.*, Proc. of FEL2015 (2015) 1-4.

[8] G.N. Kulipanov *et al.*, "Synchrotron light sources and recent development of accelerator technology", *J. of Synchrotron Radiation*, 5 (3) (1998) 176; A.N. Skrinsky *et al.*, "MARS – a project of diffraction limited fourth generation X-ray source based on super microtron", *Nucl. instrum. and meth. in physics res.*, A467-468 (2001) 16-20.

[9] D. Douglas, "A Generic Energy-Recovering Bisected Asymmetric Linac (GERBAL)", *ICFA BD-Nl,* 26 (2001) 40-45.

[10] Y.V. Getmanov *et al.*, "Full spatial coherent multiturn ERL x-ray source (MARS) based on two Linacs", *Bristol: IOP Publishing – Journal of Physics: Conference Series*, (2013) 4.

[11] Y. Sokol *et al.*, "Compact 13.5-nm free electron laser for extreme ultraviolet lithography", *PRST AB*, 14(040702) (2011) 7.

[12] Y.V. Getmanov *et al.*, "Beam Stability Investigation for a Free Electron Lithographic Laser Based on an Energy-Recovery Linac", *Physics of Particles and Nuclei Letters*, 13 (7) (2016) 835–838.

[13] N.Gavrilov *et al.*, "RF Cavity for the Novosibirsk Race-Track Microtron-Recuperator", Budker INP preprint, (1994) 94-92

[14] V.S.Arbusov, *et al.*, "Powerful RF generator of a modular design for stores and accelerators", *XVI meeting on accelerators of the charged particles*, (1998).

[15] B. A. Knyazev *et al.*, "Generation of Terahertz Surface Plasmon Polaritons Using Nondiffractive Bessel Beams with Orbital Angular Momentum", *Phys. Rev. Lett.*, 115(16) (2015) 163901.

[16] Yu. Yu. Choporova *et al.*, "Classical Holography in the Terahertz Range: Recording and Reconstruction Techniques", *IEEE Trans. on Terahertz Science and Technology*, 5(5) (2015) 836–844.

[17] M. S. Komlenok *et al.*, "Fabrication of a multilevel THz Fresnel lens by femtosecond laser ablation", *Quantum Electronics*, 45(10) (2015) 933–936.

[18] A. N. Agafonov *et al.*, "Control of transverse mode spectrum of Novosibirsk free electron laser radiation", *Applied Optics*, 54(12) (2015) 3635.

[19] E. N. Chesnokov *et al.* "Non-Faraday rotation of the free induction decay in gaseous NO", *Chem. Phys. Lett.*, 636 (2015) 203–207.

[20] V. V. Gerasimov *et al.*, "Experimental investigations into capability of terahertz surface plasmons to bridge macroscopic air gaps", *Optics Express*, 23(26) (2015) 33448.

[21] V. Volkov *et al.*, "Thermocathode radio-frequency gun for the Budker Institute of Nuclear Physics free-electron laser", *Physics of Particles and Nuclei Letters* 13 (7) 796 - 799 (2016).

[22] V. Volkov *et al.*, "New RF gun for Novosibirsk ERL FEL", *Phys. Procedia*, 84 (2016) 86-89.

[23] N. A. Vinokurov *et al.*, "Variable-period permanent magnet undulators", *Phys. Rev. ST Accel. Beams*, 14(4) (2011) 040701.

[24] I. Davidyuk *et al.*, "Modeling and designing of variable-period and variable-pole-number undulator", *Phys. Rev. Accel. Beams* 19 (2016) 020701.

[25] A. Matveenko *et al.*, "Electron outcoupling scheme for the Novosibirsk FEL", *Nucl. Instr. and Meth.* A 603 (2009) 38 – 41.

[26] V.M. Borin *et al.*, "An experimental study of beam dynamics in the ERL-based Novosibirsk free electron laser", Proc. of IPAC2017, (2017) 3781-3783.

ERL MODE OF S-DALINAC: DESIGN AND STATUS*

M. Arnold[†], C. Burandt, J. Pforr, N. Pietralla, TU Darmstadt, Germany
C. Eschelbach, M. Lösler, Frankfurt University of Applied Sciences, Germany
T. Kürzeder, Helmholtz Institut Mainz, Germany

Abstract

Recently, the S-DALINAC was extended by an additional recirculation beam line to a thrice-recirculating linear accelerator. This upgrade enables an increase of the maximum achievable energy close to its design value of 130 MeV as well as an operation as an ERL. The new beam line features a path-length adjustment system which is capable of changing the phase of the beam by a full RF phase and, thus, allowing to shift the timing of the electron bunches to the decelerating phase. The project comprises different aspects concerning the design (magnets, beam dynamics, lattice, etc.) and the construction work including the alignment done at the accelerator. This contribution presents a rough overview on the design, installation and status.

INTRODUCTION

The S-DALINAC is a superconducting electron accelerator of TU Darmstadt. It was operated from its first commissioning as a recirculating LINAC in 1991 [1] until autumn of 2015 in a twice-recirculating set-up. The decision was made to add an additional recirculation beam line to increase the final beam energy and to enable an ERL operation. In 2015/2016 this major upgrade of the S-DALINAC was performed. The new beam line was installed in between the two existing recirculation beam lines. An upgrade of the final beam energy was necessary as in the past the final design energy of 130 MeV could not be reached due to a lower quality factor of the superconducting (sc) cavities [2] than originally anticipated and, thus, a higher dissipated power to the helium bath. Adding a main LINAC passage by installing an additional recirculation beam line allows the operation of the sc cavities on a decreased gradient while keeping the overall design beam energy constant. In this operation the dissipated power to the helium bath is adapted to the cooling power of the cryo plant. Figure 1 shows the floor plan of the thrice-recirculating S-DALINAC. In case of a thrice-recirculating operation an energy gain of up to 7.6 MeV for the injector LINAC and up to 30.4 MeV for the main LINAC are used. A maximum beam current of 20 μA can be accelerated in the recirculating operation.

ERL MODE

The upgrade of the S-DALINAC features an Energy-Recovery LINAC (ERL) mode in its new beam line. The path-length adjustment system of this newly installed section is capable of an adjustment range of 360° of the RF
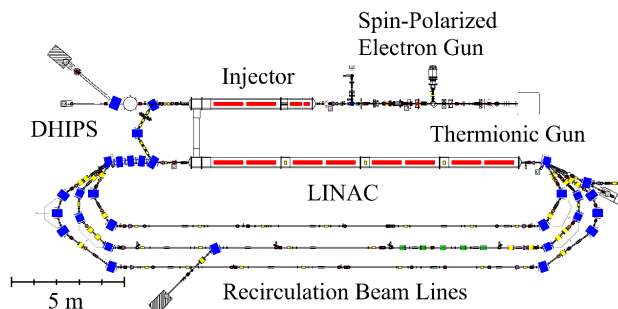
Figure 1: Floor plan of the S-DALINAC with three recirculations in the final set-up.

phase. Thus also a phase shift of 180° is possible so that the beam re-enters the main LINAC on the decelerating phase. Figure 2 shows the area of the first arcs with one out of two path-length adjustment systems of the new beam line, the separation dipole magnet as well as the dump for the decelerated beam. The beam, coming from the main accelerator, can directly be guided into the second recirculation. In this beam line the phase shift of 180° is conducted so that the beam is dumped at injection energy after being decelerated in the main LINAC (once-recirculating ERL mode, see Fig. 3). Alternatively, the beam can be deflected into the first recirculation followed by an additional acceleration in the main LINAC. During the passage through the second recirculation beam line the necessary phase shift is performed so that the beam then passes a second time through the first recirculation. After a second deceleration the beam is finally dumped at injection energy (twice-recirculating ERL mode, see Fig. 4). The purpose of the ERL mode of S-DALINAC is to serve as a test bed for principle investigations concerning the RF controlling [3] or the beam dynamics (e.g. the effect of (transversal) beam break-up (BBU) [4]).

DESIGN OF A THIRD RECIRCULATION INCLUDING ERL MODE

Figure 5 shows a view into the accelerator hall after the installation of the new beam line was finished. Long time in advance, before this installation could start, a complex design and detailed planning of this modification was done [5, 6]. Not only the design aspects considered in the following sections have been taken into account but also the design of other magnetic elements or more general aspects like the vacuum system.
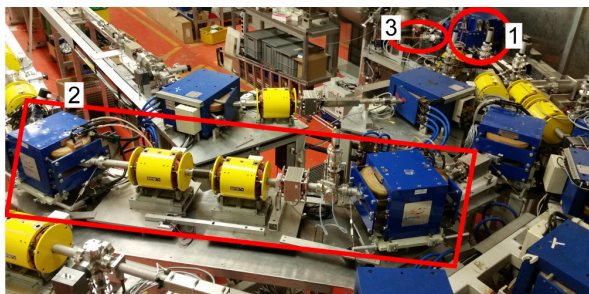
Figure 2: This photograph shows the first arc section of the S-DALINAC. The beams are bend by the separation dipole (1). One of two path-length adjustment systems of the new beam line is shown (2). They are capable to shift the phase of the beam by 180° for an ERL operation. The decelerated beam is then stopped at injection energy in the ERL beam dump (3).
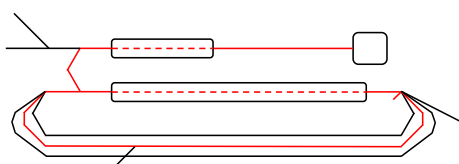
Figure 3: Scheme for once-recirculation ERL operation.
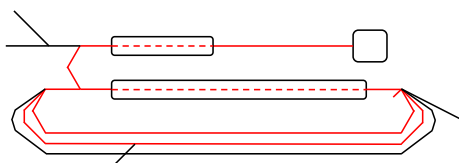
Figure 4: Scheme for twice-recirculation ERL operation.
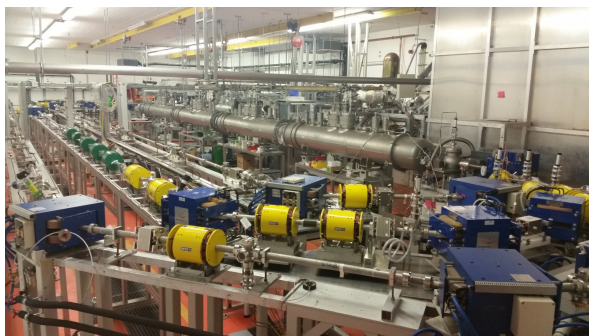
Figure 5: View into the accelerator hall with its three recirculations.

Separation Dipole Magnet

The separation dipole magnet as well as its mirrored version (recombination dipole magnet) are the most complex dipole magnets used at the S-DALINAC. Beams of up to five different energies are bent into their corresponding beam line. The new version of this magnet had to fit to the existing beam line sections on very limited space and demanding conditions. There has been a long list of requirements on this magnet concerning a variety of aspects. The most im-

portant in the context of its design will be mentioned. The properties of the magnetic field are defined in the so called good field region (GFR). The GFR is described by a circle with a radius of 5 mm which follows each orbit of every beam. The deflecting properties of the magnet have to be fulfilled to guarantee a perfect bending of all beams. For an optimal result of the beam dynamics simulations as well as of the beam operations, the homogeneity of the magnetic field (transversal, longitudinal) and the multipole components (without dipole part) have to stay below/are equal to $1 \cdot 10^{-3}$. In addition, a fixed energy gain ratio of injector to main LINAC of one to four has to be considered for the different beams. This ratio is a basis for the layout of the whole machine and had to be taken into account for the upgrade. Due to the change in energies and addition of a new beam line, all beam lines except for one had to be modified in position to fit new needs. During the demanding design the mirror plates of the dipole magnet have been the key elements for a best possible result. The magnetic field of 0.65 T is reached for the maximum electron energy. Figure 6 shows a photograph of the final magnet.
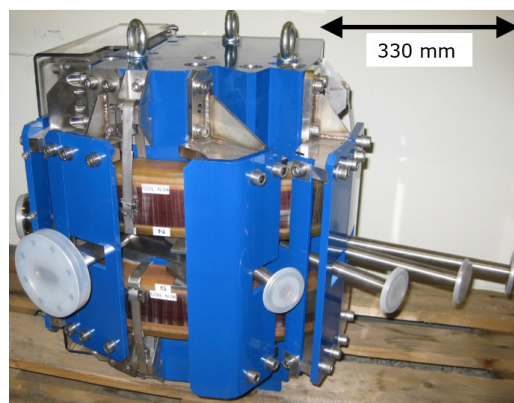
Figure 6: The new separation dipole magnet before its installation into the beam line. The four flanges for the three recirculation beam lines and the high-energy extraction beam line are visible to the right. The flange to the left leads to the ERL beam dump.

Beam Dynamics

One major pillar of the whole design was the simulation of the beam dynamics in different lattice sections for different operation schemes of the S-DALINAC. In this paper some exemplary simulations will be shown.

Normal Mode In the normal operation scheme of S-DALINAC, concerning the recirculation beam lines, a once- or thrice-recirculating setting is feasible. Depending on the mode, the ratio of energy gain from injector to main LINAC changes from one to four (thrice-recirculating) to one to eight (once-recirculating). Each lattice section was simulated separately with *xbeam* [7] and further simulations (e.g. start-to-end) have been conducted with *elegant* [8]. For recirculating operation modes it is possible to use an

MOIDCC006

isochronous or a non-isochronous setting of the recirculation beam lines in combination with an on-crest and off-crest acceleration, respectively. This special technique enables an increase of the energy resolution of the electron beam [9]. The necessary scaling of the quadrupole magnets in the arc sections have been calculated. Figure 7 shows the one-sigma envelope of a non-isochronous setting of the second recirculation as an example.
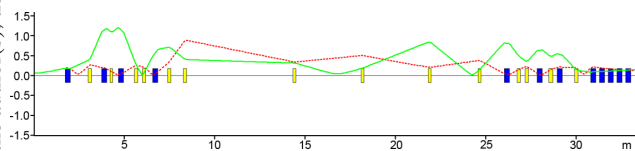
Figure 7: One-sigma envelope of the second recirculation. The dipole magnets are marked as blue boxes, the quadrupole magnets as yellow symbols. The envelope in x- (red) and y-direction (green) is shown in mm along the beam line (simulation done with *xbeam* [7]).

ERL Mode   For ERL operation two schemes have to be taken into account: A once- and a twice-recirculating ERL mode (see Fig. 3 and 4). While the simulations for the twice-recirculating case are currently under investigation, first results for the once-recirculating setting have been achieved. Figure 8 shows the envelope of the once-recirculating ERL mode. The simulation, calculated with *elegant* [8], starts behind the injector LINAC. Then the beam is accelerated, guided through the second recirculation before it is decelerated and stopped in the beam dump. The size of the envelope is comparable to the results from Fig. 7. Small deviations are also caused by the change of the simulation tool.
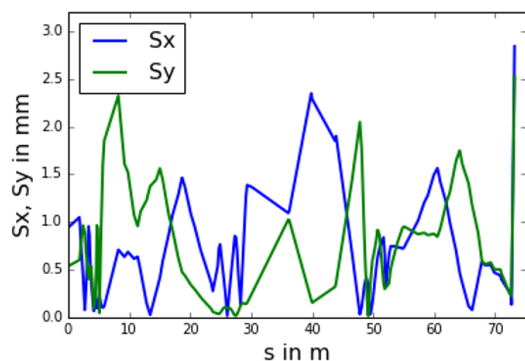
Figure 8: One-sigma envelope of the once-recirculating ERL mode is presented. The scheme shows the position along the orbit (simulation done with *elegant* [8]).

Increasing BBU Limit   The cavities of S-DALINAC have not been optimized for a suppression of higher order modes (HOMs) and they do not have any HOM damping. So only several µA are sufficient for the occurrence of BBU at

the S-DALINAC [4]. Several possibilities exist to increase the BBU threshold current. One theory uses the complete exchange of both transversal phase spaces [10]. This exchange is conducted by five skew quadrupole magnets which have been installed in the new recirculation beam line. Figure 9 and 10 show for a once-recirculating ERL operation the exchange of the transversal phase spaces: The main diagonal matrix elements are transformed to zero while the outer diagonal elements are unequal zero after the exchange.
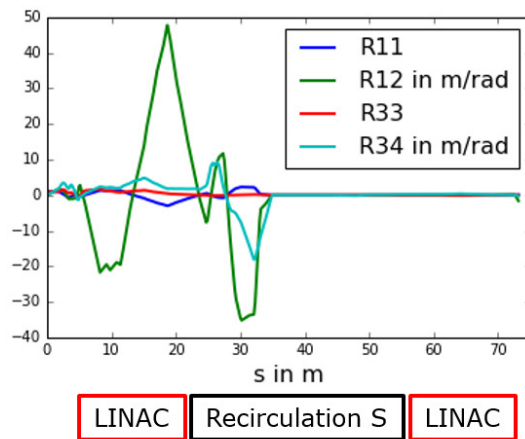
Figure 9: The exchange of the transversal phase spaces transforms the main diagonal matrix elements to zero (simulation done with *elegant* [8]).
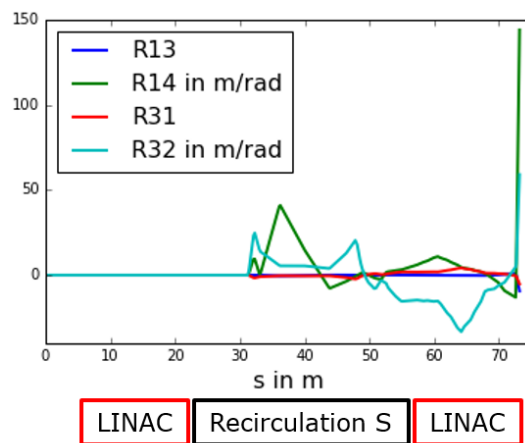
Figure 10: The exchange of the transversal phase spaces transforms the outer diagonal matrix elements to non-zero values (simulation done with *elegant* [8]).

INSTALLATION

After the preparation of all elements the installation was conducted. In the beginning of this phase a major part of all recirculation beam lines had to be disassembled (new position/lattice design of recirculation loop). Installing all beam lines very cautiously was scheduled afterwards followed by an alignment of the whole lattice.

Alignment

Aligning all magnetic elements ensures a perfect transfer from the beam dynamics simulations to the real machine. The alignment was done with a lasertracker AT401 from Leica [11, 12]. In the beginning a coordinate system was defined to work with. There have been several phases of alignment to guarantee an optimized result. Finally the precision shown in Table 1 as well as the accuracy of the tilt around the axes (see Table 2) have been achieved.

Table 1: Resulting positioning precision for the different magnet types for the horizontal (x), vertical (y) and longitudinal (z) direction.

Magnet Type	x in mm	y in mm	z in mm
Dipole	0.27 ± 0.12	0.20 ± 0.14	0.17 ± 0.13
Quadrupole 1	0.27 ± 0.11	0.19 ± 0.12	0.23 ± 0.18
Quadrupole 2	0.32 ± 0.16	0.21 ± 0.17	0.28 ± 0.23
Sextupole	0.33 ± 0.18	0.29 ± 0.22	0.15 ± 0.11[1]

Table 2: Resulting precision in terms of tilt around the horizontal (x) and longitudinal (z) axis for the different magnet types.

Magnet Type	Tilt in ° around x and z
Dipole	0.020 ± 0.019
Quadrupole 1 and 2	0.057 ± 0.051
Sextupole	0.104 ± 0.084

Path-Length Adjustment System

Figure 11 shows the position of all path-length adjustment systems in the floor plan of the S-DALINAC. These systems are used to optimize the phase of the beam in each recirculation for the re-entry into the main LINAC. Also a change from a normal operation to an ERL operation is possible, if the stroke is big enough (more than 180° is necessary). The stroke of all systems was measured with the lasertracker and is summarized in Table 3. A full RF wavelength is equivalent to a distance of 100 mm. So only the second recirculation (sum of both systems amounts to 100.8 mm) is capable of an ERL setting.
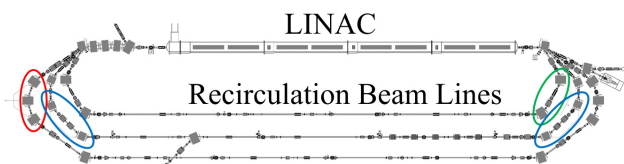
Figure 11: The path-length adjustment systems of the first (green), second (blue) and third (red) recirculation are marked in the floor plan of S-DALINAC.

Table 3: All strokes of the path-length adjustment systems have been measured with the lasertracker. The uncertainty amounts to < 0.2 mm.

System	Stroke in mm
First	33.8
Second 1	50.2
Second 2	50.6
Third	30.6

STATUS OF COMMISSIONING

The commissioning of the upgraded S-DALINAC started in December 2016. A first transport of the beam through the injector and main LINAC including the first passage of the new separation dipole magnet was achieved at the end of December before end-of-year shut-down. After some maintenance the beam was brought from the injector into the main LINAC and transported for the first time through the new recirculation beam line with a subsequent crossing of our main LINAC. The beam was than stopped at the beginning of the extraction (similar to once-recirculating ERL operation, see Fig. 3). At the moment the commissioning is continued.

CONCLUSION AND OUTLOOK

The superconducting Darmstadt linear accelerator (S-DALINAC) has been modified. The design and installation of an additional beam line including an ERL mode as well as all necessary modifications of the old layout was a complex and challenging task which is successfully completed. Some insights into the design concerning the most important dipole magnet - the separation dipole magnet - as well as some beam dynamics simulations and the final alignment have been presented. All path-length adjustment systems and the stroke, they are capable of, have been introduced. At the moment the modified S-DALINAC is under commissioning. First successes, as a transport of the beam trough the new beam line and a second passage through the main LINAC, have been achieved. The next steps will be the investigation of a once-recirculating ERL mode followed by a thrice-recirculating normal operation to prepare for first electron-scattering experiments after the current shut-down time.

REFERENCES

[1] A. Richter, "Operational experience at the S-DALINAC", in *Proc. EPAC'96*, Sitges Jun. 1996, pp. 100-114.

[2] R. Eichhorn et al., "Results from a 850 C Heat Treatment and Operational Findings from the 3 GHz SRF Cavities at the S-DALINAC", in *Proc. SRF 2007*, Beijing, China 2007, pp. 163-165.

---

[1] The accuracy of the method used is given as there have been no target positions to match.

[3] M. Steinhorst et al., "Challenges of a Stable ERL Operation Concerning the Digital RF Control System of the S-DALINAC", in *Proc. IPAC 2017*, Copenhagen, Denmark 2017, pp. 3951-3953.

[4] T. Kürzeder et al., "Measurements of the Beam Break-Up Threshold Current at the Recirculating Electron Accelerator S-DALINAC", in *Proc. LINAC 2016*, East Lansing, MI, USA 2017, pp. 751-753.

[5] M. Arnold et al., "Final Design and Status of the Third Recirculation for the S-DALINAC", in *Proc. IPAC 2016*, Busan, Korea 2016, pp. 1717-1719.

[6] M. Arnold et al., "Construction of a Third Recirculation for the S-DALINAC", in *Proc. LINAC 2016*, East Lansing, MI, USA 2017, pp. 168-170.

[7] Software: xbeam 2.1 by IKP TU Darmstadt

[8] M. Borland, "elegant: A Flexible SDDS-Compliant Code for Accelerator Simulation," Advanced Photon Source LS-287, September 2000.

[9] F. Hug et al., "Improving Energy Spread and Stability of a Recirculating Few-Turn LINAC", in *Proc. IPAC 2016*, Busan, Korea 2016, pp. 3222-3225.

[10] Y. Petenev et al., "Modeling ot the Beam Break Up Instability for bERLinPro", in *Proc. IPAC 2011*, San Sebastian, Spain, 2011 pp. 718-720.

[11] M. Lösler et al., "Hochpräzise Erfassung von Strahlführungselementen des Elektronenlinearbeschleunigers S-DALINAC", *zfv*, vol. 6/2015 140. Jg, pp. 346-356.

[12] C. Eschelbach et al., "Einsatz mobiler Lasermesstechnik bei der Erfassung von Strahlführungselementen eines Elektronenlinearbeschleunigers", *Allgemeine Vermessungs-Nachrichten AVN*, 2017, vol. 124(3), pp. 61-69.

MOIDCC006

LERF – NEW LIFE FOR THE JEFFERSON LABORATORY FEL[*]

C. Tennant†, S. Benson, J. Boyce, J. Coleman, D. Douglas, S. Frierson, J. Gubeli, C. Hernandez-Garcia, K. Jordan, C. Keith, R. Legg, M. McCaughan, M. Spata, T. Satogata, M. Tiefenback, S. Zhang, Thomas Jefferson National Accelerator Facility, Newport News, VA 23606, USA

J. Balewski, J. Bernauer, J. Bessuille, R. Corliss, R. Cowan, C. Epstein, P. Fisher, I. Friščić, D. Hasell, E. Ihloff, J. Kelsey, S. Lee, P. Moran, R. Milner, D. Palumbo, S. Steadman, C. Tschalär, C. Vidal, Y. Wang, Massachusetts Institute of Technology, Cambridge, Massachusetts, 02139, USA

T. Cao, B. Dongwi, P. Gueye, N. Kalantarians, M. Kohl, A. Liyanage, J. Nazeer, Hampton University, Hampton, Virginia, 23668, USA

R. Alarcon, D. Blyth, R. Dipert, L. Ice, G. Randall, B. Thorpe, Arizona State University, Phoenix, Arizona, 85004, USA

R. Cervantes, K. Dehmelt, A. Deshpande, N. Feege, Stony Brook University, Stony Brook, New York, 11794, USA

P. Evtushenko, HZDR, Dresden, Germany

M. Garçon, CEA Saclay, Gif-sur-Yvette, France

B. Surrow, Temple University, Philadelphia, Pennsylvania, 19122, USA

Abstract

In 2012 Jefferson Laboratory's energy recovery linac (ERL) driven Free Electron Laser successfully completed a transmission test in which high current CW beam (4.3 mA at 100 MeV) was transported through a 2 mm aperture for 7 hours with beam losses as low as 3 ppm. The purpose of the run was to mimic an internal gas target for DarkLight [1] – an experiment designed to search for a dark matter particle. The ERL was not run again until late 2015 for a brief re-commissioning in preparation for the next phase of DarkLight. In the intervening years, the FEL was rebranded as the Low Energy Recirculator Facility. In 2016 several weeks of operation were allocated to configure the machine for DarkLight with the purpose of exercising – for the first time – an internal gas target in an ERL. Despite a number of challenges, including the inability to energy recover without losses (precluding CW operation), beam was delivered to a target of thickness 10^{18} cm^{-2} which represents a three order of magnitude increase in thickness from previous internal target experiments. Details of the machine configuration and operational experience will be discussed.

BACKGROUND

After 15 years of consistent operation and upgrades Jefferson Laboratory's energy recovery linac (ERL) driven Free Electron Laser (FEL) ceased operation in 2012. Missing a steady funding for operations, the LERF has only been operational for a combined few weeks over the last five years. The common thread in all those run periods was the DarkLight experiment. This innovative experiment is searching for a dark matter particle by studying e⁻p scattering using a high power (1 MW) electron beam and a gaseous hydrogen internal target [2].

2012: APERTURE TEST

The DarkLight physics run requires continuously running a 1 MW beam into an internal target for 60 days. To address the technical challenges several different experiments were run at the LERF. One foundational question that needed to be answered is whether a high power, CW beam could be transmitted through an aperture consistent with that of an internal target with sufficiently low beam loss.

To mimic an internal target, apertures of (2, 4 and 6) mm diameter were drilled in a 127 mm long block of aluminum and the whole apparatus installed in the 3F region of the FEL (see Figs. 1 and 2). Though the target and detector package were ultimately located downstream in the 4F region, the 3F region was a natural choice for the initial test since it is well instrumented with BPMs, correctors and viewers, the beamline is well characterized (90° FODO cells) and it provides enough focusing to achieve the desired match with additional knobs available for halo control [3].
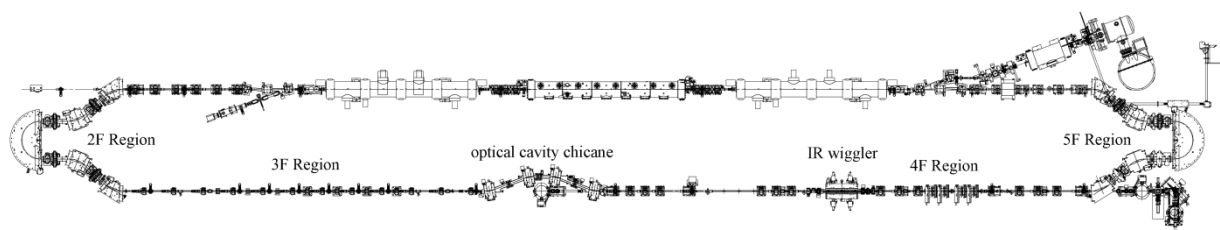
Figure 1: Schematic of the LERF (formerly FEL) without the UV bypass line.

Unlike running the machine as an FEL – which requires a short, high peak current bunch – DarkLight places a premium on long bunches with low energy spread so as to reduce dispersion errors and alleviate resistive wall heating. Establishing a longitudinal match to generate those kinds of bunches requires only changing the gang phase of one cryomodule and running the linac cross-phased. By switching the accelerating phase of the middle cryomodule (which has the same gradient as the two outboard cryomodules combined) to the falling side of the RF waveform the energy chirp is removed and nearly mono-energetic (~0.02% rms energy spread) at the exit (see Fig. 3).
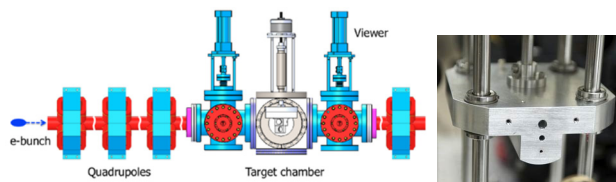
Figure 2: Schematic of the target chamber and diagnostics in the 3F region (left) and photo of the aperture block (right) showing the three different apertures (6, 4 and 2) mm (from top to bottom).
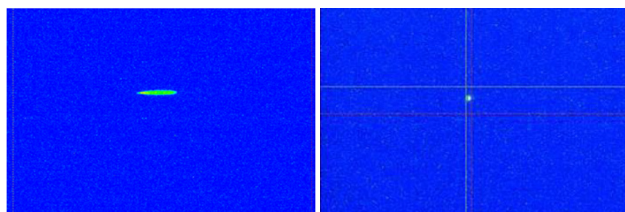
Figure 3: Energy spread as measured in the first arc for nominal operation (left) and with the linac cross-phased (right).

Installation of the test apparatus in the 3F region made the phase space exchange typically used to mitigate the multipass beam breakup instability (BBU) unavailable. Consequently, at currents above 4 mA we observed an interesting manifestation of BBU. Observant operators identified the onset of BBU by noting the characteristic vertical smearing of the beam image on a downstream synchrotron light monitor. By adjusting a vernier cavity in the linac by several 10's of keV, the vertical stripe returned to a normal round aspect ratio and the instability was averted. This behavior was due to the strong focusing needed to create a waist at the aperture (see Fig. 4), which

led to higher than usual chromaticities; small fluctuations in the beam energy were thus sufficient to modify the turn-to-turn transfer matrix and lower the BBU threshold current. With a vigilant operator, however, the onset could be identified and controlled before the machine tripped.
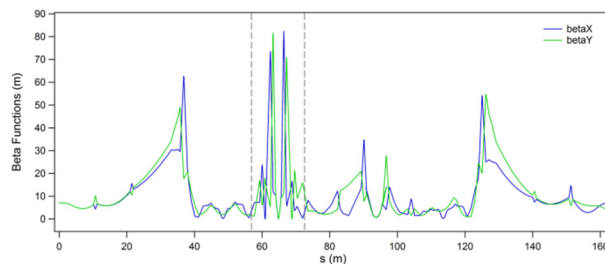
Figure 4: Beta functions in the LERF for the aperture test. The 3F region is marked by dashed lines. Note the strong focusing and beam waist at 65 m.

2015: RE-COMMISSIONING

In 2014 the FEL was renamed the Low Energy Recirculator Facility and rather than being a standalone, largely self-supported group, was absorbed into the Accelerator Division. Perhaps the most important consequence of the realignment is the LERF is now operated by members of the Operations group with supervision and guidance from subject matter experts. This presents a challenging transition since the FEL was never a user-facility, but rather an R&D platform in which beam and lattice configurations were always subject to change. Only a handful of "standard procedures" exist and trying to proceduralize 15 years of institutional knowledge is difficult, though progress is continually being made. An additional constraint is that due to the limited size of the Operations group, CEBAF and the LERF cannot be operated simultaneously.

In the fall of 2015 several days were dedicated to re-establish the configuration from the 2012 aperture test. Apart from expected minor hardware issues after 3 years of inactivity, the commissioning of the machine was incredibly efficient. During that period the gun was at its operating voltage of 350 kV for 70 hours (i.e. the amount of time operation with beam was possible). And in that span of time the machine was setup sufficiently to run CW beam. One major modification of the beamline from the 2012 run was the installation of a refurbished cryomodule (F100) in the first slot of the linac. This is the same cryomodule characterized by poor HOM damping, which

lead to the onset of the beam breakup instability (BBU) [4]. Whereas previously the module was in the second linac slot, with its current location at the start of the linac where the beam energy is lower, the beam breakup threshold was expected to be lower than initially measured (2.5 mA for the nominal configuration without invoking the phase space exchange). In fact during the few minutes we ran CW beam (the photocathode quantum efficiency was dropping precipitously) we observed the tell-tale signs of the onset of BBU – repeatable machine trips at a given current due to localized beam loss and an associated vertical smear on the downstream synchrotron light monitor – at currents less than 2 mA (see Fig. 5).
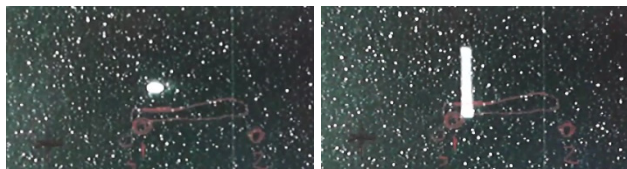
Figure 5: Screenshot of an SLM showing stable operation (left) and at the onset of BBU (right).

2016: ENGINEERING RUN

With the success of the aperture test, several weeks in 2016 were allocated to commissioning the machine with the DarkLight experimental package installed. The interaction region was installed in place of the IR wiggler (4F region) and consists of a 0.77 m long gaseous hydrogen target, detector, 5 kG solenoid and Moller dump. A staged approach was taken wherein commissioning started with only the solenoid and Møller dump installed ("engineering run"), followed by a run with the target installed ("target run"). Significant re-work immediately upstream and downstream of the interaction region were required to integrate the experimental package. The beamline must match (transversely and longitudinally) the beam to the target, ensure that the linac-to-linac transport exchanges the transverse phase spaces (to mitigate BBU), and cleanly transport a degraded beam to the dump. After interacting with the target, the electron beam will have increased energy spread, transverse size and be transversely coupled. To achieve a swap of the transverse phase spaces, skew five-quadrupole telescopes were embedded between two triplets for each side of the interaction region to complete the solenoid-induced partial phase space exchange (21.5° from each telescope and 47° from the solenoid). A schematic of the beamline is shown in Fig. 6. By uniformly distributing the exchange modest quadrupole strengths are maintained so as to avoid ringing in the beam envelopes – alleviating aberrations and helping to avoid beam losses from the degraded beam [5].
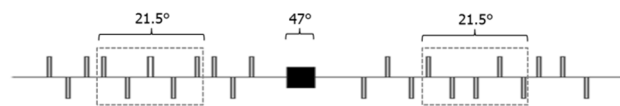
Figure 6: Schematic of the 4F beamline showing the target (black box) and skew quadrupole telescopes on either side.

Operation of the machine deviated from the previous practice of running 12 hour day shifts. With around the clock staffing available from the Operations group, we ran 24 hours/day for 8 days. The primary goal of the engineering run was to exercise high beam power (CW beam up to 4.5 mA at 100 MeV) with the skew quadrupoles and solenoid on. However a number of factors precluded us from being able to establish a lossless, CW setup even with the skew quadrupoles and solenoid off. We experienced considerable growing pains in making the transition to an element database. For much of the engineering run magnet settings from previous all-saves were not loaded correctly or the incorrect field map was being applied. Not being able to trust magnet settings – in addition to troubleshooting a variety of diagnostics systems (BPMs, viewers, Happek bunch length monitoring system) – created less-than-ideal conditions for a major rework of the machine setup. It was also discovered that when powered, the solenoid generated significant vertical steering due to a winding issue which proved difficult to correct. Though unable to achieve a CW-compatible machine setup, we were able to run 6% duty factor at 1.25 mA with minimal losses.

2016: TARGET RUN

The goal of the target run was to pick up where the engineering run left off and be able to run high beam power with the target installed – which includes a series of Kapton baffles, with small (3 mm diameter) apertures and differential pumps to isolate the target from the ERL transport system. Despite being able to match the beam to the solenoid and correcting for the vertical kick, transmission through the interaction region was poor. A post-mortem on the target baffles revealed that they were misaligned – there simply was no way to achieve good beam transmission. Losses on the apertures and the inability to energy recover precluded CW operation with high power beam. Nevertheless, the DarkLight collaboration was able to exercise the target with 300 mTorr of gas and demonstrate stable operation of the system. Data was also recorded with and without gas in the target for various solenoid settings. Under these conditions, there was no obvious effect on the electron beam.

Toward the end of the run opportunities became available to characterize the beam at multiple points in the machine using quadrupole scans to extract the emittance and Twiss parameters [6]. Data was taken in the 2F region (before the first Bates bend), in the 3F region (before the optical cavity chicane) and in the 4F region (before the DarkLight solenoid). Results of the analysis are summarized in Fig. 7. It is clear that there is degradation of the horizontal emittance after traversing the first Bates bend. In a typical LERF setup for FEL operation there are multiple parasitic compressions in the arc (where the bunch goes through a full compression), this would not be at all surprising. However, since the beam is cross-phased and does undergo over-compression, it is unclear what the source of degradation is. There also appears to be a jump

in the vertical emittance in the 3F region. Note that the data was taken on two separate occasions a week apart and in the intervening period the gun photocathode was re-cesiated, which may account for some of the discrepancy.

As is often the case, as the running period came to an end the machine was just hitting its stride. Many of the hardware issues had been resolved and the various sub-systems (gun, drive laser, RF, magnets, most diagnostics) were running well.
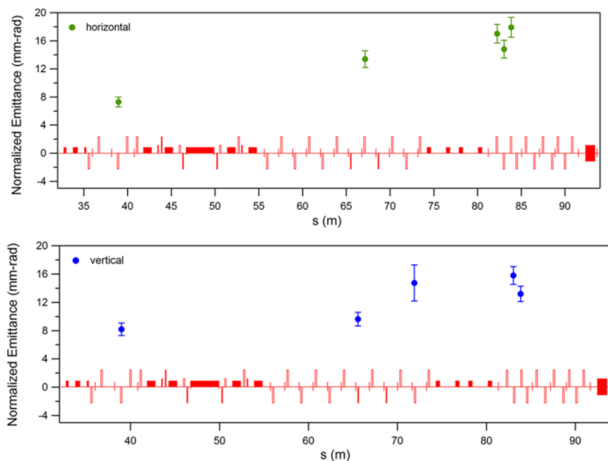
Figure 7: Measured normalized horizontal (top) and vertical (bottom) emittances from the exit of the linac to the exit of the target.

LOOKING FORWARD

Though the results of the target run were encouraging, there remain of number of issues to work through before a dedicated DarkLight physics run can commence. Achieving alignment of the target baffles and correction of detector solenoid deflecting fields are the highest priorities so as to allow full beam transmission through the interaction region. Many of the software and hardware issues that plagued us early on have been resolved and the operations staff is now proficient with LERF operations. Despite the challenges and a shorter than anticipated run schedule, in the end beam was run to an internal target with thickness 10^{18} cm^{-2} – representing a three order of magnitude increase in thickness from previous internal target experiments.

In addition to supporting DarkLight, there are a wide range of other proposals for using the LERF. Looking to the immediate future, the laboratory's highest priority is the design of the Jefferson Laboratory Electron-Ion Collider (JLEIC), a machine which collides polarized electrons (originating from CEBAF) with medium energy ions (originating from a new ion complex) [7]. In order to achieve the specified luminosity (10^{-34} cm^{-2}s^{-1}), several stages of electron beam cooling are utilized. The most challenging is the high energy, bunched beam cooler designed to cool 100 GeV protons. The cooler requires handling a low energy, high power electron beam. The current baseline design uses an ERL to accelerate and condition the beam for delivery to a non-equilibrium

circulating cooler ring (CCR) where it makes up to 20 turns before being returned to the ERL via a beam exchange region for recovery. Several key areas of technical risk could be addressed in the LERF, some requiring little modification (studies of CSR shielding) and some requiring significant changes to the existing infrastructure (installing a CCR and testing the design of the beam exchange region).

Other novel applications are being considered as well. In addition to its ability for high power lasing in the IR and UV regimes, the LERF is being considered for medical isotope production, studying photonuclear activation at low energy and as a source of intense positrons [8].

REFERENCES

[1] R. Alacorn *et al.*, Phys. Rev. Lett. **111**, 164801 (2013).

[2] P. Fisher *et al.*, JLAB PR12-11-008 (2011).

[3] D. Douglas *et al.*, JLAB TN 13-009 (2012).

[4] C. Tennant *et al.*, Phys. Rev. ST. Accel. Beams, **8**, 074403 (2005)

[5] D. Douglas, *JLAB TN in preparation*.

[6] C. Tennant, JLAB TN 16-047 (2016).

[7] S. Abeyratne *et al.*, arXiv:1504.07961 (2015).

[8] https://www.jlab.org/indico/event/199/

PERLE – BEAM OPTICS DESIGN*

S.A. Bogacz, Jefferson Lab, Newport News, VA, USA

Abstract

PERLE (Powerful ERL for Experiments) [1] is a novel ERL test facility, initially proposed to validate design choices for a 60 GeV ERL needed for a future extension of the LHC towards a hadron-electron collider, the LHeC [2]. Its main goal is to test the limits of a high current, CW, multi-pass operation with superconducting cavities at 802 MHz (and perhaps exploring other frequencies of interest). PERLE optics features Flexible Momentum Compaction (FMC) lattice architecture for six vertically stacked return arcs and a high current, 5 MeV photo-injector. With only one pair of 4-cavity cryomodules, 400 MeV beam energy can be reached in three re-circulation passes, with beam currents in excess of 15 mA. This unique quality beam is intended to perform a number of experiments in different fields reaching from uncharted tests of accelerator components via elastic ep scattering to laser-Compton backscattering for photon physics [3]. Following the experiment, the CW beam is decelerated in three consecutive passes back to the injection energy, transferring virtually stored energy back to the RF.

LAYOUT AND ENERGY

PERLE accelerator complex is arranged in a racetrack configuration; hosting two cryomodules (containing four, 5-cell, cavities operating at 802 MHz), each located in one

---

of two parallel straights, completed with a vertical stack of three recirculating arcs on each side. The straights are about 10 meter long and the 180° arcs are 5.5 meter across. Additional space is taken by 4 meter long spreaders / re-combiners, including matching sections. As illustrated in Fig. 1, the total 'footprint' of PERLE is: 24 m × 5.5 m × 0.8 m; the last dimension reflecting 40 cm vertical separation between the arcs. Each of the two cryomodules provides 65.5 MeV energy boost. Therefore, in three turns, a 393 MeV energy increase is achieved. Adding initial injection energy of 5 MeV yields the total energy of 398 MeV – call it '400 MeV'.

MULTI-PASS LINAC OPTICS WITH ENERGY RECOVERY

Multi-pass energy recovery in a racetrack topology explicitly requires that both the accelerating and the decelerating beams share the individual return arcs. This in turn, imposes specific requirements for the TWISS function at the linacs ends: the TWISS functions have to be identical for both the accelerating and decelerating linac passes converging to the same energy and therefore entering the same arc.

To represent beta functions for multiple accelerating and decelerating passes through a given linac, it is convenient to reverse the linac direction for all decelerating passes and string them together with the interleaved accelerating passes, as illustrated in Fig. 2. This way, the corresponding
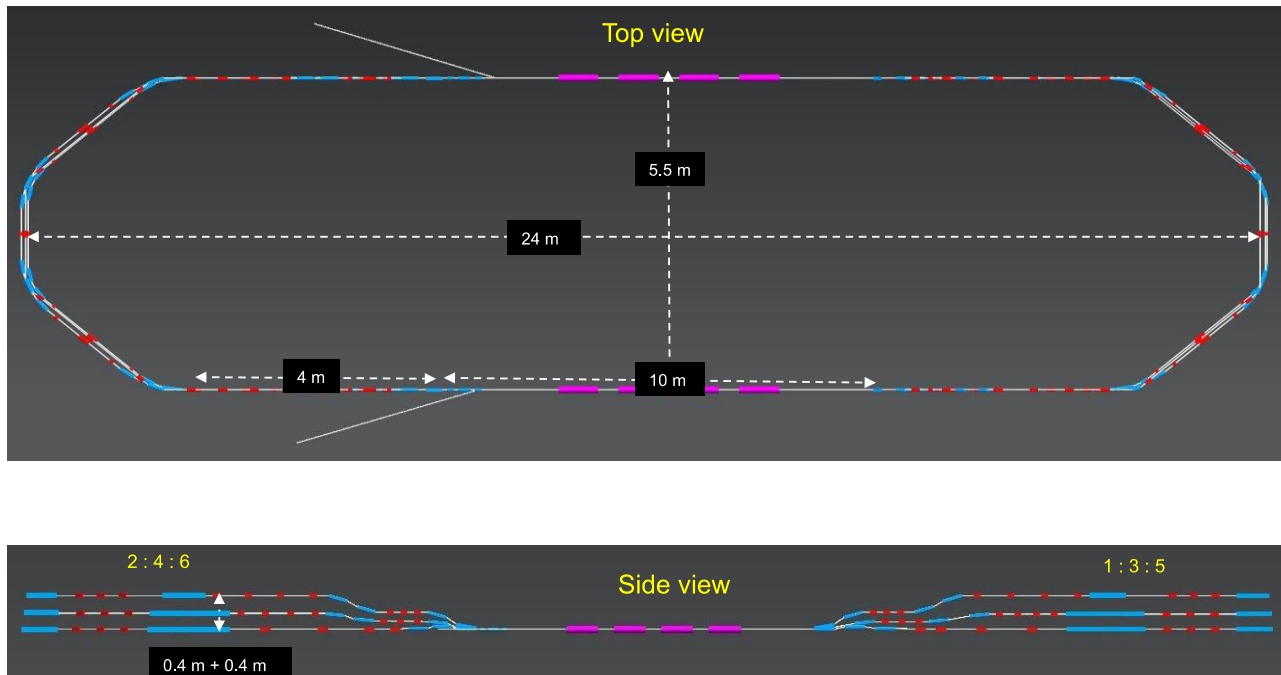
Figure 1: PERLE layout featuring two parallel linacs each hosting a 65.5 MeV cryomodule, achieving 400 MeV in three passes.

TUIDCC001
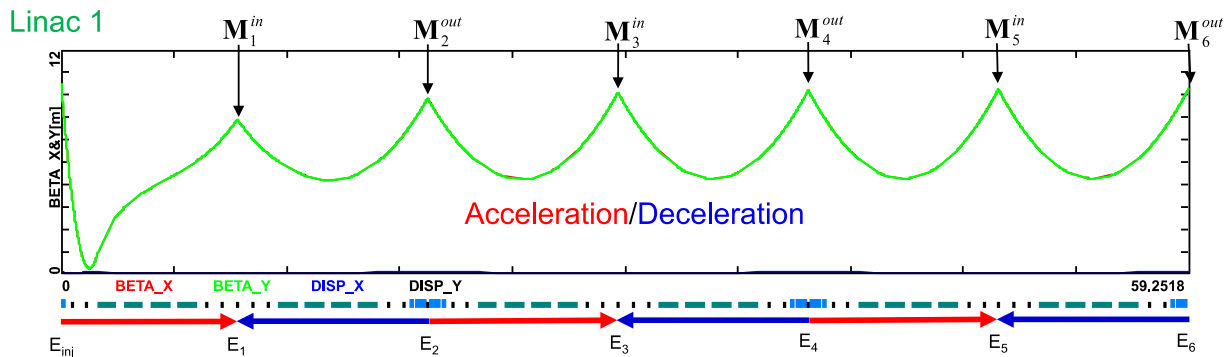
Figure 2: Multi-pass linac optics. Green curve illustrates symmetrically optimized beta functions across different passes through the linac; Red/Blue arrows indicate the accelerating/decelerating passes.

accelerating and decelerating passes are joined together at the arcs entrance/exit, automatically satisfying the matching conditions into the arcs.

Injection at 5 MeV into the first linac is done through a fixed field injection chicane, with its last magnet (closing the chicane) being placed at the beginning of the linac. It closes the orbit 'bump' at the lowest energy, injection pass, but the magnet (physically located in the linac) will deflect the beam on all subsequent linac passes. In order to close the resulting higher pass 'bumps', the so-called reinjection chicane is instrumented, by placing two additional opposing bends in front of the last chicane magnet. This way, the re-injection chicane magnets are only 'visible' by the higher pass beams.

The seecond linac in the racetrack is configured exactly as a mirror image of the first one, with a replica of the re-injection chicane at its end, which facilitates a fixed-field extraction of energy recovered beam to the dump (at 5 MeV).

RECIRCULATING ARC ARCHITECTURE

The spreaders are placed directly after each linac to separate beams of different energies and to route them to the scorresponding arcs. The recombiners facilitate just the opposite: merging the beams of different energies into the same trajectory before entering the next linac.

As illustrated in Fig. 3, each spreader starts with a vertical bending magnet, common for all three beams, that initiates the separation. The highest energy, at the bottom, is brought back to the initial linac level with a chicane. The lower energies are captured with a two-step vertical beamline. The vertical dispersion introduced by the first step bends is suppressed by the three quadrupoles located appropriately between the two steps. The lowest energy spreader is configured with three curved bends following the common magnet, because of a large bending angle (45°) the spreader is configured with. This minimizes adverse effects of strong edge focusing on dispersion suppression for a lower energy spreader. Following the spreader, there are four matching quads to 'bridge' the TWISS function between the spreader and the following 180° arc (two betas and two alphas).

All six, 180° horizontal arcs are configured with the FMC optics to ease individual adjustment of M_{56} in each arc (needed for the longitudinal phase-space re-shaping, essential for operation with energy recovery). The lower
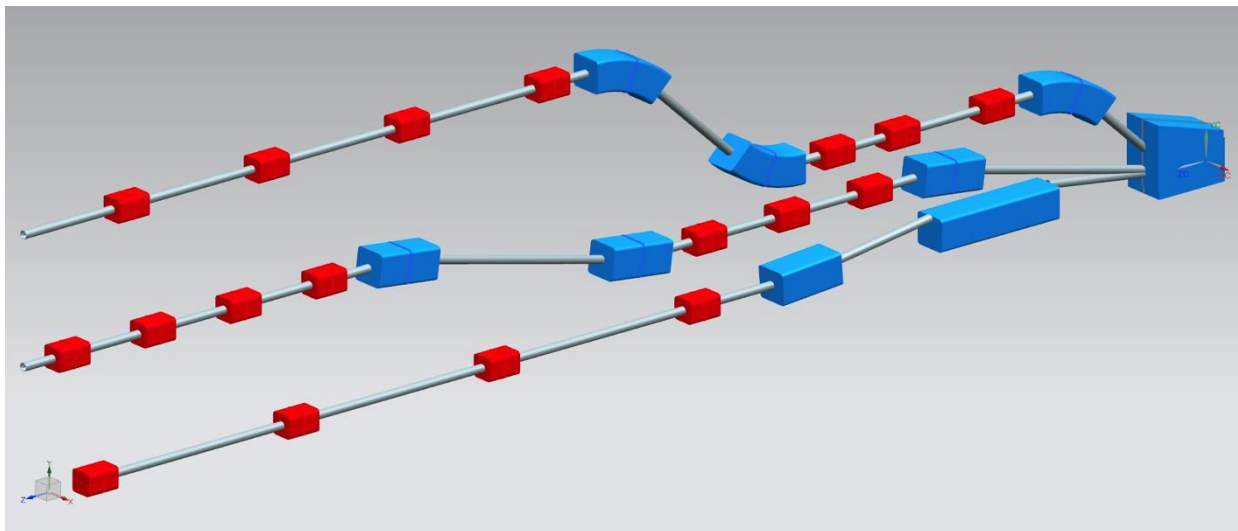
Figure 3: Layout of a three-beam switchyard with the corresponding energy ratios: 1:3:5.
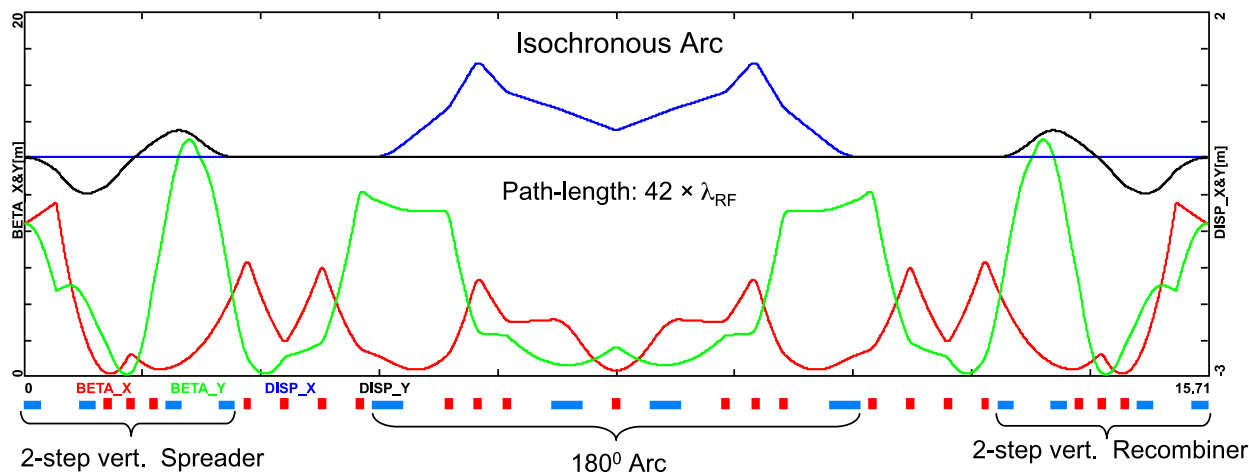
Figure 4: Optics based on the FMC cell for the lowest energy return arc. Horizontal (red curve) and vertical (green curve) beta-function amplitudes are illustrated. Blue and black curves represent the horizontal and vertical dispersion, respectively. The arc, as configured above, is tuned to the isochronous condition ($M_{56} = 0$).

energy arcs (1, 2, 3) are composed of four 45.6 cm long curved 45° bends and of a series of quadrupoles (two triplets and one singlet), while the higher arcs (4, 5, 6) use 'double length', 91.2 cm long, curved bends. The usage of curved bends is dictated by a large bending angle (45°). If rectangular bends were used, their edge focusing would have caused significant imbalance of focusing, which in turn, would have had adverse effect on the overall arc optics. Another reason for using curved bends is to eliminate the problem of magnet sagitta, which would be especially significant for longer, 91 cm, bends. Each arc is followed by a matching section and a recombiner (mirror symmetric to previously described spreader and matching section). As required in case of mirror symmetric linacs, matching conditions described in the previous section, impose a mirror symmetric arc optics (identical betas and sign reversed alphas at the arc ends). A complete lattice for arc 1 at 70.5 MeV, including a spreader, 180° horizontal arcs and a recombiner, is illustrated in Fig. 4. Presented arc optics features high degree of modular functionality to facilitate momentum compaction management, as well as orthogonal tunability for both the beta functions and dispersion.

The path-length of each arc is chosen to be an integer number of RF wavelengths, except for the highest energy pass, arc 6, whose length is longer by half of the RF wavelength (to shift the RF phase from accelerating to decelerating, switching to the energy recovery mode).

OUTLOOK – FUTURE STUDIES

We are presently launching a vigorous R&D program to develop a Technical Design Report for PERLE at Orsay, within the next year. To achieve this goal, we have tentatively identified the following sequence of accelerator design studies:

- Linear lattice optimization
- Initial magnet specs

- Momentum acceptance and longitudinal match
- End-to-End simulation with synchrotron radiation, CSR micro-bunching (ELEGANT)
- Correction of nonlinear aberrations (geometric & chromatic) with multipole magnets (sext. and oct.)
- RF cavity design and optimization, HOM content
- Multi-pass BBU studies (TDBBU)
- Injection line/chicane design including space-charge studies at injection
- Diagnostics & Instrumentation
- Multi-particle tracking studies of halo formation
- Final magnet specs
- Engineering design

ACKNOWLEDGEMENT

REFERENCES

[1] G. Arduini et al, 'PERLE: Powerful ERL for Experiments – Conceptual Design Report' accepted for publication in Journal of Physics G (2017)

[2] D. Pellegrini, A. Latina, D. Schulte, S.A. Bogacz, 'Beam-dynamics Driven Design of the LHeC Energy Recovery Linac', PRST-AB, **18**, 121004 (2015)

[3] E. Jensen et al, 'PERLE - a Powerful ERL Facility Concept', Proceedings of Nuclear Photonics Conference, Monterey, CA (2016)

CBETA FFAG BEAM OPTICS DESIGN*

J. S. Berg†, S. Brooks, F. Méot, D. Trbojevic, N. Tsoupas,
Brookhaven National Laboratory, Upton, NY, USA
J. Crittenden, Y. Li, C. Mayes, Cornell University, Ithaca, NY

Abstract

CBETA is an Energy Recovery Linac (ERL) accelerating an electron beam to 150 MeV in four linac passes. Instead of having four separate return loops to the linac, it instead has a single fixed field alternating gradient (FFAG) beamline with nearly a factor of 4 energy acceptance. While ideally the FFAG would be circular with identical cells all around, space and cost considerations dictate that small radius of curvature FFAGs should be used near the linac, connected by a straight beamline. To ensure good orbit matching over the entire energy range, adiabatic transitions are inserted between the arcs and the straight. After briefly introducing basic principles of FFAG optics, we describe how we choose the parameters of the arc cell, the basic building block of the lattice. We then describe how the straight cell is chosen to work well with the arc. Finally we describe the design process for the transition that ensures orbits over the entire energy range end up very close to the axis of the straight. We discuss how the realization of this lattice design with physical magnets impacts the design process.

Table 1: Basic parameters for the FFAG return line.

Total energy, pass 1 (MeV)	42
Total energy, pass 2 (MeV)	78
Total energy, pass 3 (MeV)	114
Total energy, pass 4 (MeV)	150
Focusing quadrupole length (mm)	133
Defocusing magnet length (mm)	122
Minimum short drift length (mm)	66
Minimum long drift length (mm)	123
Arc radius of curvature, approximate (m)	5.1
Arc cell bend angle (deg.)	5
Cells per arc	16
Cells per transition section	24

energy from the linac to the FFAG line or from the FFAG line back to the linac.

The FFAG return line has arcs at its ends (FA and FB in Fig. 1) with a relatively small bending radius to keep the machine compact. Completing the return to the linac requires a section that is straight (ZA and ZB in Fig. 1) to connect the two arcs. We connect the arcs to the straights with adiabatic transition sections (TA and TB in Fig. 1).

Table 1 describes the basic requirements for the FFAG line design. The energies correspond to a four-pass energy recovery linac with a 6 MeV injection energy. The minimum drift lengths result from allowing space for various devices (the short drift allows for a button beam position monitor (BPM), the long drift will allow for a wide variety of devices) and any overhang of magnet hardware. The radius of curvature is a result of a space limitation. The magnet lengths and maximum energy are parameters related to an earlier design using an iron-dominated magnet design, but are reasonable choices that were retained.

Each arc has 16 cells, giving 80 degrees of bend. The transition will be designed with a symmetry such that the average bend per cell is half the arc cell bend angle. Thus each transition section supplies 60 degrees of bend. Thus each spreader/combiner supplies the remaining 40 degrees of bend for half the machine.

Every focusing quadrupole will have a horizontal corrector (vertical dipole field), while every defocusing magnet will have a vertical corrector.

Figure 1: The CBETA energy recovery linac, with sections labeled. The FFAG beamline, discussed in this paper, consists of the sections labeled FA, TA, ZA, ZB, TB, and FB.

THE BASIC PARAMETERS

CBETA [1], illustrated in Fig. 1, is an energy recovery linac that will make 4 accelerating passes through the linac, and return the beam to the linac using a single fixed field alternating gradient (FFAG) return line, which must simultaneously transport beams from all passes, ranging in energy from 42 MeV to 150 MeV. At the ends of the linac are 4 spreader/combiner lines, each of which transports a single

ARC CELL

The arc cell is the basic building block for the FFAG beam line. An illustration is given in Fig. 2. The basic cell is a doublet, consisting of a focusing quadrupole and a combined function magnet with a dipole and defocusing

---
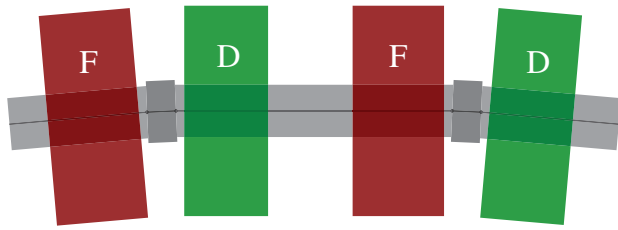
Figure 2: Illustration of FFAG arc cell geometry, showing two full cells. Lines show the reference geometry, with dots delimiting the ends of the segments. Magnet offsets are the distance of the magnet ends from the nearest dot. Segments bend by half the cell bend angle at each dot.

Table 2: Parameters for the arc cell.

BPM block length (mm)	42
Pipe length (mm)	402
Magnet offset from BPM block (mm)	12
Focusing quadrupole length (mm)	133
Defocusing magnet length (mm)	122
Single cell horizontal tune, 42 MeV	0.368
Single cell vertical tune, 150 MeV	0.042
Integrated focusing magnet strength (T)	-1.528
Integrated defocusing magnet strength (T)	$+1.351$
Integrated field on axis, defocusing (T m)	-0.03736

quadrupole component. The geometry is defined to relate to the vacuum chamber design, which consists of 42 mm BPM blocks connected by straight beam pipes. It is thus defined by a sequence of straight lines, which bend by half the cell angle where they join. The parameters that define the geometry are given in Table 2. The BPM blocks are centered in the short drift between the magnets. The precise value for the pipe length was chosen to help get the correct value of the time of flight for the entire machine.

Once the longitudinal lengths are fixed, there are three free parameters: two magnet gradients, and the dipole field in the defocusing magnet. The parameters are chosen so that the maximum horizontal closed orbit excursion at 150 MeV and the minimum horizontal closed orbit excursion at 42 MeV, relative to the line defining the coordinate system, are of equal magnitude and opposite sign.

The remaining two degrees of freedom are used to set the tunes at the working energies. When we discuss "tunes" we are referring to a single cell, treated as a periodic system. High horizontal and low vertical tunes generally reduce orbit excursions and magnet gradients. However, one must avoid the horizontal half-integer resonance at low energy and becoming linearly unstable at high energy in the vertical plane. Furthermore, we have found that being near third-order resonances, in particular the $3\nu_x = 1$ and $\nu_x + 2\nu_y = 1$ resonances, can lead to emittance growth. This emittance growth is related to nonlinear resonances of the single cell system, without errors. The effect can be seen in Fig. 3, where we plot the 600-turn dynamic aperture rather than emittance growth, showing that there are significant drops
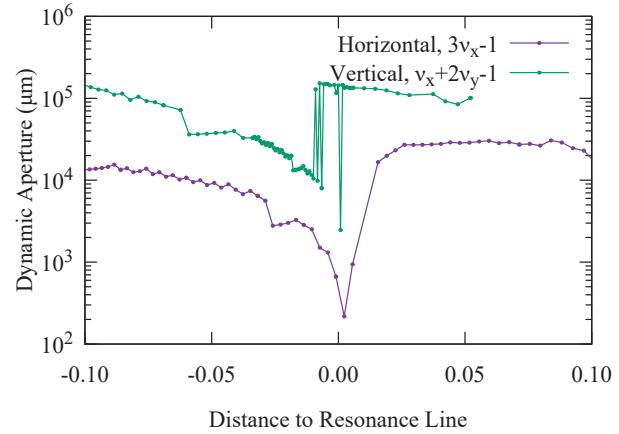
Figure 3: Horizontal and vertical dynamic apertures for the arc cell (tracked for 600 cells) at fixed energies, given as a maximum value of the normalized action, plotted against the distance from a resonance line for the zero-amplitude tune for the energy of the calculation. These are the only drops of this scale in the dynamic aperture until high energies where the vertical motion becomes unstable or low energies where we reach a tune of 0.5 per cell horizontally.

in the dynamic aperture as we approach the $3\nu_x = 1$ and $\nu_x + 2\nu_y = 1$ resonance lines. Note that the dynamic apertures away from those resonance lines are well beyond the beam's normalized emittance of 1 μm.

We have chosen our working point in the tune plane by considering how much gradients would need to change to reach problematic resonance lines. We quantify this change by

$$\sqrt{\left(\frac{\Delta B_{1F}}{B_{1F}}\right)^2 + \left(\frac{\Delta B_{1D}}{B_{1D}}\right)^2} \qquad (1)$$

where B_{1F} (B_{1D}) refers to the gradient of the (de)focusing magnet. We find the minimum value for this quantity for values meeting the resonance condition in question, and define that to be the parametric distance. The working point is chosen so that the parametric distance of the 150 MeV point to the $\nu_y = 0$ line is approximately equal to the parametric distance of the 42 MeV point to the $\nu_x + 2\nu_y = 0$ line, and the parametric distances of the 150 MeV and 114 MeV points to the $\nu_x - 2\nu_y = 0$ line are about the same. The resulting working point is reasonably well-defined by the 42 MeV horizontal and 150 MeV vertical tunes, which are given in Table 2. The parametric distance to the $\nu_x + 2\nu_y = 0$ line is 3.8%, to the $\nu_y = 0$ line is 3.7%, and to the $\nu_x - 2\nu_y = 0$ line is 1.2% for both energies.

The computation of the parameters is performed using field maps generated by the finite element software OPERA. Field maps for an initial estimate for the magnet designs are created, and these field maps are scaled and shifted to achieve the desired orbit centering and tune working point. Magnet designs are then modified to have the resulting integrated gradient and central field, field maps are computed from those designs, and the results are checked (and were found
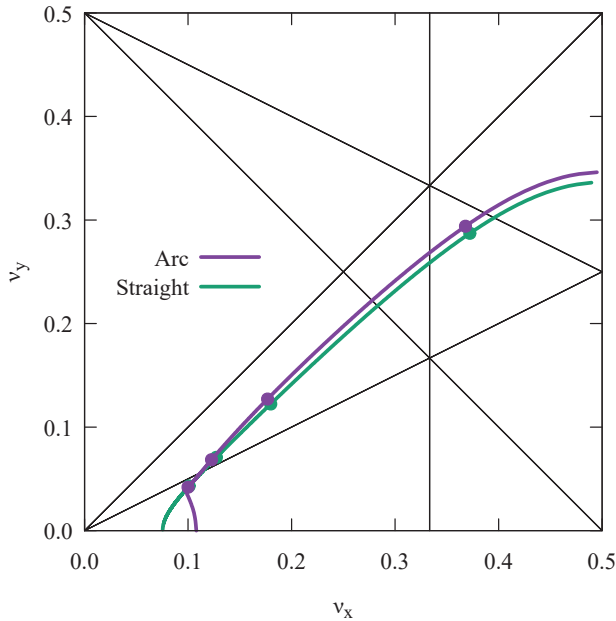
Figure 4: Tune per cell for the arc and straight cells, treated as periodic. Design energies are shown with dots. Computations are made with field maps for Halbach magnet designs.
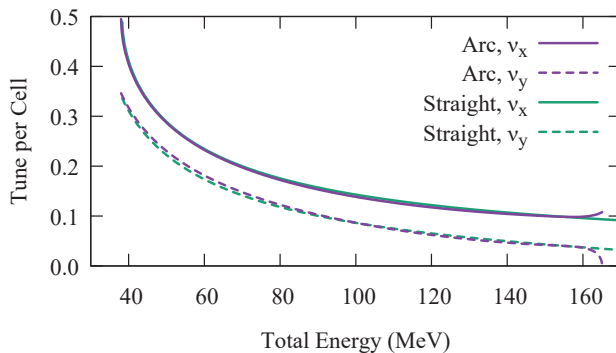
Figure 5: Tune per cell for the arc and straight cells, treated as periodic, as a function of energy. Computations are made with field maps for Halbach magnet designs.

to be in good agreement). Figures 4 and 5 show the tune per cell for the arc cell, and Fig. 6 shows the periodic orbits in the arc cell.

STRAIGHT CELL

The transition will adiabatically distort the lattice cell from the arc cell to a straight cell. We should thus first decide the parameters of the straight cell. To keep the transition smooth, all magnets of a given type (focusing/defocusing) will have the same integrated gradient and length. In addition, we will use the same focusing quadrupole everywhere. We will, however, use different types of defocusing magnets, differing in the integrated field on their axis. In particular, the defocusing magnet for the straight section will have zero field on its axis.

Table 3: Parameters for the straight cell.

BPM block length (mm)	42
Pipe length (mm)	413
Magnet offset from BPM block (mm)	17.5
Focusing quadrupole length (mm)	133
Defocusing magnet length (mm)	122
Straight cell count	27

If the longitudinal lengths in the straight cell are identical to those of the arc cell, the tunes and Courant-Snyder betatron functions would differ between the arc and the straight cells due to additional focusing occurring due to the curved paths the particles take through the arc magnets. Our goal is to make the tunes of the straight cell as close as possible to those of the arc cell. The only parameters available to do this are the drift lengths. The criterion used to determine the best fit is

$$\sum_p \left[\sum_i T_{p,\text{str}}(E_i) - T_{p,\text{arc}}(E_i) \right]^2 \qquad (2)$$

where $T_{p,\text{str}}(E)$ is the trace of the transfer matrix at energy E for plane p (*i.e.*, twice the cosine of the phase advance) for the straight cell, and similarly $T_{p,\text{arc}}(E)$ for the arc cell. Fig. 7 shows this criterion plotted when varying the drift lengths. Note there is a optimum along the dark band shown in the figure. It is slightly more favorable to be toward the longer magnet offset end of that band. However, if we wish to keep the long drift length at least as long as it is in the arc, then there is a limit to how large an offset one can use. We thus choose the parameters in Table 3. The corresponding tunes are shown in Figs. 4 and 5.

TRANSITION

The goal of the transition is to bring the orbits in the arc at and near the design energies onto the axis in the straight. It accomplishes this by adiabatically varying the cell parameters from those in the arc to those in the straight. The adiabatic variation allows the entire energy range to end up very close to the axis in the straight. At that point, to get the correction exactly right at the design energies, the correctors can be used, and the strengths required will be very small if the transition works well.

To measure the effectiveness of the transition, we begin with the periodic orbit in the arc cell, transport it through the transition, and determine the normalized action in the straight cell when the straight cell is treated as periodic. The normalized action is

$$J_{\text{str}}(E) = \frac{1}{2m_e c} \left(\gamma_x p x^2 + 2\alpha_x x p_x + \frac{\beta_x}{p} p_x^2 \right) \qquad (3)$$

where β_x, α_x, and γ_x are the Courant-Snyder functions for the straight cell, p is the total momentum for the orbit, x is the horizontal position and p_x is the horizontal momentum. The values of J_{str} give an approximation to the emittance
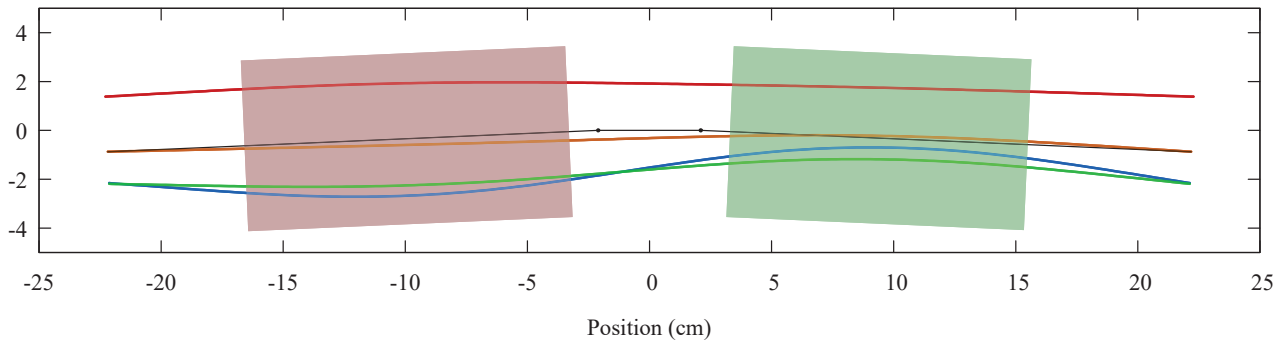
Figure 6: Periodic orbits in the arc cell. Also shown are the coordinate reference segments and the nominal magnet positions. The width of the magnets shown is equal to the pipe aperture in the midplane.
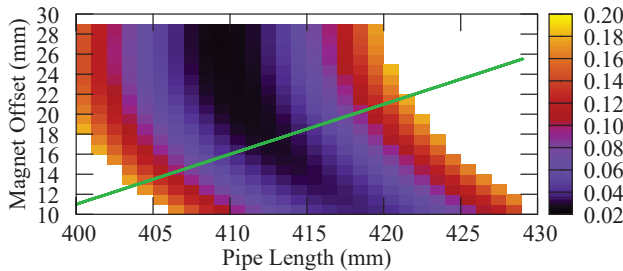
Figure 7: Quantity in Eq. (2) as a function of the pipe length (distance between the ends of the BPM blocks and offset length (distance of quadrupole ends from the ends of the BPM blocks) in the straight cell. Line drawn corresponds to a long drift length equal to that of the arc cell (123 mm).
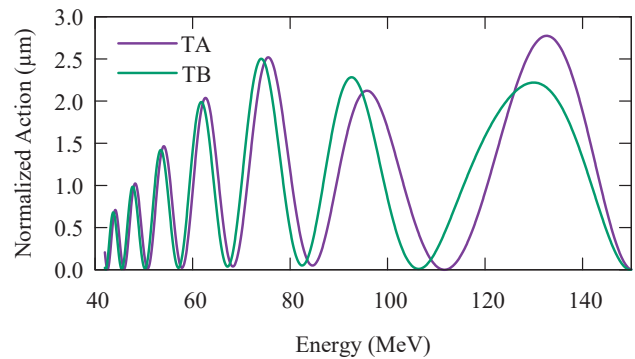
Figure 8: $J_{str}(E)$ for the transition using the taper parameters, using a hard edge model.

growth, and should therefore be compared to the normalized emittance of the beam, which is 1 μm.

Each parameter p being varied has a value p_i at cell i given by

$$p_i = \left[1 - f_T\left(\frac{i}{n_T + 1}\right)\right] p_{arc} + f_T\left(\frac{i}{n_T + 1}\right) p_{str} \quad (4)$$

where cell 1 is adjacent to the straight and cell $n_T = 24$ is adjacent to the arc. The parameters varied are the lengths of the drifts, bend angle at the BPM block, and the distance of the axis where the integrated field of the defocusing magnet is zero from the coordinate axis for the cell. The start/end of the cell is such that the distance from the end of the BPM block to the corresponding end of the cell is the same on either side of the cell.

The transition function f_T is of the form

$$f_T(x) = \frac{1}{2} + \left(x - \frac{1}{2}\right) \sum_{k=0} a_k \binom{2k}{k} x^k (1-x)^k \quad (5)$$

where we will determine the coefficients a_k that give the best behavior. Since $f_T(1 - x) = f(x)$, the average angle per cell is half the arc cell bend angle, which simplifies the design process by allowing the total bend angle to remain invariant as the a_k are varied. $f_T(0) = 0$ and $f_T(1) = 1$ if $a_0 = 1$. If a_0 through a_n are 1, the function will have n continuous derivatives at $x = 0$ and $x = 1$.
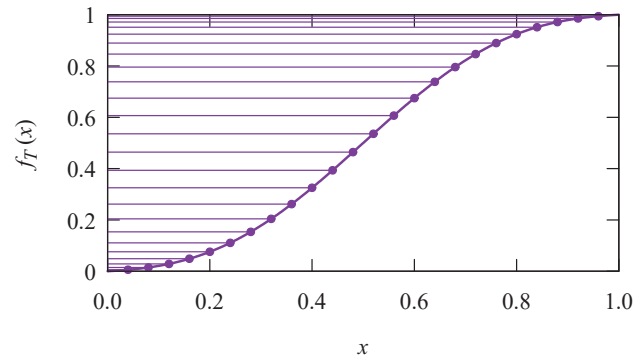
Figure 9: $f_T(x)$ used for the transition. Dots show the values used for the individual transition cells.

Since the phase advance is larger at lower energies, better continuity in the function will lead to smaller J_{str} for lower energies. However, higher degrees of continuity at $x = 0$ and $x = 1$ require a steeper rise in the function around $x = 1/2$, thus arbitrarily improving continuity at the ends will not improve the transition performance indefinitely. Furthermore, at higher energies, where the phase advance is lower and

Table 4: a_k in f_T used for the transitions.

a_0: 1.000	a_1: 0.894	a_2: 0.659	a_3: 0.329

TUIDCC004

Table 5: Magnet types used in the FFAG return line, and horizontal positions, relative to the physical magnet center, of where their integrated fields are zero.

BD: 27.642 mm	BDT2: 24.080 mm
QD: 0.000 mm	BDT1: 9.629 mm
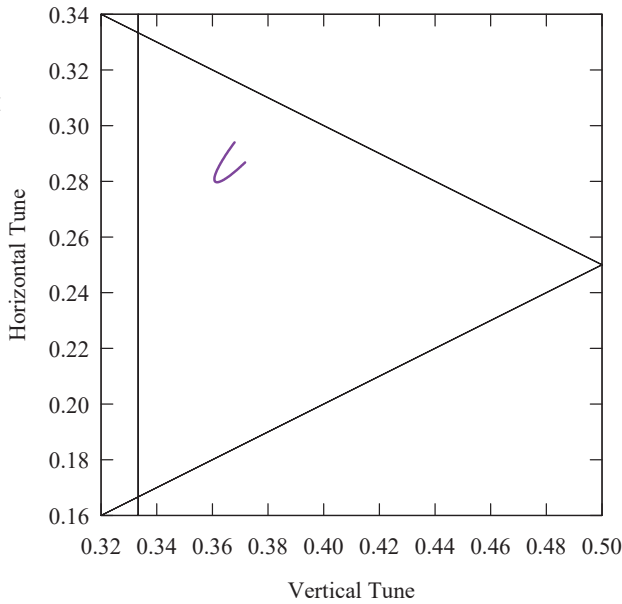
Figure 10: Tunes for a periodic cell, with angles, lengths, magnet displacements, and gradients for a hard edge model varied linearly as described in the text. Parameters vary from arc parameters to straight parameters. Computation is done using the hard-edge model described in the text.

therefore the system becomes less adiabatic, using the coefficients a_k as adjustable parameters allows one to reduce the maximum J_{str} over the entire energy range.

The linear variation in the parameters results in tunes that, rather than lying directly between the tunes for the arc and the straight, wander somewhat further from those tunes for intermediate values of f_T (Fig. 10). However, attempting to instead keep the tunes (or the traces) on a straight line between those of the arc and the straight results in a transition with significantly worse $J_{str}(E)$. It appears this is because there is a focusing term which is proportional to the square of the angle, and thus when the angle varies linearly in f_T, the focusing effect changes more rapidly at the arc end than the straight end.

In practice, we don't choose parameters that give the absolute minimum for the maximum J_{str} over the energy range for a couple reasons. First, we prefer to ensure adiabatic reduction in J_{str} at lower energies rather than adjusting parameters for the absolute minimum at higher energies; this allows lower energies to in a sense take care of themselves without being dependent on the precise choice for the a_i and fine-tuning by correctors. Second, because the doublet is not reflection symmetric in the longitudinal direction, the two transitions behave somewhat differently, and thus the

optimal coefficients are somewhat different for the two transitions. However, they are close enough that it is reasonable to choose the same coefficients for both transitions, and the penalty for doing so is small.

The coefficients were optimized using a hard-edge approximation to the lattice that attempts to give a good approximation to the low and high energy tunes and orbits. The tunes and the orbit positions at the center of the long pipe are matched at the low and high energy by adjusting quadrupole and dipole fields of the hard edge model, as well as adding thin quadrupoles to the magnet ends, offset so they have the same zero field axis as the magnet they correspond to. The drift lengths are adjusted as described above, and the modeled quadrupole gradients and the offset of the zero field axis are adjusted using f_T as well (note the gradients of the real magnets do not change). The resulting $J_{str}(E)$ is shown in Fig. 8, with the f_T used shown in Fig. 9. The corresponding a_k are shown in Table 4.

Discrete Magnet Types

The FFAG beamline uses the same focusing quadrupole throughout, but four distinct types of defocusing magnets, shown in Fig. 11. While all the defocusing magnets have the same integrated gradient, they have different integrated fields on-axis, or equivalently, a different horizontal position where the integrated field is zero. The horizontal positions where the integrated fields are zero for the different magnet types are shown in Table 5. BD is used in the arc, QD in the straight, and BDT1 and BDT2 are used in the transition.

The horizontal positions of BDT1 and BDT2 are changed depending on which cell the magnets are in, so as to have the position of the zero axis vary as described in Eq. (4). We use BDT2 when $f_T > 0.64$ and BDT1 for $f_T < 0.64$ so that, for each magnet the positive and negative shifts are approximately equal (the result is 10 BDT2 and 14 BDT1 magnets per transition). The resulting $J_{str}(E)$ is shown in Fig. 12. As can be seen, the performance of the transition is significantly worse with the maps. The underlying reason is that two different magnet types, placed with their zero-field axes in the same location, do not behave precisely the same. A simple example of the problem is shown in Fig. 13. BDT1, since it is adjacent to QD in the transition, should ideally be an adequate replacement for QD, where the line where the field is zero is a straight line. But as shown in the figure, the line where the field is zero is not precisely straight. In the QD, a particle of any energy will enter and exit with zero angle when starting along the axis. But in BDT1, for a particle to asymptotically start and end parallel to the magnet axis, it must start at a different horizontal position depending on its energy.

To attempt to correct for this, we add a systematic offset to BDT1 and BDT2 as well as the QF magnets in the corresponding sections. This function will be linear in f_T for the corresponding section:

$$\Delta x(f_T) = \Delta x(f_0)\frac{f_1 - f_T}{f_1 - f_0} + \Delta x(f_1)\frac{f_T - f_0}{f_1 - f_0} \quad (6)$$

Figure 11: Magnet blocks, longitudinal direction perpendicular to the page, for the four magnet types used in the FFAG beamline. From left to right from largest to smallest magnitude central dipole field: BD, BDT2, BDT1, QD. Color is chosen based on the angle of the block magnetization with respect to the radial direction. All magnets are drawn to the same scale.
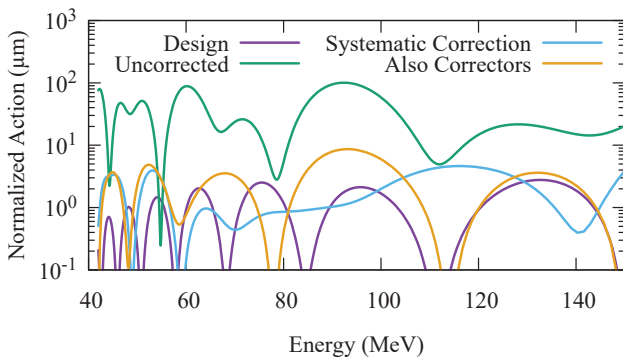
Figure 12: $J_{\mathrm{str}}(E)$ for TA. "Design" is for the hard edge model, and is the same as Fig. 8. "Uncorrected" is with field maps, when f_T alone is used to position the magnets. "Systematic Correction" applies an additional systematic correction to each magnet type as described in the text. "Also Correctors" additional applies correctors on the QF magnets in the transition to make $J_{\mathrm{str}}(E)$ be zero at the design energies.
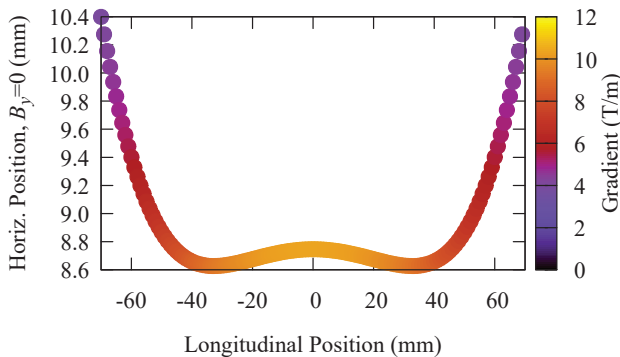
Figure 13: Points along a line where $B_y = 0$ in the midplane of BDT1. Colors show gradient along that line.

For the end point in the middle, we use 0.64. The values of Δx for the focusing and defocusing magnets at the end points

for each transition section with a given defocusing magnet type (8 values in all) are adjusted to minimize the maximum $J_{\mathrm{str}}(E)$ over the energy range. The resulting offsets are at most 190 μm, and the corresponding $J_{\mathrm{str}}(E)$ are shown in Fig. 12.

Applying Dipole Correctors

Dipole correctors can be applied to get the design energies precisely correct. The goal of the taper is to bring $J_{\mathrm{str}}(E)$ as close as possible to zero over the full energy range, to reduce the required corrector strengths required to zero $J_{\mathrm{str}}(E)$ at the design energies, and to make the design robust against systematic errors. The correctors are then applied on top of this, and the required strengths should be small.

To compute the corrector strengths, we used an iterative algorithm where a matrix computing the response of x and p_x at the straight for the design energies to changes in dipole corrector strengths is computed. Using this matrix, a linear computation is made to determine approximately the changes in corrector strengths that would zero $J_{\mathrm{str}}(E)$ at the design energies, while minimizing the sum of the squares of the changes in the corrector strengths. Starting with the corrector strengths at zero, this algorithm is repeated until the $J_{\mathrm{str}}(E)$ are zero at the design energies; in fact, one step of the algorithm gives a more than adequate estimate. The resulting $J_{\mathrm{str}}(E)$ is shown in Fig. 12. The maximum required corrector strength is 16 μT m.

REFERENCES

[1] D. Trbojevic *et al.*, "CBETA — Cornell University Brookhaven National Laboratory Energy Recovery Test Accelerator," in *Proceedings of the 8th International Particle Accelerator Conference*, Copenhagen, Denmark, May 2017, paper TUOB3, pp. 1285–1289.

ER@CEBAF - A 7 GeV, 5-PASS, ENERGY RECOVERY EXPERIMENT[*][†]

F. Méot[‡], I. Ben-Zvi, Y. Hao, C. Liu, M. Minty, V. Ptitsyn, G. Robert-Demolaize, T. Roser,
P. Thieberger, N. Tsoupas, C. Xu, W. Xu, BNL, Upton, NY, USA
M. Bevins, A. Bogacz, D. Douglas, C. Dubbé, T. Michalski, Y. Roblin, T. Satogata[‡], M. Spata,
C. Tennant, M. Tiefenback, JLab, Newport News, VA, USA

Abstract

A multiple-pass, high-energy ERL experiment at the JLab CEBAF will be instrumental in providing necessary information and technology testing for a number of possible future applications and facilities such as Linac-Ring based colliders, which have been designed at BNL (eRHIC) and CERN (LHeC), and also drivers for high-energy FELs and 4th GLS.

ER@CEBAF is aimed at investigating 6D optics and beam dynamics issues in ERLs, such as synchrotron radiation effects, emittance preservation, stability, beam losses, multiple-pass orbit control/correction, multiple-pass beam dynamics in the presence of cavity HOMs, BBU and other halo studies, handling of large (SR induced) momentum spread bunches, and development of multiple-beam diagnostics instrumentation.
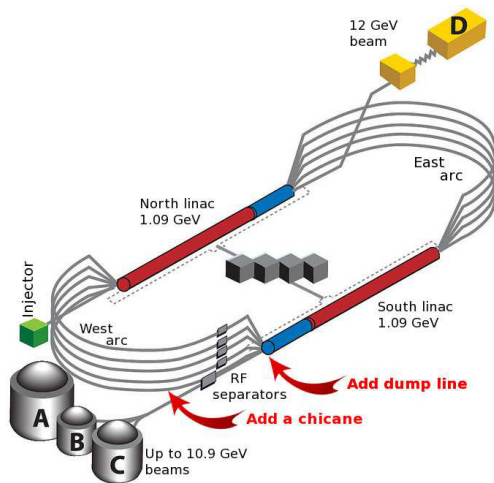
Figure 1: 12 GeV CEBAF recirculating linac. Location of chicane and dump line for ER@CEBAF.

Since it was launched 2+ years ago, the project has progressed in defining the necessary modifications to CEBAF (Fig. 1, Tab. 1, 2), including a 4-dipole phase chicane in recirculation Arc A, beam extraction and a dump line at the end of the south linac, and additional dedicated multiple-beam diagnostics. This equipment can remain in place to

Table 1: Machine/Lattice Parameters of ER@CEBAF

f_{RF}	1497	MHz	RF frequency
E_{linac}	700	MeV	Gain per linac (baseline)
E_{inj}	79	MeV	$= E_{linac} \times 123/1090$
ϕ_{FODO}	60	deg	Per cell, at first NL pass and last SL pass
M_{56}	<90	cm	Compression, Arc A
Extraction	8	deg	Angle to dump line
Dump power	20	kW	
$\Delta\phi_{tol}$	0.25	deg	Req^{ed} path-length control

Table 2: Beam Parameters

f_{beam}	31 - 499	MHz	Bunch rep. freq., CW
	7.485	MHz	Bunch rep. freq., tune mode
I_{beam}	100	μA	Max. CW beam current
q_{bunch}	0.2	pC	Bunch charge at 100 μA
σ_l	90 - 150	μm	Bunch length, high energy
σ_t	0.3 - 0.5	ps	
$\epsilon_{x,y}$	$\sim 10^{-8}$	m	Geom. emitt. at injection
dp/p	$< 10^{-4}$		Energy spread at injection
$\epsilon_{x,y}$	$\mathcal{O}(10^{-8})$	m	Geom. emitt., after ER
dp/p	2-3	%	At extraction

permit ER@CEBAF tests without hardware reconfiguration. Dedicated optics settings are required in the linacs (60° phase advance), in arcs 1 and 2 (low dispersion), as well as *ad hoc* spreader and combiner tunings for linac to arc matching. Longitudinal match will require specific settings (arc M_{56}, RF phasing). These evolutions make ER@CEBAF an expansion of CEBAF capability to a 5-pass ERL, with modest switch over time and minor impact to the CEBAF physics program.

A costing of these changes to CEBAF has been performed, amounting to below $1M. Nine months will be required to have the ER installation ready for operation.

Hardware commissioning will include 3 different recirculation regimes, namely 1 linac up/1 linac down, 1-pass up/1-pass down starting with reduced energy (400∼500 MeV/linac), and eventually 5-pass up/5-pass down, to be concluded with completion of ER at 7 GeV.

The project has been submitted to, and has received approval from, JLab Program Advisory Committee (PAC 44) in July 2016 [1]. A next major objective in demonstrating readiness is a technical review as mandated by PAC 44.

REFERENCES

[1] S.A. Bogacz et al., ER@CEBAF: A Test of 5-Pass Energy Recovery at CEBAF, JLab Tech. Note, June 6, 2016, eRHIC Tech. Note 54, BNL, June 2016.

STUDIES OF CSR AND MICROBUNCHING AT THE JEFFERSON LABORATORY ERLS*

C. Tennant[†], S. Benson, D. Douglas, R. Li
Thomas Jefferson National Accelerator Facility, Newport News, VA 23606, USA
C.-Y. Tsai
SLAC National Accelerator Laboratory, Menlo Park, CA 94025, USA

Abstract

One attractive feature of energy recovery linacs (ERLs) is they are source limited. However as beam brightness increases so too do the effects of coherent synchrotron radiation (CSR) and the microbunching instability. The Low Energy Recirculator Facility at Jefferson Laboratory provides a test bed to characterize aspects of CSR's effect on the beam by measuring the energy extraction via CSR as a function of bunch compression. Data was recorded with acceleration occurring on the rising part of the RF waveform while the full compression point was moved along the backleg of the machine and the response of the beam measured. Acceleration was moved to the falling part of the RF waveform and the experiment repeated. Initial start-to-end simulations using a 1D CSR model show good agreement with measurements. The experiment motivated the design of a modified Continuous Electron Beam Accelerator Facility-style arc with control of CSR and the microbunching gain. Insights gained from that study informed designs for recirculation arcs in an ERL-driven electron cooler for Jefferson Laboratory's Electron Ion Collider. Progress on the design and outstanding challenges of the cooler are discussed.

INTRODUCTION

Coherent synchrotron radiation (CSR) poses a significant challenge for accelerators utilizing high brightness beams. When a bunch travels along a curved orbit, fields radiated from the tail of the bunch can overtake and interact with the head. Rather than the more conventional class of head-tail instabilities where the tail is affected by the actions of the head, CSR is a tail-head instability. The net result is that the tail loses energy while the head gains energy leading to an undesirable redistribution of particles in the bunch. Because the interaction takes place in a region of dispersion, the energy redistribution is correlated with the transverse positions in the bend plane and can lead to projected emittance growth. The following section describes experiments at the Low Energy Recirculator Facility (LERF, formerly the Jefferson Laboratory FEL [1]) to quantify these bulk effects on the bunch distribution. However, in addition to the potential for emittance and energy spread growth, CSR can also drive the microbunching instability. This aspect is

addressed later in the context of the Jefferson Laboratory Electron-Ion Collider (JLEIC).

MEASURED EFFECT OF CSR

Studies at the LERF (see Fig. 1) focused on characterizing the impact of CSR with the goal of benchmarking measurements with simulation . The LERF was designed as an energy recovery based linear accelerator used to condition an electron beam for high average power lasing. Electrons are generated in a DC photocathode gun (135 pC), accelerated to 9 MeV and injected into the linac where they are further accelerated up to 130 MeV through three cryomodules. Acceleration nominally occurs 10° ahead of the crest of the RF waveform, to impart a phase-energy correlation across the bunch. The first- and second-order momentum compactions of the first Bates-style recirculation arc are set so that, in conjunction with the downstream chicane, the bunch is rotated upright at the wiggler and phase space curvature is eliminated. Following the wiggler, the longitudinal phase space must be rotated back by 90° to energy compress the beam as it arrives at the dump. The experimental program consisted of characterizing the effects of CSR for two different longitudinal matches: accelerating on the rising (falling) side of RF waveform together with a negative (positive) momentum compaction – from the combined arc and chicane system – for compression.

Accelerating 10° Before Crest

Measurements were made to quantify the effect of parasitic compressions (i.e. when the bunch goes through a full compression) on beam quality through linac-to-wiggler transport. With the nominal energy chirp the beam experiences three such parasitic compressions. Quadrupole scans to measure emittance and Twiss parameters were performed at several locations around the machine and repeated with the linac cross-phased. Cross-phasing refers to switching the accelerating phase of only the middle cryomodule (which has the same gradient as the two outboard cryomodules combined) to the falling side of the RF waveform. Upon exiting the linac the energy chirp is removed and the nearly mono-energetic distribution avoids parasitic compressions. Results of the measurements are summarized in Table 1. The small horizontal emittance growth through the machine for cross-phased measurements is not unexpected, while the effect of parasitic compressions is more dramatic. These measurements together with simulations suggest that while parasitic compressions do not lead to copious CSR-
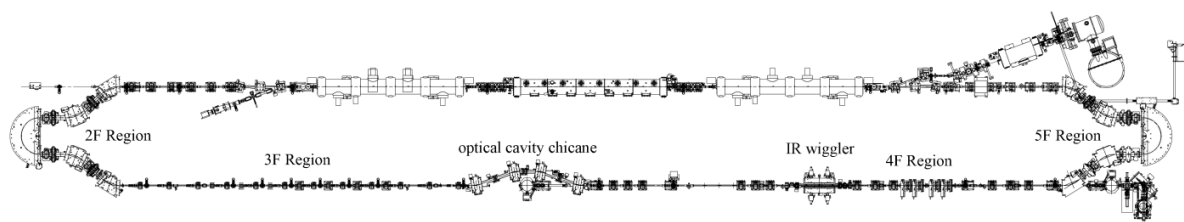
Figure 1: Schematic of the LERF (formerly FEL) without the UV bypass line.

induced energy loss, they do significantly degrade emittance in the bending plane. Simulations using elegant's ultra-relativistic 1D CSR model were unable to generate the observed emittance growth [2]. It is known that the transverse extent of the bunch through the Bates bend violates the so-called "Derbenev criterion" [3] under which the 1D approximation is valid. This, along with the absence of space charge modeling through the arc, may account for the discrepancy.

Table 1: Normalized horizontal emittance and Twiss parameters at various locations in the machine. (0F corresponds to the injector, 2F to the exit of linac, 3F to the exit of first arc and 4F to the exit of the chicane).

	Cross-Phased			Nominal		
	ε_x (mm-mrad)	β_x (m)	α_x	ε_x (mm-mrad)	β_x (m)	α_x
0F	15.2	11.2	−0.1	15.2	11.2	−0.1
2F	17.5	11.8	6.3	17.9	12.9	6.6
3F	20.8	3.7	−1.0	30.5	3.1	−0.7
4F	21.3	11.8	−5.5	41.8	16.8	−8.0

Accelerating 10° After Crest

Nominally the R_{56} and T_{566} in the Bates bend are selected (using trim quadrupoles and sextupoles) such that (after traversing a downstream chicane), the bunch is rotated upright at the wiggler. However, it is possible to vary the trim quadrupoles to produce a range of arc linear momentum compactions from −0.5 m to +1.0 m. After moving the acceleration to the falling side of the RF waveform, data was recorded of the energy extracted via CSR (measuring BPMs in the dispersive region in the π-bend of the second Bates bend) as function of bunch compression. This is illustrated in Fig. 2. Most energy is extracted when full compression occurs at the optical cavity chicane (left dip) rather than at the end of the arc (right dip). While the R_{56} was varied in the arc, T_{566} was fixed such that the native T_{566} of the chicane corrects the curvature, generating high peak current and exacerbating the effects of CSR [4].

In addition to measuring the CSR-induced energy loss, images from a synchrotron radiation monitor were recorded to capture details of the bunch momentum distribution while the compression state was varied (the synchrotron light monitor is located at a dispersive location where the horizontal beta function is small, effectively mapping the momentum distribution onto the horizontal

axis of the viewer). An animation of the beam response to variable compression is available at [5]. Preliminary start-to-end simulation results show good agreement with measurement, even to the point of replicating observed filamentation on the momentum distribution (see Fig. 3).
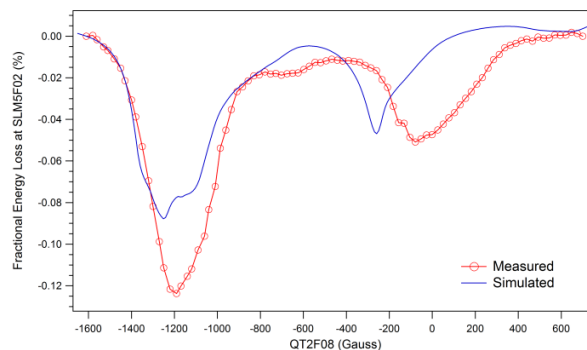
Figure 2: Measured and simulated CSR-induced energy loss as a function of compression state after acceleration on the falling part of the RF waveform.
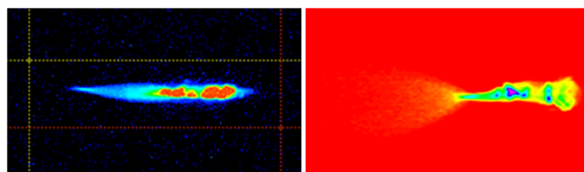
Figure 3: Observed beam momentum distribution modulation (left) compared with simulated results (right).

Figure 4 illustrates changes to the momentum distribution as measured in the second arc (projections plotted along momentum axis) as a function of the compression state (characterized by the strength of one of the quadrupoles varied in the first Bates bend). Two distinct troughs running through the surface plot are clearly discerned. As previously noted, a curved bunch in longitudinal phase space (e.g. when second-order compactions are not properly set) will limit the minimum compressed bunch length and generate one or more localized current spikes. It has been shown that a local concentration of charge can produce stronger CSR wakes than compared to a Gaussian distribution of the same rms length [6]. The strong CSR wake and its effect – namely the redistribution of energy within the distribution – is localized to the region of the current spike which itself moves temporally through the bunch as the compression

WEIBCC004

state is changed. Note that the regions of depletion correspond to the measured maximum energy loss (compare to Fig. 2).
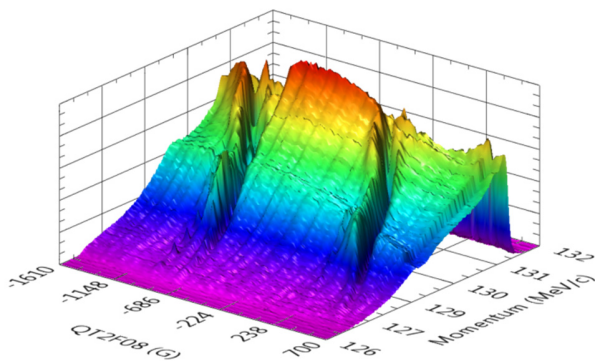
Figure 4: Surface plot illustrating the effects of CSR on the momentum distribution as a function of compression state.

LASING WITH $R_{56} > 0$ COMPRESSION

The FEL itself serves as the best available beam diagnostic. Leveraging the flexibility of the LERF to completely change the longitudinal match, a test was performed of lasing with compression using a positive R_{56} from the linac-to-wiggler transport. Acceleration occurred on the falling side of the RF waveform and signs of the compactions were switched. Lasing was challenged by fact that wiggler gap control firmware was unavailable, keeping the wavelength "stuck" at value for which optical cavity mirrors performed poorly (over 50% losses). Additionally, the "high" reflector had higher transmission than the outcoupler requiring greater than 200% gain just to lase. Despite these issues, the system lased extremely well. After optimization the wavelength was 762 nm with a (10-11) μm detuning curve and a (9.5-10) μs turn-on time – both typical values for the nominally configured system. This proof-of-principle lasing demonstration has important implications for bunch compression, namely:

1) Positive compaction is the natural result of bending and is readily achieved in simple beamline configurations (e.g. a FODO arc) supporting simple and effective schemes for aberration compensation, rendering harmonic RF unnecessary.
2) Longitudinal space charge (LSC)-induced phase space distortion, on the falling side of the RF waveform, increases the phase-energy correlation on the beam. Thus, LSC enhances the chirp, rather than suppressing it (as occurs on the rising side of the RF waveform), where the suppression can result in a potentially incompressible region of phase space.
3) Compressors can be configured – when running with positive compaction – to avoid any spurious over-compression; the final compression occurs in the back end of the final compressor dipole.

The idea of using a compressor arc leads one to contemplate recirculated linac driven light sources. The cost saving benefits of recirculating linacs is well known [7], but concerns about beam degradation, especially due to CSR, through 360° of bending presents a challenge. Progress on an emittance preserving, low microbunching instability (μBI) gain, isochronous arc is discussed below.

EMITTANCE PRESERVING ARC

We apply the compensation analysis of Ref. [8] – as previously used by Borland [9] – to the design of transport systems for use with low emittance beams, and find that appropriately configured second order achromats will suppress transverse emittance growth due to CSR [10]. A second-order achromat composed of superperiods that are individually linearly achromatic and isochronous meet all the requirements for the suppression of CSR effects. In this case, any CSR-induced momentum shift will be paired to a matching shift at a downstream location with the same lattice parameters and the same bunch length. The transverse phase space configuration is "inverted" by the (modulo) half-betatron wavelength phase separation. The impact of the second transverse momentum shift therefore completely cancels (to linear order) that of the first. One such design is for a 1.3 GeV arc based on a modified CEBAF design. Simulation of transport with CSR was performed with elegant. For an initial transverse normalized emittance of 0.25 mm-mrad and assuming an initially upright bunch of length of 3.0 ps and momentum spread 11.7 keV, the emittance is well-preserved over a broad range of bunch charges and initial (rms) bunch lengths. As the beam brightness increases, it is not only the bulk effects of CSR on the bunch, but also the CSR-driven microbunching that must be managed. An unanticipated outcome of the exercise, and of considerable interest, is the additional observation that these beam line designs also manifest little or no evidence of microbunching. In the modified CEBAF arc example, though wake distortion is evident on the longitudinal distributions, there is no visible microbunching until the bunch charge approaches 1.0 nC. Analysis shows micro-bunching gains of less than unity across a range of modulation wavelengths (see Fig. 5) [11].
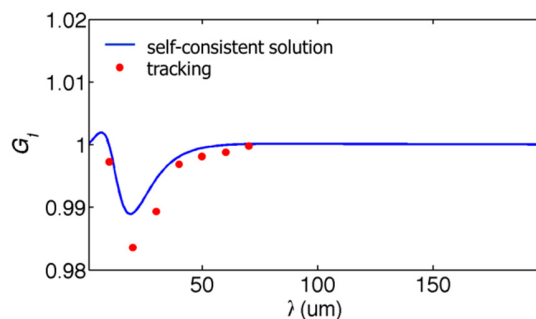
Figure 5: Microbunching gain spectrum as a function of modulation wavelength.
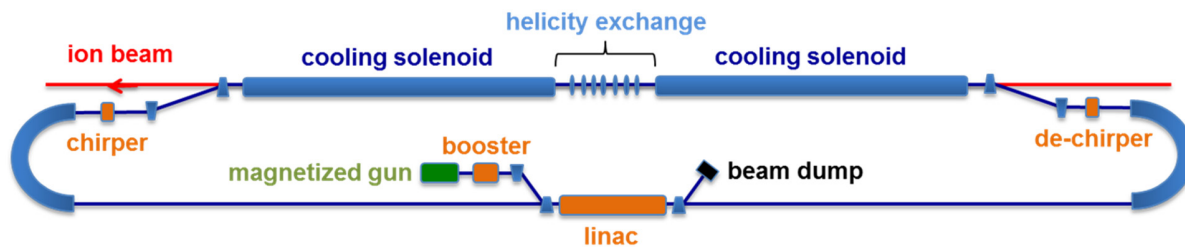
Figure 6: Schematic of the single pass ERL-driven electron cooler for JLEIC.

MICROBUNCHING

The mechanism by which microbunching develops is as follows: an initial density modulation, either from shot noise or from the drive laser, is converted to energy modulations through short-range wakefields such as space charge and CSR. The energy modulations are then transformed back to density modulations through the momentum compaction of the lattice. Danger arises when a positive feedback is formed and the initial modulations are enhanced. This phenomenon has been studied extensively, both theoretically and experimentally, in bunch compressor chicanes [12]. Only recently has there been a concerted effort to study the microbunching instability in recirculating arcs [13]. Energy recovery linacs can be particularly susceptible to microbunching. For increased efficiency, ERLs inject beam at low energy and the beam is influenced by space charge forces. Due to the topology required in same-cell energy recovery, ERLs necessarily have substantial bending and are subject to the effects of CSR. And – unlike space charge – the effects of CSR do not diminish at high energy. Because the beam is subject to space charge and/or CSR throughout the machine, density modulations can be converted to energy modulations. And because of the native momentum compaction of the lattice (in arcs, spreaders/recombiners, chicanes, etc.) those energy modulations may be converted back to density modulations. Therefore, for ERLs using high brightness beams, conditions are quite favorable for seeding the microbunching instability.

Studying the microbunching instability in the time-domain (i.e. via particle tracking) presents multiple challenges. The initial density modulation needs to be small enough to remain in the linear regime but large enough to overcome numerical artifacts which requires a large number of particles. Due to the computational burden, it becomes difficult to exercise parametric studies and/or model an entire accelerator complex. On the other hand, a semi-analytical Vlasov solver that works in the frequency-domain and models relevant collective effects such as LSC, CSR and linac geometric effects using analytic impedance expressions has led to insights on lattice constraints for control of the microbunching instability [14]. The development of a fast Vlasov-solver has been an invaluable asset in the design and development of arc lattices.

JLEIC

The U.S. Nuclear Science Advisory Committee has made an electron-ion collider the priority as the next generation of accelerator to serve the nuclear physics community. Jefferson Laboratory's contribution to this effort has been the design of JLEIC, a design over 10 years in the making, which involves colliding polarized electrons (originating from CEBAF) with medium energy ions that would originate in a new ion complex [15]. A ring-ring collider scenario has been chosen as the baseline, with figure-8 shape rings for achieving and preserving the high ion polarization. Calculations indicate that a very high luminosity (over 10^{-34} $cm^{-2}s^{-1}$) is possible with the present design concept. However, in order to achieve that ambitious luminosity, several stages of electron beam cooling must be employed. The most challenging is the high energy, bunched beam cooler designed to cool 100 GeV protons. The cooler requires handling a low energy, high power electron beam – which is not unlike a free-electron laser. The primary difference is that an FEL requires a very short (high current) bunch at the interaction region (undulator), whereas the cooler requires a very long, low energy spread bunch at the interaction region (cooling solenoid). Both a strong cooling (baseline) and weak cooling scheme (backup) are being designed. In the following sections, the impact of CSR and microbunching for each are discussed.

Weak Cooling

The weak cooling option is based on an energy recovery linac conditioning a 55 MeV magnetized beam (420 pC/bunch) for a single pass through a long cooling channel (co-propagating with the proton beam) before the beam energy is recovered. A schematic of the machine is shown in Fig. 6. Effective cooling requires preserving the transverse emittance and meeting the energy spread specification of 3×10^{-4} (rms). The recirculation arcs are comprised of index-½ dipoles to maintain axial symmetry and preserve the magnetization. The arc is tuned to have a R_{56} of +0.55 m so as to debunch the beam and lengthen it from 20 ps (full) to 67 ps (full). The computer code TStep was used to model space charge and CSR in the arc and its effect on the beam. Results show a 2% growth in the transverse emittance. The wake-induced distortions along the bunch are modest and should present no challenges in achieving the required energy spread at the cooling

channel. Recent efforts have studied the effect of transporting a magnetized beam on the microbunching gain [16]. It turns out that the relatively large transverse size (on the order of millimeters) produces a smearing effect, analogous to Landau damping when the energy spread is large, which effectively damps the instability. Using the fast Vlasov-solver we can quickly estimate the microbunching gain curve. We note that the Vlasov solver has been extensively benchmarked with the more computationally intensive and tedious particle tracking in elegant. The result shows that the microbunching instability is well controlled over a large range of incoming intrinsic energy spreads; it is damped by the arc (gain < 1) when $\delta p/p = 2.4 \times 10^{-3}$ and is near unity for $\delta p/p = 8 \times 10^{-5}$.

Strong Cooling

Rather than the single pass ERL, the new baseline is a circulator cooling ring (CCR) driven by an ERL. The idea is that an ERL, conceptually similar to the one designed for weak cooling, accelerates 2 to 3.2 nC bunches to 55 MeV/c. After the first arc, the cooling channel is replaced by a beam exchanger where the bunch is kicked upward into a CCR. The bunch will make 10 to 20 turns in the CCR wherein it will pass through a cooling channel on every revolution. A kicker [17] then directs the beam back down to the ERL where the bunch is energy recovered. As in the weak cooling design, the bunch delivered to the cooling channel must be long (with a flattop distribution of full length 2 cm) and of small relative momentum spread (3×10^{-4} rms). In addition to preserving the beam quality through the first arc of the ERL and the beam exchange region, one of the biggest challenges is maintaining a sufficiently small energy spread while the bunch is subjected to the CSR wake over the course of 20 turns in the CCR. While methods to mitigate the transverse emittance growth have already been explored, the energy loss and gross distortion along the bunch from the CSR wake are not easily reversed. The CSR wake is proportional to the bunch distribution. For a flattop the effect of the wake is impart a fairly linear slope across the bunch. Simulations using an RF cavity run near zero-crossing to both remove the slope and restore the energy loss from CSR have been moderately successful (see Fig. 7). Estimates suggest that CSR shielding can be effective and will be explored as arc designs mature.
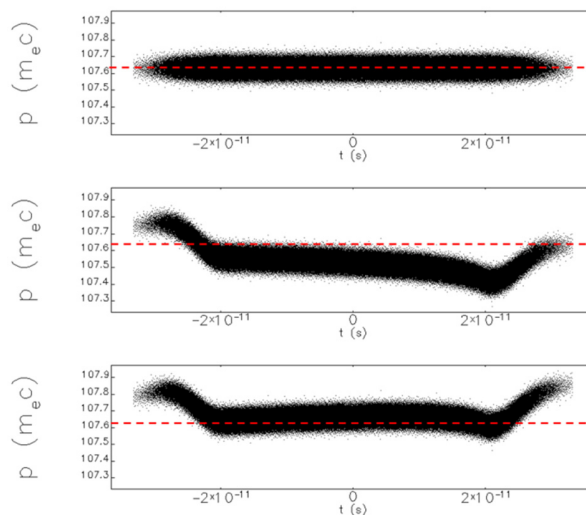
Figure 7: Initial longitudinal phase space (top) and after one turn in the CCR with CSR without correction (middle) and with correction via an RF cavity (bottom).

SUMMARY

In Jefferson Laboratory's three ERL-driven FELs (IR Demo, IR Upgrade, UV) CSR has been present though has never as an operational impediment. As we look toward the future and consider an ERL-driven cooler with higher bunch charges, CSR as well as the microbunching instability become challenges to be addressed in the design of arcs. This leads to an important point, namely that we are approaching the limits of what currently available simulation codes can handle. We are entering a low energy, high charge region of parameter space where both space charge and CSR are important. Furthermore, initial studies have shown that the ability to simulate the effect of CSR shielding is going to be a high priority.

REFERENCES

[1] C. Tennant, Proc. PAC'09, pp. 3125-3129 (2009).

[2] M. Borland, Advanced Photon Source LS-287 (2000).

[3] Y.S. Derbenev et al., TESLA FEL Report 1995-05 (1995).

[4] C. Hall et al., Phys. Rev. ST Accel. Beams **18**, 030706 (2015).

[5] https://goo.gl/KoIcpu

[6] R. Li, NIM-A, **475** 498-503 (2001).

[7] R. York, PRST-AB **17**, 010705 (2014).

[8] S. DiMitri et al., Phys. Rev. Lett. **110**, 014801 (2013).

[9] M. Borland et al., Proc. AccApp'07, pp. 196-203 (2007).

[10] D. Douglas et al., arXiv:1403.2318 (2014).

[11] C.-Y. Tsai et al., Proc. 36th FEL Conference, pp. 730-734 (2014).

[12] S. Heifets et al., Phys. Rev. ST Accel. Beams **5**, 064401 (2002).
     Z. Huang and K.-J. Kim, Phys. Rev. ST Accel. Beams **5**, 074401 (2002).

[13] S. DiMitri and M. Cornacchia, EPL, **109** 62002 (2015).
C.-Y. Tsai et al., Phys. Rev. Accel. Beams **19**, 114401 (2016).
C.-Y. Tsai et al., Phys. Rev. Accel. Beams **20**, 024401 (2017).

[14] C.-Y. Tsai et al., Phys. Rev. Accel. Beams **20**, 024401 (2017).

[15] S. Abeyratne et al., arXiv:1504.07961 (2015).

[16] C.-Y. Tsai et al., Phys. Rev. Accel. Beams **20**, 054401 (2017).

[17] Y. Huang et al., Phys. Rev. Accel. Beams **19**, 122001 (2016).

WEIBCC004

FIRST RESULTS OF COMMISSIONING DC PHOTO-GUN FOR RHIC LOW ENERGY ELECTRON COOLER (LEReC)*

D. Kayran†, Z. Altinbas, D. Bruno, M. Costanzo, A. V. Fedotov, D. M. Gassner, Xiaofeng Gu,
L. R. Hammons, P. Inacker, J. Jamilkowski, J. Kewisch, C.J. Liaw, C. Liu, K. Mernick,
T. A. Miller, M. Minty, V. Ptitsyn, T. Rao, J. Sandberg, S. Seletskiy, P. Thieberger, J. Tuozzolo,
Erdong Wang, Zhi Zhao, Brookhaven National Laboratory, Upton, NY 11973, US

Abstract

Non-magnetized bunched electron cooling of ion beams during low energy RHIC operation requires electron beam energy in the range of 1.6-2.6 MeV, with an average current up to 45 mA, very small energy spread, and low emittance [1]. A 400 kV DC gun equipped with a photocathode and laser system will provide a source of high-quality electron beams. During DC gun test critical elements of LEReC such as laser beam system, cathode exchange system, cathode QE lifetime, DC gun stability, beam instrumentation, the high-power beam dump system, machine protection system and controls has been tested under near- operational conditions [2]. We present the status, experimental results and experience learned during the LEReC DC gun beam testing.

INTRODUCTION

The LEReC uses a replica of the DC photocathode gun used in the Cornell University prototype injector, which has already been producing record high-brightness, high average current electron beams [3]. The gun has been built by Cornell University. DC Gun is required to operate with more than 30 mA 24/7. Gun will use multi-alkali NaK2Sb (or CsK2Sb) photocathode, which will be illuminated with green (532 nm) laser light with an oscillator frequency of 704 MHz. We expect that lifetime of such cathodes should be 10s hours. In order to optimized operation time and minimized the cathode exchange time multi cathodes carrier has been built. It's

designed to hold up to 12 pucks of photocathodes attached to the gun in 11 scale vacuum [4]. The 400 keV electron beam from the gun is transported via a 704 MHz SRF booster cavity and 2.1 GHz 3rd harmonic linearizer normal conductive cavity. Electron beam is accelerated to maximum kinetic energy of 2.6 MeV. In drift space electron bunch is stretched to required bunch length. Before entering the cooling section accumulated energy chirp is compensated by normal conductive 704 MHz cavity. Two dogleg-like mergers and mirror dipole are used to combine and to separate electron cooler electron beam with/from RHIC ion beams. The layout of LEReC is shown in Fig. 1. The optics of entire transport line has been designed and optimized to delivery electron bunches for different operation energies with quality satisfied electron cooling requirement summarized in Table 1 [5].

Table 1: LEReC electron beam requirements

Kinetic energy, MeV	1.6	2.0	2.6
Bunch Charge, pC	130	160	200
Bunches per train	30	27	24
Macro bunch charge, nC	3.9	4.3	4.8
Macro bunch rep. f, MHz	9.3	9.3	9.3
Total beam Current, mA	36	40	45
Normalized Emittance, µm	< 2.5	< 2.5	< 2.5
Energy spread, 10^{-4}	< 5	< 5	< 5

Figure 1: Layout of LEReC accelerator. Red contour box indicates DC gun test area.
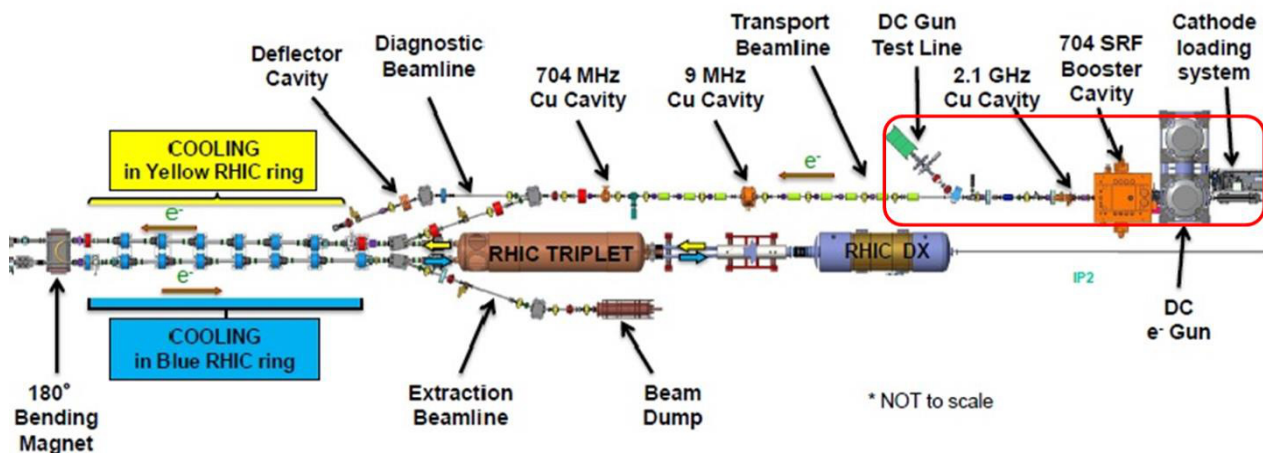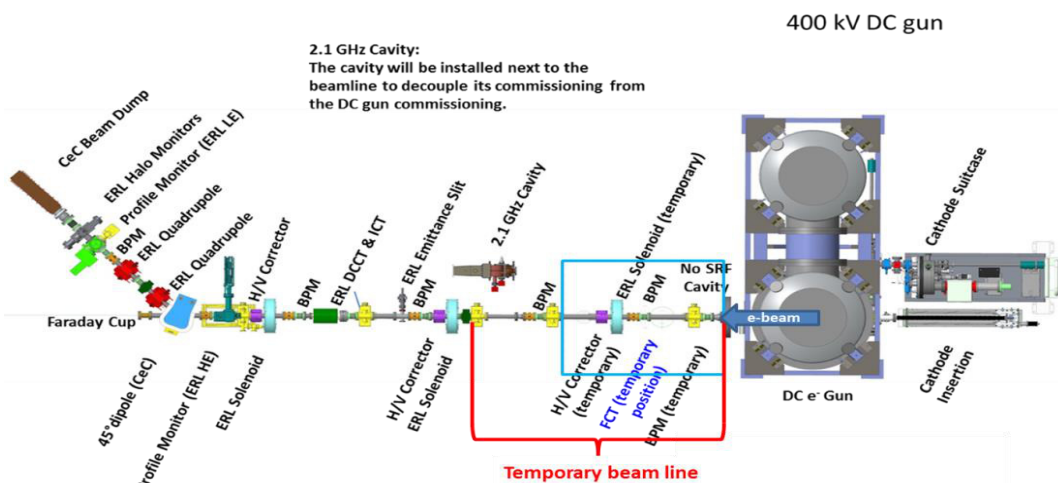
Figure 2: LEReC DC gun beam test layout. 2.1 GHz 3rd harmonic cavity (testing aside of DC gun test beam line) and 704MHz SRF cavities (shown as a blue box contour) will be installed in replacement of temporary beam line after gun test is finished in fall of 2017.

Many beam line components are transferred from R&D ERL test facility [6] SRF cavity, solenoids, quadrupoles, magnets power supplies, beam profile monitors, beam position monitors, DCCTs, ICT and from CEC POP test [7] 45 degrees dipole, 10 kW beam dump.

PURPOSE OF LEReC GUN TEST

The gun beam test (see Fig. 2) is the first stage of LEReC commissioning. Our aim is to test critical LEReC equipment in close to operation condition. This will demonstrate that the DC gun with photocathode meets its performance specifications and can work reliably.
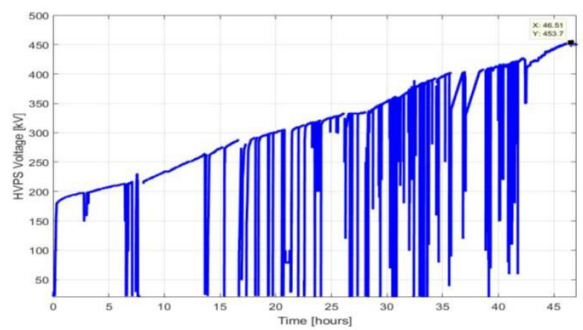
Figure 3: Voltage change during LEReC DC gun conditioning process at BNL.

Components to be tested during gun commissioning: a) laser beam delivery system (laser, laser shaping, laser transport, laser pulse stability); b) vacuum components; c) cathode manipulation system; d) DC gun characterization (stability, maximum operation voltage, electron beam quality); e) magnets (power supply); f) beam instrumentation; g) Control system (timing system, machine protection system, control of laser, gun power supply etc.); h) high average power beam extraction and dump system. Gun test is designed to measure: a) beam

energy and energy spread; b) emittance (ε) and Twiss parameters (α, β) using solenoid scan and/or slits; c) Longitudinal and transverse halo. During later runs with booster cavity installed we should be able to measure: bunch length and slice emittance.
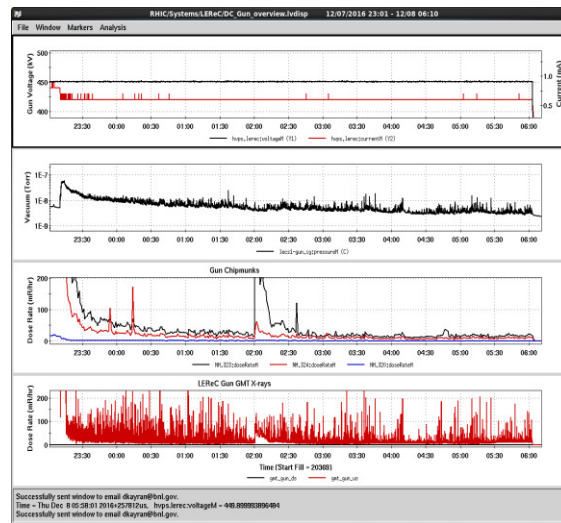
Figure 4: DC Gun stable operation during 7 hours at 450 kV after HV conditioning. (Top plot HV PS voltage and current. Second plot SHOWS in gun vacuum improvement from initial 1E-8 to 3E-9.

HV DC GUN CONDITIONING

First time gun has been conditioned at Cornell University in October 2016 gun reached 440 kV. After that gun has been dissembled and sent to Brookhaven National Lab (BNL). Where it was assembled and installed in final location. In November 2016 after 46 hours of conditioning the gun successfully reached 450 kV (see Fig. 3). Gun demonstrated stable operation at 450

kV during 7 hours with very little radiation (see Fig 4.) The two bottom plots show radiation measured by different instruments, radiation level stays at 10-20 mR/hr).

FIRST PHOTOCURRENT FROM DC GUN

The gun to booster beam line includes two solenoids, H/V correctors, laser insertion and extraction ports, beam profile monitor (PM), and two beam position monitors (BPM) (see Fig. 5).

Temporary line presented at Fig. 2, consists of: ERL type solenoid, H/V corrector, beam position monitors (BPMs), fast current transformer (FCT).

Rest of the DC gun test transport line consists of: two ERL solenoids, two H/V correctors, three BPMs, integrated current transformer (ICT), direct current transformer (DCCT), multi-slits, and PM. Straight ahead line is terminated by Faraday cup (FC) at the end. This line is used for current control and transverse emittance measurements (for LEReC beam instrumentation details see [8, 9]).
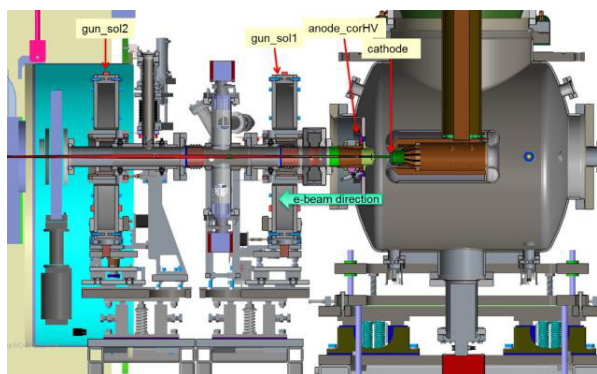
Figure 5: LEReC gun area side view.

1st cathode surface has been scratched during transportation from cathode deposition system to the gun (see Fig. 6). Initial without high power pulsed laser these clear straight lines helped to check first two solenoids calibration using photoelectrons generated by cathode illumination LED lamp. Lines rotation angle: $\varphi = \int Bz(z)dz/2B\rho$, where $Bz(z)$-longitudinal solenoid field, $B\rho$ – beam rigidity (see Fig. 7). As a result for different current we confirmed gun energy and solenoid field integral calibration.
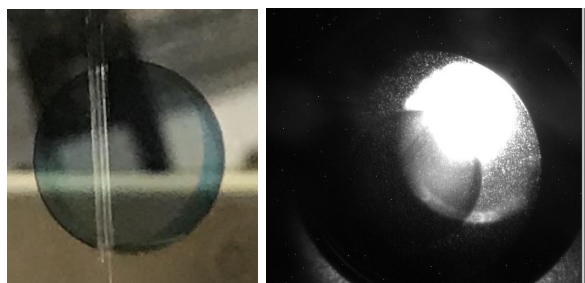
Figure 6: First cathode with scratch marks used in the DC gun test: (left) before installation, (right) cathode installed in the gun.
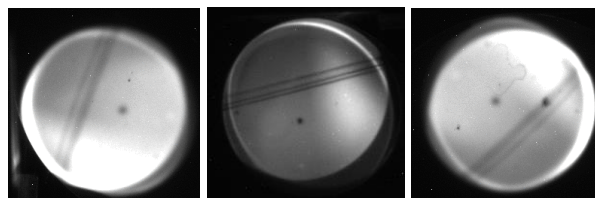
Figure 7: Beam images (DC "lamp current") are taken at YaG beam profile monitor for three different solenoid current settings.

Results of all three cathodes tested during DC gun test are summarized in Table 2 (for more details about LEReC cathodes see [10]).

Table 2: LEReC cathodes operations summary

	Cath #1	Cath #2b	Cath #3
Operation dates	Apr 17-June 2	June 2 – June 14	June 16-current
Lamp DC	40 nA	40 nA	150 nA
Max. charge	25 pC	33 pC	130 pC
In Lab QE	1.7%	7%	4%
In Gun QE	0.1%	0.3%	1.2%

Lamp DC beam produced by illumination of LED flash light has been used for initial commissioning and beam based calibration of faraday cups, halo scrapers and profile monitors. Rest of the beam instrumentation required bunched beam.

BEAM DUMP LINE

Beam dump extraction line consists of 45-degrees chevron dipole, two ERL quadrupoles with trims (one horizontal, one vertical correction), BPM, PM, 2D halo monitor, and fast current transformer (FCT). Inclined beam line is terminated by 10 kW beam dump that also serves as a Faraday cup. The inclined line will be used for beam energy and energy spread measurements, transverse and longitudinal halo studies.

The beam dump is cooled from top and bottom by water circulation. The sides are cooled only by copper thermo-conductivity. For optimum cooling, the electron beam will be spread more in the vertical direction. The beam profile monitor is used to match the electron beam with the aperture of the beam dump. At high beam current BPMs provide an interlock if the beam trajectory is out of a predefined range of offsets (for LEReC machine protection system details see [11]). A second protection method uses four sets of slightly inserted halo monitors. These monitors measure very small current deposition on any of the four beam dump jaws in order to detect any beam profile changes.

BUNCHED BEAM OPERATION

LEReC operation required to chop 704 MHz laser pulses into macro bunches with 106 nsec apart. Operation with macro bunches from single to few hundreds has been tested (see Fig. 8 and Fig. 9).
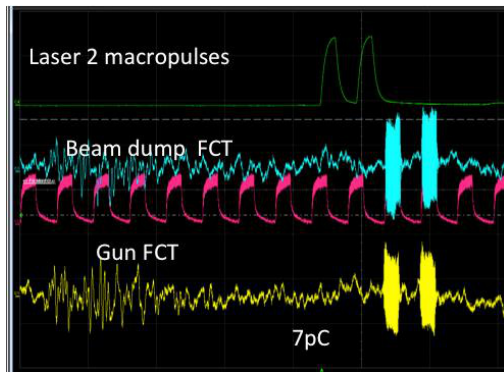
Figure 8: First pulsed beam observed during 2 macro bunch operations. Charged per bunch measured 7 pC by gun FCT (cyan) and beam dump FCT (yellow).

Figure 9: Charge per bunch reached minimum LEReC design requirement 120 pC. Cyan trace is beam dump faraday signal 4 macro bunches 30 bunches each.

As expected for train of several hundreds of macro bunches gun voltage dropped due to beam loading which has been clearly observed at beam dump line BPM and FCT signals. This is a result of large time constant of currently installed 100 MOhm processing resistor and estimated cathode capacitance of 75 pF (time constant 7.5 msec). 1 nC charge per macro bunch leads to gun voltage dropped by 13 V.

For 500 macro bunches train DC gun voltage and as result energy of the last macro bunch drops by 6.7 keV. On Fig. 10 it's shown how average bunch position moved in dispersive section when numbers of macro bunches increase.

Beam loss increases in beam dump line (see Fig. 11). Currently gun beam loading prevents us to run more total charge per second.

After replacing processing resistor to regular one with resistance of 400 Ohm and corresponding time constant of 30 nsec we expect that the effect of accumulated beam loading will be diminished.

BEAM LINE MAGNETIC SHIELDING

The energy of the electrons leaving the gun is ~400 keV. In tunnel measured residual field is in order of 0.5 Gauss (Earth's magnetic field) in 1 m will bend the beam to 20 mrad. The beam shift could be on the order of 1 cm. After 2 m of drift space, the beam would be lost on the minimum aperture of the vacuum chamber. On the

bench test confirmed that 3 layers of 9 mils of μ-metal foil wrapped around the vacuum chamber diameter of 7.5 cm sufficient to reduce field more than 50 times (see Fig. 12). The same magnetic shielding has been installed everywhere at any open areas along DC gun beam line.
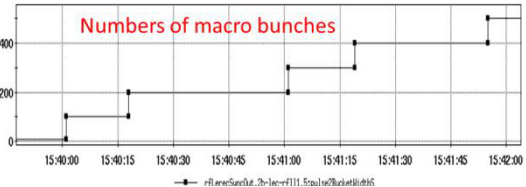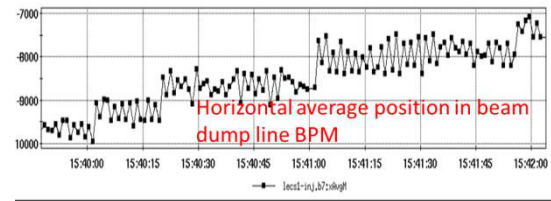
Figure 10: 100-500 macro bunches operation with 1 nC per macro bunch: (top) horizontal beam position in dispersive beam dump line, (bottom) numbers of macro bunches.
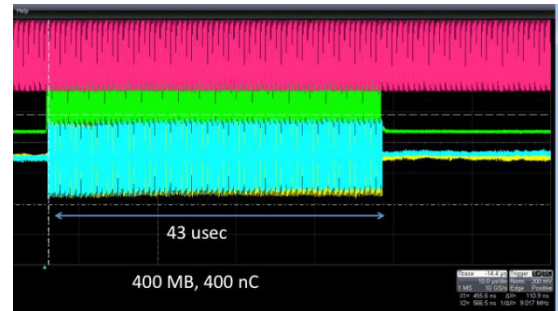
Figure 11: Gun FCT signal (yellow) and beam dump FCT signal (cyan) during 400 Macro bunches operation.
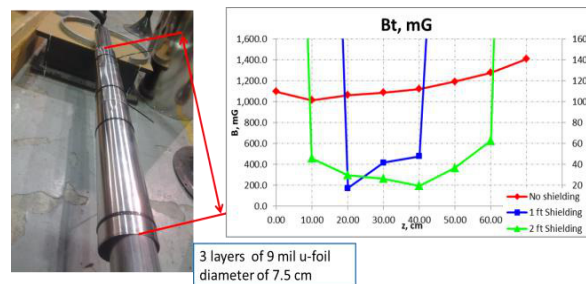
Figure 12: Transport line magnetic shielding test on the bench (left). Measured magnetic field (right). Without shielding 1.2-1.4 Gauss (left scale) with shielding 20-40 mGauss (right scale).

BEAM CURRENT RAMP UP

Space charge effect plays significant role to beam dynamics at low energy. In order to increase average current preferable scenario is to keep charge per bunch constant while increasing numbers of macro-bunches. Currently our laser bunch structure control system is

capable to provide continuous increase numbers of macro-bunches up to 50 msec train duration. Work has been started to develop and test system which is capable to increase numbers of macro bunches from 1 to CW. Such system is required for LEReC commissioning which scheduled to start in spring of 2018.
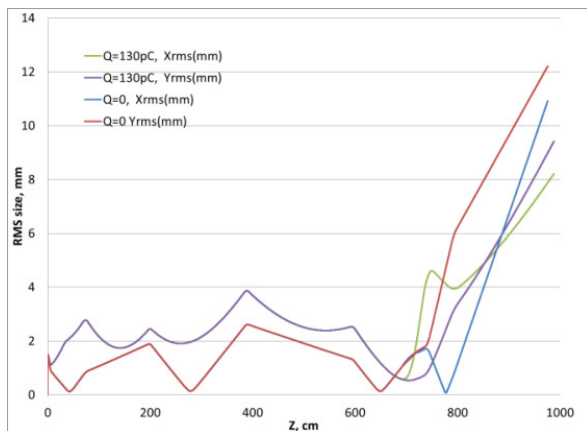
Figure 13: RMS beam envelope in the gun test beam line for nominal charge of 130 pC and very small charge of 0.13 pC.

Alternative could be increasing charge per bunch while keep pulse pattern untouched. As a results beam envelope will vary with space charge. For example on Fig. 13 we show RMS envelopes from gun to dump as a result of PARMELA [12] simulation with nominal charge per bunch and with significant low charge per bunch. Due to simplicity of the beam line and relatively weak optics in both cases beam reaches the beam dump while RMS transvers size stays below 4 mm in transport line. The slow increasing laser power seems to be good alternative to ramp up current during DC gun test.

Table 3: LEReC DC Gun beam test parameters

Parameter	Required	Achieved
Gun voltage , kV	400	400
Bunch charge, pC	130-200	0-130
Laser max frequency, MHz	704	704
Laser pulse duration, psec	80	80
Macro-bunch charge, nC	3-5	3.9
Macro-bunch rep. rate, MHz	9.3	9.3
Macro bunches per sec	CW	1400
Normalized emittance, µm	1-1.5	0.2-4*
Maximum average power, kW	10	0.0004

*) Preliminary results.

SUMMARY AND PLANS

To reduce risk and time required for LEReC systems commissioning we start testing the DC gun photo injector during RHIC Run 17.

Gun test is designed to provide initial studies of DC gun performance and test key concepts for LEReC

commissioning: MPS operation, cathode delivery system, laser system, high average current capability etc.

The beam line optics is flexible enough to accommodate running gun with different charges required for final stage of LEReC operation.

Bunch with designed beam kinetic energy of 400keV and charges of 0-130 pC has been successfully delivered to the 10 kW beam dump. Measured beam parameters during gun test are summarized in Table 3.

Beam instrumentation has been tested and cross calibrated.

Maximum numbers of pulses has been limited by beam loaded voltage drop due to very long current replenishment constant. After replacing processing resistor in July 2017 we will continue increasing numbers of macro bunches and study CW operation of the HV DC gun photo injector.

REFERENCES

[1] A. Fedotov, "Bunched beam electron cooling for Low Energy RHIC operation", ICFA Beam Dynamics letter, No. 65, p. 22, December 2014.

[2] D. Kayran et al., "DC Photogun Gun Test for RHIC Low Energy Electron Cooler (LEReC)", in Proc of NAPAC2016, p. 1008-1011, 2016.

[3] B. Dunham et al., "Record high-average current from a high-brightness photoinjector", Appl. Phys. Lett., vol. 102,p . 034105, 2013.

[4] C.J. Liaw et al., "Cathode puck insertion system design for the LEReC photoemission DC electron gun", in Proc of NAPAC2016, p. 1021-1023, 2016.

[5] J. Kewisch et al., "Beam optics for the RHIC Low Energy electron Cooler (LEReC)", in Proc of NAPAC2016, p. 1015-1017, 2016.

[6] D. Kayran et al., "Status and commissioning results of the R&D ERL at BNL", in Proc. of ERL2015, p. 11-15, 2015.

[7] I. Pinayev et al., "Performance of CEC POP gun during commissioning", in Proc of NAPAC2016, p. 1024-1026, 2016.

[8] T. Miller et al., "LEReC instrumentation design & construction", in Proc of IBIC2016, p. 417-421, 2016.

[9] C. Liu et al., "Design and simulation of emittance measurement with multi-slit for LEReC", in Proc of NAPAC2016, p. 1045-1047, 2016.

[10] T. Rao et al., "Multialkali cathode for high current electron injector-fabrication, installation and testing" presented at ERL 2017, Geneva, Switzerland, June 2017, paper MOIBCC004, this conference.

[11] S. Seletskiy et al., "Conceptual design of LEReC fast machine protection system", in Proc of IBIC2016, p. 665-668, 2016.

[12] L.Young, J.Billen, PARMELA, LANL Codes.

DEVELOPMENT OF AN ERL RF CONTROL SYSTEM*

S. Orth[†], H. Klingbeil, D. Domont-Yankulova, Institut für Theorie Elektromagnetischer Felder,
Accelerator Technology Group, TU Darmstadt, Germany

Abstract

The Mainz Energy-recovering Superconducting Accelerator (MESA), currently under construction at Johannes Gutenberg-Universität Mainz, requires a newly designed digital low-level radio frequency (LLRF) system. Challenging requirements have to be fulfilled to ensure high beam quality and beam parameter stability. First, the layout with two recirculations and the requirements will be shown from an LLRF point of view. Afterwards, different options for the control system are presented. This includes the generator-driven system, the self-excited loop and classical PID controller as well as more sophisticated solutions.

OVERVIEW AND REQUIREMENTS OF MESA

At Johannes Gutenberg-Universität Mainz a new accelerator will be built: The Mainz Energy-recovering Superconducting Accelerator (MESA). This accelerator will not only feature high current beams, feasible by means of energy recovery, but will also be operated as conventional multi-turn linac with a polarized electron beam. A part of the building is yet to be constructed and civil works will begin in 2018. The accelerator itself is scheduled to be constructed in 2020, but some parts can already be tested in existing halls [1].

Figure 1 shows a (preliminary) lattice [2]. The source
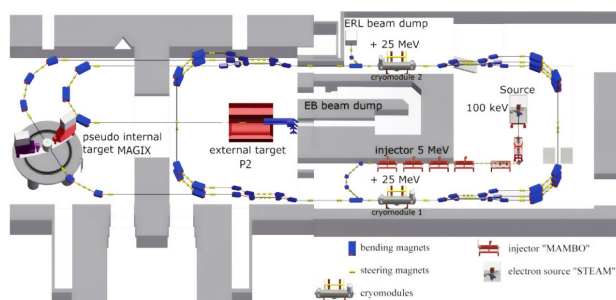
Figure 1: MESA lattice as of 2016.

called STEAM [1] ("Small Thermalized Electron-source At Mainz") will deliver a beam of polarized electrons which are pre-accelerated up to 5 MeV in the injector MAMBO ("Milli Ampere Booster") before they enter the main linac. MESA uses a double-sided layout with two cryomodules, providing an energy gain of up to 25 MeV each. After passing the cryomodules the beam is guided through the arcs for multi-turn operation. Separator magnets split the beams of different energies and recombine them before entering the cryomodules again or before experimental use.

Two experimental sides are foreseen: If MESA works as a 3-turn linac without energy recovery, the beam will be used in the so-called "external target P2" for high precision measurements of the Electro-Weak mixing angle [1]. In this mode, a 0.15 mA polarized electron beam will be accelerated to 155 MeV. Since there will be no energy recovery after P2 the beam will be dumped at high energy. This makes heavier shielding for radiation protection necessary.

The other operation mode will be the energy-recovery mode. In this mode, the beam will interact with the pseudo internal target called MAGIX which is a windowless gas target [1]. There will only be two passes, since this experiment only needs lower energies—but ideally, the available energies range from quite as low as 25 MeV up to a maximum of 105 MeV. The use of energy recovery makes higher currents feasible. In the first stage, a current of 1 mA is planned which shall be upgraded to 10 mA in the second stage. Currently, discussions are ongoing whether this mode will also make use of polarized electrons [1]. There are many possible experiments in MAGIX' portfolio, from nuclear physics to the search for dark matter [1].

All the experiments will require high accuracy and stability of the accelerating RF field while a wide variety of parameters (e. g. beam current and energy) has to be dealt with. The RF control system will have to handle this on demand.

Multi-Turn ERL Layout

In this paper, the focus is set to the energy-recovery mode. The path a beam takes is sketched in Fig. 2, starting from the injector through the main linac to the internal experiment and back on the decelerating phase ending in the beam dump. The beam re-enters the cavities 180° out of phase
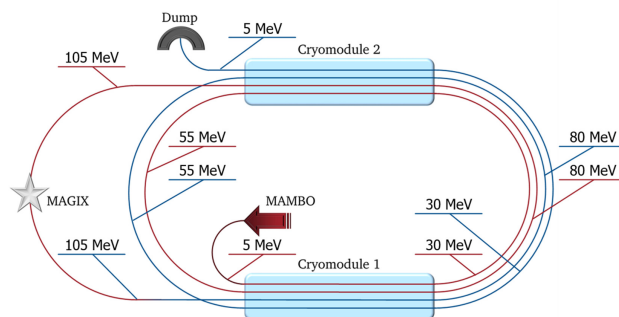
Figure 2: Sketch of the way a beam travels through MESA in the energy-recovery mode. Red: accelerating phase. Blue: decelerating phase. Note that the spatial separation is meant to clarify the different ways—in reality, the bunches are interleaved and those with the same energy share also the same beampipes in the arcs.

with respect to the accelerating field. This is achieved by path-length variation in the last arc with the internal target. As can be seen in Fig. 2, there will be four different beams in each cryomodule. MESA will be operated in continuous-wave (CW) mode and in the upgraded stage 2 this would result in a DC current of 40 mA in each cryomodule and thereby a very high beam loading. But since two of the four beams are on the decelerating phase their energy is given to the accelerating beams so that for perfect energy recovery the "RF currents" cancel each other. This results in a significantly reduced RF power demand, as can be seen from Eq. (1) and Eq. (2), which describe the required RF power in terms of the amplitude of the accelerating voltage V_{acc}, the (resulting) beam current I_{beam}, the beam phase relative to the crest φ_{beam}, the cavity's $\frac{R}{Q}$, the loaded quality factor Q_L, the coupling factor β_c, the detuning $\delta\omega$ and the 3 dB bandwidth $\Delta\omega_{BW}$ [3].

$$P_{RF} = \frac{V_{acc}^2}{4\frac{R}{Q}Q_L}\frac{1+\beta_c}{\beta_c}\left[\left(1+\frac{R}{Q}Q_L\frac{I_{beam}}{V_{acc}}\cos\left(\varphi_{beam}\right)\right)^2\right.$$
$$\left.+\left(\frac{2\delta\omega}{\Delta\omega_{BW}}+\frac{R}{Q}Q_L\frac{I_{beam}}{V_{acc}}\sin\left(\varphi_{beam}\right)\right)^2\right] \tag{1}$$

In the case of perfect energy recovery there is no beam loading [3] and Eq. (1) reduces to

$$P_{RF} = \frac{V_{acc}^2}{4\frac{R}{Q}Q_L}\frac{1+\beta_c}{\beta_c}\left[1+\left(\frac{2\delta\omega}{\Delta\omega_{BW}}\right)^2\right]. \tag{2}$$

Note that due to different conventions other authors may use the factor 8 instead of 4—here the so-called linac definition is used, while there also exists the circuit definition originating from the cavity's equivalent LRC model.

Equation (2) also reveals that the RF power demand in the energy-recovery mode strongly depends on the cavity detuning $\delta\omega$ due to microphonics. Therefore resonance control is crucial.

In the next section some control system basics are summarised and a theoretical model of the cavity is presented before the attention is drawn back to more specific issues related to the control of superconducting cavities.

CONTROL SYSTEM BASICS

In Fig. 3 the basic feedback loop is shown. A desired input signal is given to the controller to generate a steering signal for the plant. The output of the plant is then measured by a sensor and fed back to the input. The difference between the input and the actual measured output gives the "error" signal which the controller tries to reduce and ideally fix to zero. In reality there are also disturbances acting on the steering signal and the measurement is noisy as well (the latter is not shown here).

The "plant" in question are superconducting cavities with a resonance frequency of 1.3 GHz together with the power
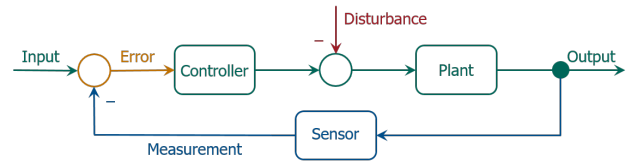
Figure 3: Basic feedback control loop.

sources, couplers, transmission lines, amplifiers, and the cavity tuners.

In general there will be more than just one sensor. In the special case of an LLRF system one could measure the amplitude and phase of the RF field inside the cavities (or the so-called in-phase and quadrature components I & Q) but additionally measuring the forward and reflected power as well as the actual tuning and the beam position would be possible. Since the measurement is an important component of the feedback loop, controlling a quantity (like the amplitude) without proper measurements is (almost) impossible.

In the following section some options for the controller will be shown, but first the "plant" is discussed in more detail.

Model of SC RF Cavities

MESA will make use of two modified "ELBE-type" cryomodules [2]. Their cross section is shown in Fig. 4. As can be seen, each cryomodule will house two nine-cell cavities. For the development of an RF control system, a theoretical
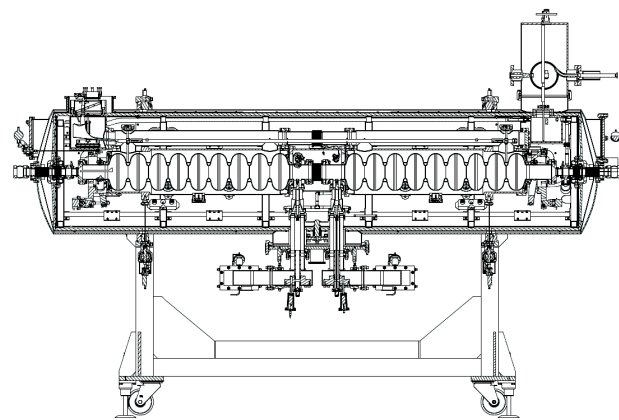
Figure 4: Modified ELBE-type cryomodule for MESA.

model of the plant is needed. Superconducting cavities are usually simplified by an equivalent LRC circuit [4, 5]. The "RF generator", which includes the amplifier, delivers the power to the cavity via waveguides. A circulator prevents the amplifier from damage by reflected power and couplers connect the transmission line to the cavity, see Fig. 5. From the cavity's point of view this model can still be simplified by substituting the coupler and all elements to the left of it by an *equivalent power source* delivering the current $\tilde{i}_{gen}(t)$ while the beam itself is also modelled as a current source delivering $i_{beam}(t)$. In this process the cavity's shunt impedance also has to be modified, since it is connected in parallel to
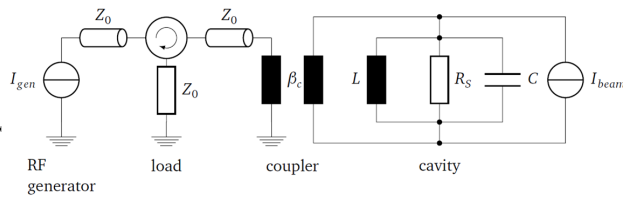
Figure 5: Simplified model of a superconducting cavity, including the power source and transmission lines.

the generator impedance (seen through the coupler). One finally ends up with the simplified circuit shown in Fig. 6. This model represents just a single resonance, but due to
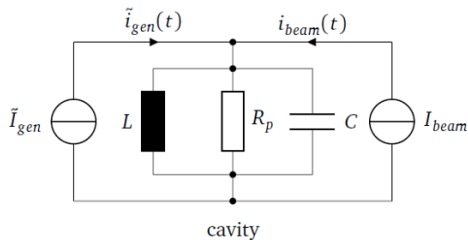
Figure 6: Simplified model of a superconducting cavity with (equivalent) current sources.

the narrow bandwidth of superconducting cavities, this is nevertheless useful for describing the accelerating mode [4].

Applying Kirchhoff's current law, one can easily derive the linear differential equation describing the cavity voltage $U_{cav}(t)$. By replacing the model's parameters R_p, L and C by their corresponding "accelerator" expressions, this equation reads [4]

$$\ddot{U}(t)+\frac{\omega_0}{Q_L}\dot{U}(t)+\omega_0^2 U(t) = \omega_0 \frac{R}{Q}\frac{d}{dt}\left(\tilde{i}_{gen}(t)+i_{beam}(t)\right). \quad (3)$$

For the development of an RF control system, the model shown in Fig. 6 together with Eq. (3) is used for simulations. It is a simple but yet powerful model which can represent the RF amplitude and phase, their transient & steady state behaviour as well as the cavity's reactions to beam loading, especially with an (interleaved) bunch train. It neglects the exact field distribution inside the cavity and is not able to reproduce HOMs, wakefields or the 6D phase-space motion of particles. At the very beginning of the development of an LLRF control system this is acceptable.

CONSIDERATIONS FOR THE CONTROL SYSTEM

Based on the basics described in the previous section, one can start to collect more specific requirements for the LLRF system.

First of all, the amplitude and phase of the accelerating (and decelerating) field shall be accurate and constant (within given tolerances that still need to be specified). In addition, especially for MESA, the control system has to support

the two different operation modes (energy-recovery mode and external-beam mode) with different numbers of passes, beam energies and currents as well as varying beam loading. Advanced control algorithms can enhance the stability and provide the user with additional diagnostic information. For further development and improvement the system should be modular and scalable so that one will be able to substitute some components without having to redesign the whole system. These key-points make a *digital control system* preferable (see also [6]).

Options for the Feedback Loop

For the basic design of the feedback loop, two different approaches exist: the Generator-Driven Resonator (GDR), see Fig. 7, and the Self-Excited Loop (SEL), see Fig. 8 [4].
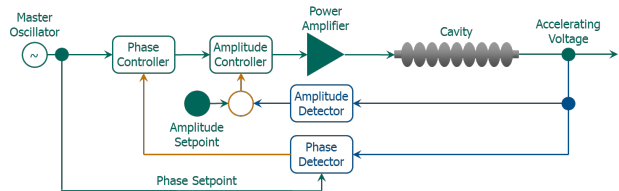
Figure 7: Example of the "Generator-Driven Resonator" feedback loop.
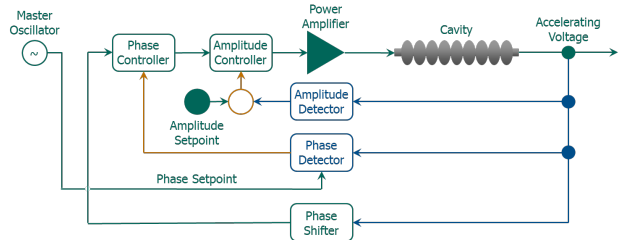
Figure 8: Example of the "Self-Excited Loop".

The GDR is a "straight-forward" approach, i. e. it resembles the basic feedback loop shown in Fig. 3. The Master Oscillator's signal is directly used to drive the amplifiers which power the cavity. In this example, amplitude and phase feedback is shown instead of I & Q. This "direct way" has the advantage that the start-up, i. e. filling the cavity with RF power, can be precisely timed and fast. Therefore one needs to carefully control the cavity's resonance frequency—the amplifiers won't be able to power the cavity if they are operating too far away from the cavity's resonance frequency. Lorentz-force detuning and its compensation are a major issue for the GDR.

In the SEL, the Master Oscillator is used as reference for the phase setpoint but the amplifier's input is the cavity's voltage signal itself. If the phase of the cavity's voltage signal is adjusted to an integer multiple of 2π, even small thermal noise will be amplified—the cavity can start oscillating without any external input or reference. The real system will include a limiter which is not shown in Fig. 8. The main

advantage is that one does not have to care about Lorentz-force detuning since this effect is automatically compensated. Since the cavity starts oscillating from thermal noise it can also start in an unwanted mode. This gives some "randomness" to the start-up and may slow down this process. One can account for this by *modifying the noise* [7]: The cavity acts as a very narrow bandpass filter and if some weak narrow bandwidth random signal centered on the expected resonance frequency of the accelerating mode is used as input, the SEL will lock to this desired mode. After that, the amplifiers can be turned to full operation power. This start-up procedure can be as fast as the GDR start-up but benefits from all advantages the SEL has over the GDR [7].

Options for the Controller

As mentioned earlier, the RF power needed in the energy-recovery mode is highly affected by microphonics. In addition—and even worse for the experimentalists—the stability of the accelerating field is affected by it. Since stability is a key feature of future experiments, compensating microphonics will be very important. The modified ELBE-type cryomodules will make use of fast piezo tuners for cavity resonance control (the tuners are not shown in Fig. 7 & 8). For predictable disturbances, e. g. arriving bunches, the concept of (adaptive) feedforward can bring additional benefits and improve the overall performance of the control system [6].

For the controller there are also a couple of options. The classical PID controller is a widely-used concept, which suffers from noise in the "D" part. Therefore many LLRF control systems for superconducting cavities deploy PI control only. This reduces the speed of the control system but if it is fast enough the increased stability is considered to be better. Nevertheless, since this is a known problem, there are some solutions. One is the so-called Kalman filter which replaces the system's state with an *estimator* from a series of measurements, thereby significantly reducing the noise. Another option is the state observer. This control scheme places a model of the actual "plant" in parallel to the real system. The model's input is exactly the same as for the real system and by comparing the outputs of both systems (real and model) one can adjust the model to track the real system. Internal states of the real system can be read out from the model and used for feedback control (when the controller uses internal states of the system, this is commonly referred to as "state control"). Besides that there is robust control, a design that makes the controller independent of system parameter variation or uncertainty (to some extent). This can be done by "H infinity" control (H∞)—the controller is optimized by modelled system parameter uncertainties.

But: All these options are a priori not determinable. The development of an LLRF control system—like any control system—starts with system identification and setting up the topology. At the current state of this project, these options are considered, but a deep understanding of the system's dynamical behaviour is the precedent step.

SUMMARY AND OUTLOOK

MESA, a multi-turn energy recovery linac, will be constructed at Johannes Gutenberg-Universität Mainz. Civil works are scheduled to start in 2018 and the building of the accelerator itself shall start in 2020. In the meantime some components can already be tested in the existing halls.

The LLRF system design has started and R&D of a generic digital RF control system is in progress. The first step will be modelling and understanding of the system behaviour, especially in multi-turn energy-recovery mode. Afterwards, an appropriate control system topology will be chosen.

Since there is some time until the commissioning of the accelerator, further analytical and numerical investigations shall follow to optimize the digital control system and to improve the system performance applying more sophisticated controllers & signal processing techniques.

REFERENCES

[1] K. Aulenbacher, "Nuclear Physics Experiments at MESA", presented at ERL17, Geneva, Switzerland, June 2017, paper FRIACC002, this conference.

[2] T. Stengler *et al.*, "Status of the Cryomodules and Cryogenic System for the Mainz Energy-Recovering Superconducting Accelerator MESA", in *Proceedings of IPAC2016*, Busan, Korea, 2016, pp. 2134–2137.

[3] K. Aulenbacher *et al.*, "Elementary Design Report for the Mainz Energy Recovering Superconducting Accelerator MESA", Technical report, Institut für Kernphysik, JGU Mainz, Germany, 2014.

[4] M. Konrad, "Development and commissioning of a digital rf control system for the S-DALINAC and migration of the accelerator control system to an EPICS-based system", Ph.D. Thesis, TU Darmstadt, Germany, 2013.

[5] S. Simrock, "Options for RF Control & State of Art Simulation and Performance", presented at ERL2005, Newport News, Va, USA, March 2005.

[6] S. Pfeiffer, "LLRF Controls and Feedback", presented at CAS on FELs and ERLs, Hamburg, 2016.

[7] I. Ben-Zvi, private communication, June 2017.

STUDY OF MICROBUNCHING INSTABILITY IN MESA[*]

A. Khan[†], O. Boine-Frankenheim, Institut für Theorie Elektromagnetischer Felder, Darmstadt, Germany

K. Aulenbacher, IKP Mainz, Mainz, Germany

Abstract

The Institute for Nuclear Physics (KPH) at Mainz is building a multi-turn energy recovery linear accelerator, the Mainz Energy-recovering Superconducting Accelerator (MESA), to deliver a CW beam at 105 MeV with short pulses, high current and small emittance for physics experiments with an internal target. Space charge effects potentially cause beam quality degradation for medium energy beams in smaller machines like MESA. As beam quality preservation is a major concern in an ERL during recirculation. We present a study on Microbunching Instability (MBI) caused by Longitudinal Space Charge (LSC) in MESA. Our results demonstrate the impact of the MESA arc lattice design on the development of Microbunching Instability.

INTRODUCTION

Energy recovery linacs (ERLs) provide electron beams of high current, high intensity with short pulses, facilitating their use as apparatus for various physics experiments and as free electron laser (FEL) drivers. ERLs were first proposed in 1965 and have gained tremendous interest since the 21st century [1]. At present, there are three operating ERLs: the JLab IR FEL Upgrade, the Japan Atomic Energy Agency (JAEA) FEL, and the Novosibirsk High Power THz FEL. While ERLs such as these three have been used largely for applications as FEL drivers, a large amount of research is focused on alternative applications such as dark photon detection and scattering experiments. Currently, upcoming ERL facilities include cERL at KEK, BerlinPro, and the Mainz Energy-recovering Superconducting Accelerator (MESA).

A detailed understanding of the physics of high current and high intensity beams in ERLs is of fundamental importance to preserve beam quality. While rapid advances have been made in the field of ERLs through investigations using particle tracking, the effect of space charge has received less attention. Space charge will be important in smaller machines and for medium energy and might, for example also affect the transport matrix in the arcs for recirculation [2]. It is important to develop an effective methodology to optimize the effect of space charge on lattice arcs. There is a need to explore measures to circumvent beam mismatch and corresponding emittance growth. Such studies rely on accurate predictions of the 3D beam envelope in the presence of space charge [3]. Longitudinal space charge (LSC) together dispersion can lead to the amplification of the initial shot noise, which is the well-known microbunching instability (MI). The linear microbunching gain process due to LSC

can be depicted as follows [4]:

$$G \simeq 4\pi \frac{I_0}{I_A} L_s \frac{|Z(k)|}{Z_0} k |R_{56}| \quad (1)$$

where $Z(k)$ is longitudinal space charge impedance, R_{56} is the longitudinal dispersion, the bunch peak current I_0 and the Alfven's current I_A.

We adopt the LSC impedance derived in Ref. [5]. The beam is assumed transversely uniform with a circular cross section of radius r_b [5],

$$Z(k) = \frac{iZ_0}{\pi\gamma\, r_b} \left[1 - \frac{kr_b}{\gamma} K_1 \left(\frac{kr_b}{\gamma} \right) \right] \quad (2)$$

where $r_b \approx 1.7(\sigma_x + \sigma_y)/2$.

The goal of our study is to predict the microbunching instability due to LSC, for the specific MESA lattice and beam parameters which we will describe below. Further, as a first step, we analyze the MESA lattice parameter in the presence of 3D space charge.

BRIEF OVERVIEW OF MESA

MESA is a small-scale, multi-turn, double-sided recirculating linac with vertical stacking of the return arcs operating in cw mode. Currently there are two planned experiments in MESA [6]:

(I) Fixed target experiment for precise measurement of the Weinberg angle with the beam extracted to the experiment in the external beam (EB) mode at 155 MeV.

(II) Pseudo Internal Target (PIT) experiment in search for dark photons with high luminosity as compared to storage rings due to low emittance life time.

A 3D sketch of MESA is shown in Fig. 1. It consists of a 100 keV polarized photo-cathode electron gun [7] with a normal conducting injector linac with an extraction energy of 5 MeV. The photo-cathode electron gun produces very short electron bunches. There are two superconducting linac modules with an energy gain of 25 MeV for each pass with four spreader sections for separating and recombining the beam and two chicanes for injection and extraction of the 5 MeV beam [8]. For beam recirculation there are five arcs to support the beam corresponding to five different energy levels: 55 MeV, 80 MeV, 105 MeV, 130 MeV and 155 MeV. The proposed beam parameters for MESA are in Table. 1. After the PIT experiment, the beam re-enters the main module with a 180^0 phase shift and starts to decelerate. The decelerated beam is dumped at 5 MeV [8].

[†] khan@temf.tu-darmstadt.de
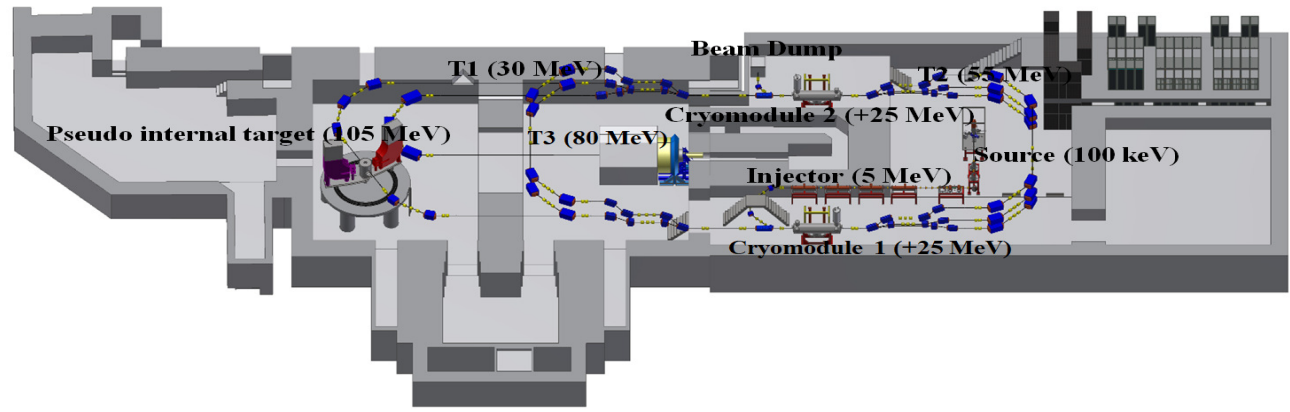
Figure 1: 3D sketch of MESA

Table 1: MESA Beam Parameters

Beam Parameter	Value	Unit
Beam Energy	105	MeV
Beam Charge	7.7	pC
Beam Current	10	mA
Operation Frequency	1300	MHz
Bunch Length	1.281	mm
Normalized emittance	0.002	mm mrad

MATCHED ENVELOPES WITH SPACE CHARGE

The beam envelopes and lattice functions are obtained by solving the envelope equations by a matrix method, including the linear defocusing effect of space charge [9, 10].

The space charge modified rms envelope equations for the rms beam radii $\sigma_{x,y}$ including dispersion are (see e.g. [2]):

$$\frac{d^2\sigma_x}{ds^2} + \left(\kappa_x(s) - \frac{K}{2X(X+Y)}\right)\sigma_x - \frac{\epsilon_x^2}{\sigma_x^3} = 0$$

$$\frac{d^2\sigma_y}{ds^2} + \left(\kappa_y(s) - \frac{K}{2Y(X+Y)}\right)\sigma_y - \frac{\epsilon_y^2}{\sigma_y^3} = 0 \qquad (3)$$

$$\frac{d^2D}{ds^2} + \kappa_x(s)D - \frac{K}{2X(X+\sigma_y)}D = \frac{1}{R}$$

where the effective horizontal beam radius is $X = \sqrt{\sigma_x^2 + D^2\delta^2}$ and K is the space charge perveance, which measures the strength of space charge, defined by $K = eI/\left(2\pi\epsilon_0 m\beta^3\gamma^3\right)$, I is the beam peak current, β and γ are the relativistic factors. $\kappa_{x,y}$ are the focusing gradients and R is the bending radius. $\epsilon_{x,y}$ are the rms emittances. Instead of the envelopes we solve for the the beam matrix B_s along the longitudinal position s: $B_s = M.B_{s_0}.M^T$ with M as transport matrix $M(s_0, s_0 + \Delta s) = M_{\Delta s/2}M_{\Delta s}^{sc}M_{\Delta s/2}$, where M^{sc} is the space charge kick. A matched solution is found using an iteration scheme for the desired envelopes at the exit.

RESULTS AND DISCUSSION

Figure 2 and Fig. 3 (b) show beta functions of MESA along the longitudinal axis in the absence and presence of space charge effects respectively. As can be seen in Fig. 3 (b), with the inclusion of space charge effects, there appears to be a strong mismatch in beam envelopes in the range (as depicted in Fig. 2) of the PIT experiment.
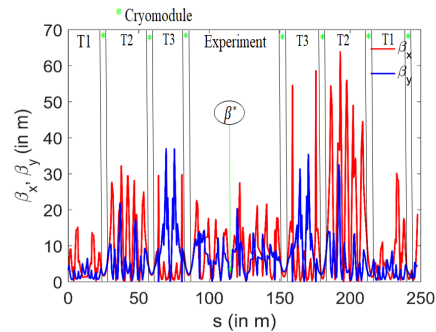
Figure 2: Beta functions of MESA in ERL mode in the absence of space charge effects.
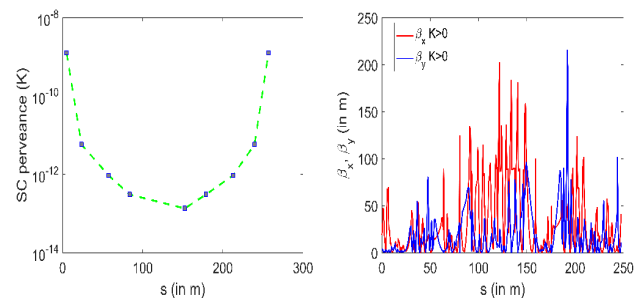
Figure 3: (a) Variation of space charge perveance along the beamline. (b) Beta function of MESA in ERL mode in the presence of space charge effects at design current 10 mA.

Figure 4 (a) shows the Variation of LSC gain function $G(s)$, along the beamline, for four different modulation wavelengths . Microbunching gain at $\lambda = 10\,\mu m$ is greater than the gain at three other values $\lambda = 0.1$, 50 and $300\,\mu m$, at every point along the beamline. Since impedance is a function of modulation wavelength (see Eq. (2)), an accurate gain analysis requires scanning of the spectral range of modulation wavelengths. Figure 4 (b) shows the variation of LSC

THICCC002

gain spectrum $G(\lambda)$ at the exit of the lattice as a function of initial modulation wavelength. As shown in Fig. 5, LSC effect on microbunching gain appears to be increasing in the operating current range of MESA. The preliminary design of MESA for high-current electron bunch is therefore, at risk of microbunching instability. An improved design is required to suppress such instability. Alternatively a modified beam transport scheme may be considered to transport the electron beam through the multi-turn accelerator, while maintaining high beam quality that is necessary for physics experiments in MESA.
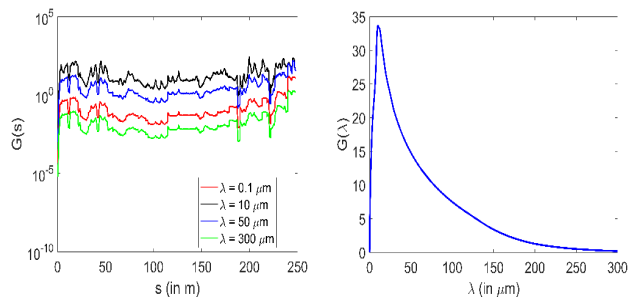
Figure 4: (a) LSC gain $G(s)$ along the beamline shown at four different wavelengths (red) $\lambda = 0.1\,\mu m$, (black) $\lambda = 10\,\mu m$, (blue) $\lambda = 50\,\mu m$, (green) $\lambda = 300\,\mu m$. (b) LSC gain $G(\lambda)$ as a function of initial modulation wavelength at beam exit.
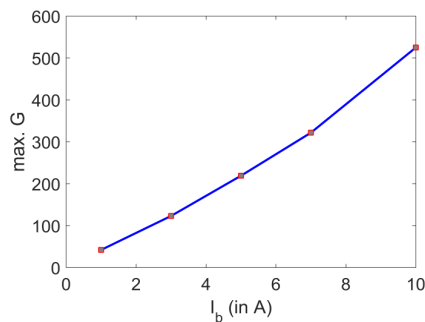
Figure 5: Initial current dependence of the maximal microbunching gains for MESA with space charge effects.

CONCLUSION AND OUTLOOK

The effect of space charge on the MESA lattice was investigated using a simple beam matrix method with space charge kicks. Since precisely adjusted beam envelopes are a key component of the PIT experiment, the effect of space charge

which can create a global mismatch of beam envelopes at different energies, should be well controlled. The microbunching instability is present in the operating range of the accelerator beam parameters. Further optimization of the recirculation arcs for intensity effects is foreseen. Space charge is prominent at low energies during beam injection and extraction. It will therefore be necessary to include 3D space charge in start-to-end simulations.

ACKNOWLEDGEMENT

REFERENCES

[1] L. Merminga *et al.*, "High-Current Energy-Recovering Electron Linacs", *Annu. Rev. Nucl. Part. Sci*, 53,387 (2003).

[2] Y.S. Yuan *et al.*, "Dispersion-Induced Beam Instability in Circular Accelerators", *Phys. Rev. Lett. 118*, 154801 (2017).

[3] Y.S. Lee *et al.*, "Space-Charge Dominated Beams in Synchrotrons", *Phys. Rev. Lett. 80*, 5133 (1998).

[4] E.L Saldin, "Longitudinal Space Charge Driven Microbunching Instability in TTF2 linac", *Nucl. Instr. Meth.*, vol. 483, pp. 516-520 (2002).

[5] M. Venturini, "Models for Longitudinal Space Charge Impedance for Microbunching Instability", *Phys. Rev. ST Accel. Beams 11*, 034401 (2008).

[6] K. Aulenbacher*et al.*, "Opportunities for Parity Violating Electron Scattering Experiments at the Planned MESA Facility", *Hyperfine Interact. 200*, 3 (2011).

[7] R. Heine *et al.*, "Lattice And Start To End Simulation of the MAINZ Energy Recovering Superconducting Accelerator MESA", *Proceedings of IPAC2014*, MOPRO108 (2014).

[8] D. Simon *et al.*, "Lattice And Beam Dynamics of the Energy Recovery Mode of the MAINZ Energy-Recovering Superconducting Accelerator MESA", *Proceedings of IPAC2015*, MOPWA046, Richmond, VA, USA.

[9] F.J. Sacherer *et al.*, "RMS Envelope Equations with Space Charge", *IEEE Trans. Nucl. Sci. 18*, 1105 (1971).

[10] M. Venturini *et al.*, "rms Envelope Equations in the Presence of Space Charge and Dispersion", *Phys. Rev. E 57*, 4725 (1998).

ERL17 WORKSHOP, WG1 SUMMARY: INJECTORS

Erdong Wang, Brookhaven National Laboratory, New York, USA

Kurt Aulenbacher , University Mainz, Germany

Abstract

The 59th ICFA Advance Beam Dynamics Workshop on Energy Recovery Linacs, hosted by the CERN was held on CERN campus. The working group (WG) 1 ERL injectors focused on high-brightness, high-power CW electron gun and high QE long lifetime semiconductor photocathode. The working group 1 was separated into two sessions: One is electron gun session, which has eight invited talks; another is photocathode session, which has six invited talks and one contributed talk. This report summarizes the state of the art of electron guns and photocathodes discussed in the ERL workshop WG1.

INTRODUCTION

Energy Recovery Linacs (ERL) enable the generation of high current high brightness electrons beam with high energy and cost saving. The high current, low emittance electron sources are always one of the challenges of ERL. So far, there are several facilities successfully commissioned and operated the electron guns in last a few years. Also, several labs are capable of preparing high QE semiconductor photocathodes for electron guns. These experiences provide an opportunities to push to even higher quality electron source. However, the challenges are still existed such as long lifetime operation cathode, stable operation SRF gun as well as high current operation.

There are total 14 talks in WG1. A large variety of interesting and important topics have been presented in the WG1 sessions. From the number of talks, we identified 4 topics with two separated sessions: Session1 photocathode: i. High QE, long lifetime photocathode: CeC, LEReC (BNL), SHXFEL (SHLS),Mainz Univ. HZB, HZRD. ii. Cryogenic cathode: Cornell, HZB, HZRD Session 2: iii. DC gun: BNL, JAEA/KEK, Mainz Univ.,Cornell Univ., KEK,ALICE iv. SRF gun: BNL, HZDR, PKU DCSC, HZB.

This report concludes with the discussions of cathode and gun operation/commissioning results, concerns, technical issues related to electron source realization and interesting concepts.

SUMMARY OF PHOTOCATHODE SESSION

The photocathode session has seven talks. All talks are discussed alkali antimony based photocathode including CsK_2Sb, KNa_2Sb, and Cs_3Sb. Alkali antimony photocathodes have advantages on visible light sensitive (Green prefer), high QE, low thermal emittance and long lifetime. It could use in DC gun, RF gun, and SRF gun. The presenter Dr. Taro Konomi from KEK, Dr. Triveni Rao from BNL, and Dr. Julius Kuhn from HZD showed the prepared antimony based photocathode can reach 10% QE

with the green laser. More discussions brought up in these talks: 1) Using ITO as a substrate to generates transparent photocathode for RF sealing. The cathode QE is almost equalized using reflection mode and transparent mode by a green laser. Transparent photocathode has advantages on simplified the laser transport system and obtaining the low emittance electrons. 2) The cathode routing production system requires very high capacities of alkali source. Conventional SAES sources are not sufficient for continuous cathode preparation. So J-bend effusion cells are developed and used in routing alkali antimony cathode preparation. 3) Using the cathode in cryogenic environments is an open discussion issue for many years. Measure the cathode QE evolution in temperature reducing helps to understand the cathode performance in SRF gun. Besides on high current operation, obtain low transverse and longitudinal emittance electrons beam are very important directions for electron source development. Dr. Monika Dehn From Univ. Mainz compared the multialkali PEA material's longitudinal temporal response with GaAs NEA material and found that the PEA material has significantly short bunch tail. Prof. Ivan Bazarov from Cornell Univ. discussed the cathode in a cryogenic environment and combining with transparent mode operation will generate orders of magnitude lower mean transverse energy electrons. More labs involve the alkali antimony photocathode development. Some labs switch from GaAs photocathode to alkali antimony photocathode for either DC gun or RF gun. The presenter Zhenggong Jiang from SHLS and Dr. Nishimori from KEK presented their new developed alkali antimony deposition systems.

In open discussion, we have two major opening discussion topics, which were recommended to future R&D.

1) Several labs tested the cathode performance in cryogenic temperature. For the HZB case, the cathode QE at long wavelength side is increased once cathode cool down to LN2 temperature. It is possible caused by the phonon scattering domination in cathode crystal. In the cryogenic environment, the phonon-electron scattering rate decreased, then the QE increase. This may be related to the cathode lattice structure, defects or surface states. The advantage is possible to cool the cathode, generate low thermal emittance electron beams with high QE.

2) Recently, The challenge will be using the alkali semiconductor cathode inside the SRF gun, either caused multipacting or lifetime concerns. It is possible to develop advanced cathodes without any alkali metals or say with superconducting prefered materials such as hydrogen, nitrogen? The diamond amplifier was studied at BNL in a few years before. This is only H_2 terminated on emission source. Recently, the SRF gun has tested with alkali antimony cathode. Test diamond amplifier may solve the issues found in SRF gun test.

SUMMARY OF GUN SESSION

The gun session has eight talks. Four of them talked DC gun, three of them talked SRF gun and one is about the hybrid DC-SRF gun. DC guns as matured electron source have been used for ERL machines such as ALICE and JLab-FEL. Dr. Lee Jones gave a summary talk of gun operation at ALICE ERL. JAEA/KEK DC gun and Cornell DC gun has been well commissioned. Dr. Nishimori showed the DC gun stable operation range with 1mA average current from GaAs photocathode. The DC gun at Cornell and BNL are explored the new applications on CBETA and LeREC, presented by Karl Smolenski from Cornell Univ. and Dr. Dmitry Kayran from BNL. Two SRF guns from BNL and HZRD showed encourage commissioning results. SRF gun is able to operate in CW mode with a high gradient on the cathode and extremely good vacuum due to cryogenic pumping. Dr. Igor Pinayev reported 113MHz QWR-SRF gun stable CW (26kHz) operation for CeC experiment with 0.32 mm-mrad normalized emittance at half nC. QWR SRF gun has advantages on high gradient, small energy spread, and 4K operations. The K_2CsSb cathodes in this gun have a lifetime more than a month without obviously decay. The multipacting eliminated with new cathode design and RF procedure progresses. Recently, the injector is not the limit of CeC experiment. Dr. Jochen Teichert from HZDR reported that both magnesium and Cs_2Te in 3.5 cell 1.3 GHz SRF gun delivered request beam for users with good lifetime. The issues are focused on increase cathode lifetime in transferring and long time stable operation with Cs_2Te cathode. The HZB gun is approaching to beam test once finish the RF gun. The RF tests show that the peak gradient could achieve 57.3 MV/m. Hybrid DC-SRF gun developed by Peking University has commissioned and delivered the beam for THz and UED experiment. The new design is going on for approaching the normalized emittance to sub mm-mrad.

In open discussion, we have two major opening discussion topics:

1. ERL's for fundamental researches need polarized beams with meaning mA currents with high charge lifetimes. High current polarized electron is useful in the project like future EIC. But there is only very little progress with respect to this topic. More resources should provide to the polarized electron source.

2. Given the fact that it is mandatory to solve this problem if a high average current ERL is to be of use, it seems that efforts should intensify. Even if one group would have the capability to generate 100mA average current for a long time with optimum beam conditions, the respective accelerator managements must understand that mastering the technology requires continuous effort in personnel for example photocathode specialist. Have a photocathode common platform is helpful such as Wiki web page or shared online procedure.

CONCLUSION

The progresses in injectors for ERLs at the last couple years are significant. Many labs start to interested in high QE alkali-antimonide photocathode. Most of the labs reached 10% QE of the cathode in green light and tested in their injectors. The maturity of DC gun technology, and their viability for ERL use has confirmed this year. SRF guns have breakthrough in last two years. Both BNL 113MHz QWR gun and HZDR SRF gun tested semiconductor photocathode with stable CW operation. The cathode lifetime in QWR SRF gun is more than a month without obviously decay. In the future, the injector efforts will push to high current, high brightness and stable operations. The photocathode research should focus on long lifetime, high QE with SRF preferable cathode.

ACKNOWLEDGMENTS

The authors would like to thank the workshop organizers and participants of the working group I for the excellent presentations and lively discussions during and in-between the sessions.

ERL17 WORKSHOP, WG2 SUMMARY:
OPTICS, BEAM DYNAMICS AND INSTRUMENTATION

S.A. Bogacz, Jefferson Lab, Newport News, VA, USA
D. Schulte, CERN, Geneva, Switzerland

During the workshop a number of interesting projects were discussed: ERL at KEK, ALICE, PERLE, LHeC, eRHIC, CBETA, ERL for MESA and bERLinPro; a nice mixture of future, existing and past facilities. As a message for future ERL facilities, past operational experience and optimization efforts from ALICE were highlighted (P. Williams/Daresbury). Importance of implementing separate diagnostics for the lattice and the beam was emphasized along with a need for simulations aimed at step-by-step modeling of procedures one needs to exercise to establish the beam conditions defined by milestones of the project. Valuable experience of high charge per bunch operation of compact ERL at KEK was also presented (T. Miyajima/KEK).

Three talks were devoted to beam dynamics challenges of CBETA (G. Hoffstaetter/Cornell, C. Mayes/SLAC, S. Berg/BNL); covering lattice design, magnet technology and orbit control. With four different energies CBETA becomes a test-bed for multi-pass beam dynamics issues, such as: time of flight control for beams with energy spread and the recirculative BBU (addressed by cavity design with strong damping).

Extending the quest for more passes in a racetrack ERL, optimized linac optics for 5-pass ER@CEBAF was presented. Multi-pass energy recovery in a racetrack topology explicitly requires that both the accelerating and the decelerating beams share the individual return arcs. This in turn, imposes specific requirements for the TWISS function at the linacs ends.

As an ultimate application of multi-pass ERLs the FFAG, 6-pass e-RHIC ring was highlighted (V. Ptitsyn/BNL). Here, CBETA will provide an important synergistic input. Even so, recently the Ring-Ring option has become more in the focus for the eRHIC design, there are still efforts on ERL-Ring option for eRHIC.

A comprehensive review of beam dynamics driven design of the LHeC, 60 GeV ERL was presented (D. Pellegrini/CERN), which is probing the longitudinal acceptance limits in high energy ERLs. Extreme synchrotron radiation effects (almost 2 GeV energy loss around a 3-pass racetrack) were simulated to assure that the SR induced energy spread and corresponding emittance dilution due to quantum excitations will not impede the energy recovery process on the decelerating passes. These effects along with beam-beam, short and long range wake-fields and imperfections were simulated with PLACET2 and ELEGANT. The resulting End-to–End simulation showed acceptable levels of energy spread and emittances all the way to the dump, vastly dominated by the synchrotron radiation effects.

Probing the limits of virtual power vs RF power in high current ERLs, two presentations on rapidly developing bERLinPro highlighted the overall design and project commissioning status (A. Jankowiak/HZB), as well as the beam dynamics challenges of the extreme high current (100 mAmp) operation (M. Abo-Bakr/HZB). In the same category of high power ERLs, PERLE – the newly proposed ERL Test Facility at Orsay – was introduced (W. Kaabi/LAL) along with its current layout and optics design (A. Bogacz/JLAB). A future R&D program was presented to fully develop a Technical Design Report, which will require work in the following areas:

- Liner lattice optimization and initial magnet specs
- Momentum acceptance and longitudinal matching
- End-to-End simulations with synchrotron radiation, CSR micro-bunching (ELEGANT)
- Correction of nonlinear aberrations (geometric & chromatic) with multipole magnets (sextupoles and possibly octupoles)
- RF cavity design, HOM content BBU studies (TDBBU)
- Injection line/chicane design space-charge studies at injection
- Diagnostics & Instrumentation
- Multi-particle tracking studies of halo formation
- Final magnet specs
- Engineering design

Operational experience of another superconducting linac based nuclear physics user facility – MESA – was described (F. Hug/U. of Mainz). This two-pass, high current (10 mAmp) ERL truly excels in versatility providing highly polarized beams to large number of experiments.

Finally, a clever lattice mitigation scheme for CSR/micro-bunching suppression was presented (C. Tennant/JLAB). As the lattice figure of merit, a variation of M_{56} (max value of M_{56} across the lattice) was chosen. Two lattices with diverse values of M_{56} variation were simulated with ELEGANT, introducing initial density fluctuation 'seed' and looking for the onset of micro-bunching instability. The results revealed striking suppression of instability growth for the case of minimum M_{56} variation.

In summary, we witness a rather vigorous development of new ERLs, aggressively pushing the limits:

- Maximizing number of passes
- Maximizing virtual beam power
- Opening longitudinal acceptance
- Mitigation of limiting factors: BBU, CSR/micro-bunching
- Diagnostics & Instrumentation for multiple beams
- Multi-particle tracking studies of dark current and halo formation (M. McAteer/HZB).

A bright future can be expected for the field.

ERL17 WORKSHOP, WG3 SUMMARY:
TEST FACILITIES AROUND THE WORLD

Georg H. Hoffstaetter, Cornell University, Ithaca, NY 14850, USA
Achille Stocchi, LAL, 91898 Orsay, France

This contribution has not been submitted.

ERL17 WORKSHOP, WG4 SUMMARY: SUPERCONDUCTING RF

I. Ben-Zvi, BNL, Upton, USA

F. Gerigk, CERN, Geneva, Switzerland

Abstract

Working Group 4 consisted of 10 talks (see References), which were split into three sessions around four main themes. These themes will be listed and summarized in the following along with a summary of the discussion session.

HIGHER ORDER MODE DAMPING AND FUNDAMENTAL POWER COUPLERS

ERL power couplers need to be able to provide 10's of kWs in Continuous Wave (CW) operation. While CW power transmission has been demonstrated up to levels of 500 kW (standing wave) or even 750 kW in travelling wave, e.g. at CERN [1], it became clear that a successful coupler development is a multi-year effort, which is only mastered by a few experts worldwide. For lower frequencies, which are often favoured by ERLs, coaxial couplers are typically preferred [2] with a new development of TE11 coaxial couplers showing particular promise to handle high average CW power. High-pass filters in Higher Order Mode Suppressors (HOMS) are relatively new and require further development.

ADVANCES IN SRF SURFACE PERFORMANCE

In CW ERLs, RF surface losses often determine the maximum gradients at which the SRF cavities can be used. Lowering surface losses therefore has a significant impact on the facility footprint, initial cost, and running costs of the RF stations and cryogenic installations. Recent advances in the field of nitrogen doping flattened out the Q-slopes (in 1.3 GHz cavities) up to gradients of around 25 MV/m. Nitrogen infusion, which is still being optimized shows high Q values even at high gradients up to 40/45 MV/m. The nitrogen infusion method offers the possibility to tailor cavities to specific applications [3]. The effort of Niobium on Copper coatings has re-started and first samples show that it is possible to flatten the Q-slope, which was typically observed on coated cavities up until today [4]. Further effort is needed to unblock the full potential of this technique, which is used at CERN for LEP, LHC, and recently the HIE-ISOLDE cavities.

MICROPHONICS AND RESONANCE CONTROL

Issues of microphonics and cavity resonance stability continue to challenge new SRF installations, especially in view of the recent advances with nitrogen doping/infusion, which substantially increases the cavity Q but which equally decreases the cavity bandwidth. In case of the LCLS-II cryo module this translates into a cavity half-bandwidth of 16 Hz and a peak detuning requirement of 10 Hz, which means that active resonance control is becoming mandatory for operation [5]. First beam has just been seen in the Main Linac Cryomodule (MLC) at the CBETA facility (Cornell), which also faces the challenge of operating with a very small bandwidth (10 Hz) [6].

As part of the Low-Level Control System (LLRF) [7] active resonance control typically consists of Lorentz Force detuning compensation via fast piezo tuners and adaptive feedforward algorithms. In order to achieve the small detuning levels, which are necessary for the active resonance control to work, the cavities [8], the cryo module design and the cryogenic supply system all have to be optimised for very low vibrations/microphonics [9].

CAVITY DESIGNS AND CRYOMODULE PERFORMANCE

Dual axis cavities [10] can offer significant advantages as they: i) allow to have a straight trajectory for the injection of low-energy beams, ii) allow dumping of beams with large energy spread (no dispersion in the dumped beam as there is no bend between the decelerating cavity and the dump), iii) have the potential of improved BBU suppression. Despite these advantages, there are very few proposals today to actually use this type of cavities in a machine (see discussion session).

DISCUSSION SESSION

Coated versus bulk Niobium cavities

The question of which fabrication technique to choose depends on the desired beam characteristics. For high-current applications lower frequency cavities are often chosen because of the lower excitation and easier extraction of HOM power. Due to their larger size, low-frequency cavities are mechanically more stable if made out of copper, as it was done for instance for the 350 MHz LEP cavities or the 400 MHz LHC cavities. For lower-current applications, higher frequency (> 650 MHz) multi-cell cavities out of bulk Nb are typically chosen, as they are easier to fabricate and require small cryostats. Recent progress in nitrogen doping/infusion have dramatically reduced the surface resistance of bulk Nb cavities and this technique is already being applied to the series production of LCLS-II cavities [3]. One can argue that nitrogen doping is in fact a thin film/coating technique as the ensuing physics takes place only in the top surface layer.

Nb/Cu has lower residual resistance at low fields than bulk Nb but has traditionally suffered from a strong Q-slope at higher fields. Recent work has related the Q-slope to small defects at the Nb/Cu interface. Moving

from sputtering to energetic condensation techniques first samples have shown a significantly reduced Q-slope, which indicates that further R&D may be able to yield substantial performance increases [4].

Further R&D in both techniques is strongly encouraged.

Dual-axis cavities – the way forward?

Questioned whether anyone would dare to use dual-axis cavities, the following points were raised: i) During a test of a dual-axis cavity at Los Alamos RF instabilities were observed. However, these were not related to the cavity itself but rather to a complicated bridge system used to put power into the cavities. Despite these issues successful lasing could be demonstrated; ii) the larger RF surface will increase the likelihood of having surface defects. However, considering that ERLs typically run at lower gradients and furthermore considering the successful recent commissioning of very long SC linacs (e.g. XFEL) it is assumed that the issue of the larger surface area can be mastered with modern Quality Assurance; iii) Using dual axis cavities may be especially interesting in cases where the beam quality in the injection is important, or where the returning beam has a large energy spread (such as in FELs). However, due to the added cost of doubling the number of cavities, this approach may be better suited to small ERLs with demanding beam conditions than for large ERLs, such as colliders.

RECOMMENDATIONS FOR FUTURE R&D

Coaxial couplers need further development for high average power capability. Especially TE11 power couplers should be investigated. Also high-pass, high-power HOMs should be studied further. Nitrogen infusion and thin films hold great promise for SRF cavity performance and both techniques need dedicated R&D programs to unlock their full potential. On cavity shapes we highly recommend a vigorous R&D program on dual-axis energy recovery cavities and for cryomodules we encourage the development of designs that minimise microphonics.

REFERENCES FROM ERL 2017

[1] E. Montesinos, "Power Couplers & HOM Dampers at CERN"

[2] Q. Wu, "Coaxial Couplers"

[3] M. Checchin, "High-Q R&D at FNAL"

[4] S. Aull, "The Potential of Nb/Cu Technology for High Beam Current Applications"

[5] W. Schappert, "Resonance Control of the PIP-II SC Cavities"

[6] F. Furuta, "Cornell ERL CM Performance"

[7] S. Orth, "Development of an ERL RF Control System"

[8] T. Miura, "Resonant Frequency Control at the Compact ERL in KEK"

[9] F. Furuta, "Microphonics Analysis of ERL Cryomodule"

[10] F. Marhauser, "Twin-Axis Elliptical Cavity"

ERL17 WORKSHOP, WG5 SUMMARY: APPLICATIONS

P. A. McIntosh†, STFC Daresbury Laboratory, Warrington, UK
I. Konoplev, Oxford University, Oxford, UK

Abstract

For the ERL17 Applications Working Group (WG5), a focus was identified for Photon science and Particle and Nuclear Physics application areas. For the Photon applications; THz, FEL and Compton drivers were most relevant and for the Particle and Nuclear Physics field, Compton, Polarised and Cooled beams were most prominent. The following then highlights the key performance needs, challenges and anticipated future demands for each of these application areas as reviewed and discussed at the workshop.

PHOTON APPLICATIONS

THz

For optimum THz user delivery, there is a fundamental need for high power and broad spectral range (ideally upto 3THz). It was noted that broadband, short-pulse, high repetition rate THz is inconsistent with competing demands for highly monochromatic and coherent THz delivery, which ideally should be accomplished using the same ERL platform. Good pulse-pulse THz stability is also a key operational requirement. The challenges to achieve such requirements are driven by the stability of the energy recovered beam in terms of bunch charge, beam energy, bunch length and RF stability. Careful and repeatable machine optimisation is therefore required, however it was noted that the use of a THz cavity could provide a more consistent THz beam for user exploitation. In addition, the transport of THz radiation across long distances is difficult and it was reported that Jlab have a precision HeNe laser alignment system which includes source-point tracking for their THz distribution line in order to minimise transmission losses from the ERL to their exploitation area. THz utilisation is most definitely a growing field of scientific research and with advent of diffraction-limited performance from synchrotrons, the scope for THz research is expected to expand even further.

FEL

For effective ERL delivery for FEL applications, the stability of the entire machine was cited as the fundamental requirement, in particular the beam energy and pulse-pulse stability in order to achieve the required FEL wavelength and output power. Utilisation of complex, fast feedback across the ERL laser, RF and FEL systems are identified as the most effective direct mitigation mechanism, however achieving higher repetition rates with equivalent stability performance is a fundamental target for ERLs in comparison with single pass linac topologies.

EUV

Industrial demands for achieving high power EUV radiation at <13.5nm wavelengths for X-ray lithography applications drive the FEL output performance to way beyond current state-of-the-art. Such an ERL platform requires >10kW EUV power at >98% machine availability with an extremely high degree of beam stability throughout the entire accelerator chain. In order to achieve such demanding requirements, necessitates a considerable level of inherent system redundancy and relaxation (wherever possible) of the sub-system complexity and operational demands, to the extent whereby even complete system replication can be incorporated, which will facilitate rapid change-over should a system failure occur. Such consumer demand is driving technologies to shorter and shorter wavelength regimes and whilst commercial commitment is not yet at the stage to formally launch a complete ERL platform delivery, this is likely to change in the near future as competing demand continues to strive towards higher integrated circuit transistor densities.

Compton

Laser Compton Scattering (LCS) techniques for both X-ray and γ-ray beam generation, with X-rays being used for medical imaging and γ-rays being used for nuclear material security interrogation. The demand for such capabilities requires high energy beams to enable reduced exposure times for imaging/interrogation; for X-rays, typically need 50MeV, 10mA and >100kW laser power to achieve ~40keV X-ray energy and for γ-rays utilising various Nuclear Resonance Fluorescence (NRF) techniques. For both, the key challenge is the provision of a suitable high power laser source which can be accommodated in a small footprint. A laser enhancement cavity which can store dual-beams with a fast polarisation switch appears to be a suitable solution for providing both X and γ-ray beam generation. Compact ERL platform demands for implementation into a hospital environment is an overriding challenge for medical imaging.

---

†peter.mcintosh@stfc.ac.uk

PARTICLE AND NUCLEAR PHYSICS AP- PLICATIONS

Polarisation and Cooling

Provision of a high performance polarised electron beam injector is a key technology requirement for cooling and spin polarised experiments. The challenge is in achieving the required peak current and operational Quantum Efficiency. Precise control is needed for the transported beam current, particularly for spin polarisation measurement of exotic particles, requiring optimised diagnostics to effectively characterise beam emittance, energy spread and fundamental photocathode performance.

CONCLUSIONS

For each of the application areas identified, an operational performance spreadsheet has been formulated, which attempts to collate the necessary beam parameters for each of the beam delivery programmes presented. Whilst this spreadsheet is not yet complete, it identifies some of the operational variability an ERL platform may hope to provide for Photon, Particle and Nuclear Physics programmes.

List of Authors

Bold papercodes indicate primary authors; ~~crossed out~~ papercodes indicate 'no submission'

— A —

Abo-Bakr, M.	~~WEIACC002~~, **WEIBCC003**
Ainsworth, R.	~~TUIACC003~~
Alarcon, R.	TUIACC001
Altinbas, Z.	WEICCC004, ~~WEIDCC002~~
Anders, W.	~~WEIACC002~~
Arakawa, D.A.	~~MOICCC003~~
Arnold, A.	**MOPSPP003**, ~~WEIDCC003~~
Arnold, M.	**MOIDCC006**
Aryshev, A.	~~MOPSPP011~~
Aulenbacher, K.	~~MOIBCC002~~, MOPSPP004, FRIBCC001, ~~MOPSPP001~~, MOPSPP005, MOPSPP006, MOPSPP007, MOPSPP008, THICCC002, **FRIACC002**
Aull, S.	**TUICCC004**

— B —

Balewski, J.	TUIACC001
Banerjee, N.	~~THIBCC002~~
Bazarov, I.V.	**MOIBCC001**
Büchel, A.B.	~~WEIACC002~~
Beaver, T.S.	**MOPSPP017**
Bechthold, V.	~~MOIBCC002~~, **MOPSPP004**, MOPSPP006
Belomestnykh, S.A.	~~WEIDCC002~~
Ben-Zvi, I.	WEIACC003, ~~WEIDCC002~~, **FRIBCC004**
Benson, S.V.	TUIACC001, WEIBCC004
Berg, J.S.	**TUIDCC004**
Bernauer, J.C.	TUIACC001
Bessuille, J.C.	TUIACC001
Bevins, M.E.	WEIACC003
Blyth, D.	TUIACC001
Bogacz, S.A.	**TUIDCC001**, WEIACC003, **FRIBCC002**
Boine-Frankenheim, O.	~~MOPSPP001~~, THICCC002
Borin, V.M.	MOIDCC002
Boyce, J.R.	TUIACC001
Brooks, S.J.	TUIDCC004
Brown, K.A.	~~WEIDCC002~~
Bruno, D.	WEICCC004
Brutus, J.C.B.	~~WEIDCC002~~
Bürkmann-Gehrlein, K.B.	~~WEIACC002~~
Burandt, C.	MOIDCC006
Burt, G.	~~TUIACC003~~

— C —

Cao, T.	TUIACC001
Cervantes, R.	TUIACC001
Checchin, M.	**TUICCC001**
Cheng, W.	~~WEIDCC001~~

Chi, Y.L.	~~WEIACC004~~
Ciovati, G.	~~MOPSPP003~~
Coleman, J.L.	TUIACC001
Corliss, R.	TUIACC001
Costanzo, M.R.	WEICCC004
Cowan, R.F.	TUIACC001
Craig, T.	~~TUIBCC001~~
Cricenti, A.	~~TUIBCC001~~
Crittenden, J.A.	TUIDCC004
Curcio, A.J.	~~WEIDCC002~~

— D —

Davidyuk, I.V.	MOIDCC002
De Silva, S.U.	~~TUICCC002~~
Dehmelt, K.	TUIACC001
Dehn, M.A.	**MOIBCC002**, MOPSPP004, MOPSPP006
Deichuli, O.I.	MOIDCC002
Delayen, J.R.	~~TUICCC002~~
Dementyev, E.N.	MOIDCC002
DeSanto, L.	~~WEIDCC002~~
Deshpande, A.	TUIACC001
Di Lieto, A.	~~WEIDCC002~~
Dipert, R.A.	TUIACC001
Dobbins, J.	~~TUICCC003~~, ~~THIBCC002~~
Domont-Yankulova, D.	MOPSPP002, THIBCC005
Dongwi, B.	TUIACC001
Dorokhov, V.L.	MOIDCC002
Douglas, D.	TUIACC001, WEIACC003, WEIBCC004
Dovzhenko, B.A.	MOIDCC002
Dubbé, C.J.	WEIACC003
Dunning, D.J.	~~TUIBCC001~~

— E —

Echevarria, P.	~~WEIACC002~~
Egi, M.	~~MOICCC003~~
Eichhorn, R.G.	~~TUICCC003~~, ~~THIBCC002~~
Enami, K.	~~MOICCC003~~
Epstein, C.	TUIACC001
Eschelbach, C.	MOIDCC006
Evtushenko, P.E.	TUIACC001

— F —

Fedotov, A.V.	WEICCC004
Feege, N.	TUIACC001
Feng, L.W.	~~WEIDCC001~~
Fichtner, F.	~~MOIBCC002~~
Fisher, P.F.	TUIACC001
Folz, C.	~~WEIDCC002~~
Frahm, A.	~~WEIACC002~~
Freitag, M.	~~MOPSPP003~~

Friederich, S.   MOPSPP004, **MOPSPP005**, MOPSPP006, MOPSPP008
Frierson, S.L.   TUIACC001
Friščić, I.   TUIACC001
Furuta, F.   **TUICCC003**, **THIBCC002**
Furuya, T.   ~~MOICCC003~~

— G —

Garçon, M.   TUIACC001
Gardner, P.   ~~TUIBCC001~~
Gassner, D.M.   WEICCC004, ~~WEIDCC002~~
Ge, M.   ~~TUICCC003~~, ~~THIBCC002~~
Gerigk, F.   FRIBCC004
Getmanov, Ya.V.   MOIDCC002
Glöckner, F.   ~~WEIACC002~~
Glock, H.-W.   ~~WEIACC002~~
Göbel, F.   ~~WEIACC002~~
Gonnella, D.   ~~TUICCC003~~
Gorbachev, Ya.I.   MOIDCC002
Gu, Q.   ~~MOIACC003~~
Gu, X.   WEICCC004
Guèye, P.   TUIACC001
Gubeli, J.   TUIACC001

— H —

Hajima, R.   ~~MOPSPP013~~, MOPSPP015, ~~WEICCC001~~, ~~THICCC003~~
Hall, B.D.S.   ~~WEIACC002~~
Hammons, L.R.   WEICCC004
Hao, J.K.   ~~WEIDCC001~~
Hao, Y.   WEIACC003
Harrison, P.   ~~TUIBCC001~~
Harvey, M.   ~~WEIDCC002~~
Hasell, D.K.   TUIACC001
Hayes, T.   ~~WEIDCC002~~
Hein, L.M.   **MOPSPP006**, MOPSPP008
Heling, S.   ~~WEIACC002~~
Hernandez-Garcia, C.   TUIACC001
Hoberg, H.-G.   ~~WEIACC002~~
Hoffstaetter, G.H.   **MOIDCC004**, ~~TUIBCC003~~, ~~TUICCC003~~, **WEIBCC001**, ~~THIBCC002~~, **FRIBCC003**
Honda, Y.   MOIACC002, **MOPSPP011**, ~~MOPSPP012~~, ~~WEICCC001~~
Hotei, T.   ~~THICCC001~~
Huang, S.   ~~WEIDCC001~~
Hug, F.   MOPSPP009, ~~TUIDCC005~~
Hulsart, R.L.   ~~WEIDCC002~~
Hutton, A.   ~~TUICCC002~~

— I —

Ice, L.   TUIACC001
Ihloff, E.   TUIACC001
Inacker, P.   WEICCC004, ~~WEIDCC002~~
Ingham, J.   ~~TUIBCC001~~

— J —

Jamilkowski, J.P.   WEICCC004, ~~WEIDCC002~~
Jankowiak, A.   **WEIACC002**
Jiang, Z.G.   **MOIACC003**
Jin, X.J.   MOPSPP012, ~~WEICCC001~~
Jing, Y.C.   WEIDCC002
Jones, L.B.   ~~MOPSPP017~~, **WEICCC002**
Jordan, K.   TUIACC001

— K —

Kaabi, W.   **WEIACC001**
Kako, E.   MOIACC002, ~~MOICCC003~~
Kalantarians, N.   TUIACC001
Kalus, C.   ~~WEIACC002~~
Kameta, Y.   MOPSPP012
Kamps, T.   ~~WEIACC002~~
Katagiri, H.   ~~MOICCC003~~
Kawasaki, T.   MOPSPP012
Kawata, H.   **MOIDCC001**, ~~TUIBCC004~~
Kayran, D.   **MOIDCC005**, **WEICCC004**, ~~WEIDCC002~~
Keith, C.   TUIACC001
Kellermann, R.   ~~WEIDCC002~~
Kelsey, J.   TUIACC001
Kewisch, J.   WEICCC004
Khan, A.   **MOPSPP001**, **THICCC002**
Klemz, G.   ~~WEIACC002~~
Klingbeil, H.   ~~MOPSPP002~~, THIBCC005
Knedel, J.   ~~WEIACC002~~
Kneisel, P.   MOPSPP003
Knobloch, J.   ~~WEIACC002~~
Knyazev, B.A.   MOIDCC002
Kobayashi, Y.   MOIACC002
Kohl, M.   TUIACC001
Kolbe, J.   ~~WEIACC002~~
Kolobanov, E.I.   MOIDCC002
Kondakov, A.A.   MOIDCC002
Konomi, T.   **MOIACC002**, ~~MOICCC003~~
Konoplev, I.V.   **TUIACC003**, FRIBCC005
Kourkafas, G.   ~~WEIACC002~~
Kozak, V.R.   MOIDCC002
Kozyrev, E.V.   MOIDCC002
Krutikhin, S.A.   MOIDCC002
Kubarev, V.V.   MOIDCC002, **TUIACC002**
Kühn, J.   **MOIBCC003**, ~~WEIACC002~~
Kürzeder, T.   MOIDCC006
Kulipanov, G.N.   MOIDCC002
Kuper, E.A.   MOIDCC002
Kuptsov, I.V.   MOIDCC002
Kuriki, M.   WEICCC001
Kurkin, G.Y.   MOIDCC002
Kuske, B.C.   ~~WEIACC002~~
Kuske, P.   ~~WEIACC002~~
Kuszynski, J.   ~~WEIACC002~~

— L —

Lambiase, R.F.	WEIDCC002
Lancaster, A.J.	TUIACC003
Laxdal, R.E.	**THICCC004**
Lösler, M.	MOIDCC006
Ledroit, B.	**MOPSPP007**
Lee, S.	TUIACC001
Legg, R.A.	TUIACC001
Lehn, D.	WEIDCC002
Li, R.	WEIBCC004
Li, X.D.	MOIACC003
Li, X.P.	**WEIACC004**
Li, Y.	TUIDCC004
Liaw, C.J.	WEICCC004
Liepe, M.	TUICCC003, THIBCC002
Lin, L.	WEIDCC001
Litvinenko, V.	WEIDCC002, **FRIACC003**
Liu, C.	WEIACC003, WEICCC004, WEIDCC002
Liu, K.X.	WEIDCC001
Liu, N.	MOICCC003
Liyanage, A.	TUIACC001
Lu, P.N.	MOPSPP003, WEIDCC003
Luce, M.	TUIBCC001

— M —

Mahler, G.J.	WEIDCC002
Malyutin, D.	WEIACC002
Mapes, M.	WEIDCC002
Marhauser, F.	**TUICCC002**
Matejcek, C.	MOPSPP006, **MOPSPP008**
Matsuda, R.	MOIACC002
Matsumoto, T.	MOICCC003
Matveenko, A.N.	WEIACC002
Mayes, C.E.	**TUIDCC003**, TUIDCC004
Müller, R.	WEIACC002
McAteer, M.	WEIACC002, **THIACC002**
McCaughan, M.D.	TUIACC001
McIntosh, P.A.	**FRIBCC005**
Medvedev, L.E.	MOIDCC002
Méot, F.	TUIDCC004, **WEIACC003**
Mernick, K.	WEICCC004, WEIDCC002
Meseck, A.	WEIACC002
Meshkov, O.I.	MOIDCC002
Metodiev, K.	TUIACC003
Metzger-Kraus, C.J.	WEIACC002
Michalski, T.J.	WEIACC003
Michizono, S.	MOIACC002, MOICCC003
Michnoff, R.J.	WEIDCC002
Mihara, K.	WEIDCC002
Militsyn, B.L.	MOPSPP017
Miller, T.A.	WEICCC004, WEIDCC002
Milner, R.	TUIACC001
Minty, M.G.	WEIACC003, WEICCC004, WEIDCC002
Mistry, S.	MOPSPP017

— M — (continued, right column)

Miura, T.	**MOICCC003**
Miyajima, T.	MOIACC002, MOPSPP011, MOPSPP012, WEICCC001, **THIACC001**, THICCC001
Montesinos, E.	**MOICCC001**
Moran, P.	TUIACC001
Motygin, S.V.	MOIDCC002
Murasev, A.A.	MOIDCC002
Murcek, P.	MOPSPP003, WEIDCC003

— N —

Nagai, R.	MOPSPP015, WEICCC001, THICCC003
Nakamura, N.	**TUIBCC002**, THICCC001
Narayan, G.	WEIDCC002
Nazeer, J.	TUIACC001
Neumann, A.	WEIACC002, **WEIDCC004**
Nishimori, N.	MOPSPP012, MOPSPP016, **MOPSPP015**, **WEICCC001**, **THICCC003**
Noakes, T.C.Q.	MOPSPP017

— O —

O'Connell, T.I.	TUICCC003
Obina, T.	MOPSPP011, MOPSPP012, WEICCC001
Ohm, N.	WEIACC002
Orfin, P.	WEIDCC002
Orth, S.	**MOPSPP002**, **THIBCC005**
Osaki, K.	THICCC001
Osipov, V.N.	MOIDCC002
Ott, K.	WEIACC002
Ovchar, V.K.	MOIDCC002

— P —

Palumbo, D.	TUIACC001
Paniccia, M.C.	WEIDCC002
Panofski, E.	WEIACC002
Park, H.	TUICCC002
Pei, S.	WEIACC004
Pellegrini, D.	**WEIBCC002**
Petrov, V.M.	MOIDCC002
Petrushina, I.	WEIDCC002
Pflocksch, F.	WEIACC002
Pforr, J.	MOIDCC006
Phillips, D.	WEIDCC002
Pietralla, N.	MOIDCC006
Pilan, A.M.	MOIDCC002
Pilling, M.J.	TUIBCC001
Pinayev, I.	**WEIDCC002**
Popik, V.M.	MOIDCC002
Ptitsyn, V.	**TUIDCC002**, WEIACC003, WEICCC004

List of Authors

— Q —

Qin, W.	WEIDCC001
Qiu, F.	MOICCC003
Quan, S.W.	WEIDCC001
Quigley, P.	TUICCC003, THIBCC002

— R —

Rahn, J.	WEIACC002
Randall, G.	TUIACC001
Rao, T.	**MOIBCC004**, WEICCC004, WEIDCC002
Repkov, V.V.	MOIDCC002
Robert-Demolaize, G.	WEIACC003
Roblin, Y.	WEIACC003
Roser, T.	WEIACC003, WEIDCC002
Ryukou, R.	MOPSPP011

— S —

Sabol, D.M.	TUICCC003
Sakai, H.	MOICCC003
Sakai, H.	MOIACC002
Salikova, T.V.	MOIDCC002
Sandberg, J.	WEICCC004
Satogata, T.	TUIACC001, WEIACC003
Saveliev, Y.M.	TUIBCC001
Sawamura, M.	MOICCC003, MOPSPP015, THICCC003
Schappert, W.	**THIBCC001**
Scheglov, M.A.	MOIDCC002
Schmeißer, M.	WEIACC002
Schüler, O.	WEIACC002
Schulte, D.	FRIBCC002
Schuster, M.	WEIACC002
Sears, J.	TUICCC003, THIBCC002
Seberg, S.K.	WEIDCC002
Sedlyarov, I.K.	MOIDCC002
Seletskiy, S.	WEICCC004
Serednyakov, S.S.	MOIDCC002
Seryi, A.	TUICCC003
Sheehy, B.	WEIDCC002
Shevchenko, O.A.	MOIDCC002
Shih, K.	WEIDCC002
Shimada, M.	MOPSPP011, **MOPSPP013**, THICCC001
Siggel-King, M.R.F.	TUIBCC001
Simon, D.	MOPSPP009
Skaritka, J.	WEIDCC002
Skrinsky, A.N.	MOIDCC002
Smart, L.	WEIDCC002
Smith, C.	TUIBCC001
Smith, E.N.	TUICCC003
Smith, K.S.	WEIDCC002
Smolenski, K.W.	**WEICCC003**
Soria, V.	WEIDCC002
Sorrell, Z.	WEIDCC002

Spata, M. F.	TUIACC001, WEIACC003
Steadman, S.	TUIACC001
Stocchi, A.	FRIBCC003
Stoll, C.P.	**MOPSPP009**
Surman, M.	TUIBCC001
Surrow, B.	TUIACC001
Sweat, L.	TUICCC002

— T —

Takai, R.	MOPSPP011
Tanaka, O.	**THICCC001**
Tararyshkin, S.V.	MOIDCC002
Tcheskidov, V.G.	MOIDCC002
Teichert, J.	**WEIDCC003**
Tennant, C.	**TUIACC001**, WEIACC003, **WEIBCC004**
Than, R.	WEIDCC002
Theisen, C.	WEIDCC002
Thieberger, P.	WEIACC003, WEICCC004, WEIDCC002
Thompson, N.	TUIBCC001
Thorpe, B.N.	TUIACC001
Tiefenback, M.G.	TUIACC001, WEIACC003
Trbojevic, D.	TUIDCC004
Tribendis, A.G.	MOIDCC002
Tsai, C.-Y.	WEIBCC004
Tschalär, C.	TUIACC001
Tsoupas, N.	TUIDCC004, WEIACC003
Tuozzolo, J.E.	WEICCC004, WEIDCC002
Turlington, L.	MOPSPP003

— U —

Uchiyama, T.	WEICCC001
Ullrich, J.	WEIACC002
Umemori, K.	MOIACC002, MOICCC003
Ushakov, A.	WEIACC002

— V —

Valizadeh, R.	MOPSPP017
Vennekate, H.	MOPSPP003, WEIDCC003
Veshcherevich, V.	TUICCC003, THIBCC002
Vidal, C.	TUIACC001
Vinokurov, N.A.	**MOIDCC002**
Vobly, P.	MOIDCC002
Völker, J.	WEIACC002
Volkov, V.	MOIDCC002

— W —

Walsh, J.	WEIDCC002
Wang, E.	WEICCC004, WEIDCC002, **FRIBCC001**
Wang, F.	WEIDCC001
Wang, G.	WEIDCC002
Wang, J.Q.	WEIACC004
Wang, Y.	TUIACC001

Weightman, P.	TUIBCC001
Weiss, D.	WEIDCC002
Williams, P.H.	**THIACC003**
Williams, R.L.	TUIBCC001
Wu, Q.	**MOICCC002**

— X —

Xiang, R.	MOPSPP003, WEIDCC003
Xiao, B. P.	WEIDCC002
Xie, H.M.	**WEIDCC001**
Xin, T.	WEIDCC002
Xu, C.	WEIACC003
Xu, J.Q.	WEIACC004
Xu, W.	WEIACC003, WEIDCC002

— Y —

Yamaguchi, S.	MOIACC002
Yamamoto, M.	MOIACC002, **MOPSPP012**, MOPSPP013, **MOPSPP016**, WEICCC001
Yamamoto, N.	MOPSPP011
Yanagisawa, T.	MOIACC002
Yokoya, K.	MOPSPP013

— Z —

Zaltsman, A.	WEIDCC002
Zhai, J.Y.	WEIACC004
Zhang, S.	TUIACC001, **FRIACC001**
Zhao, Z.	WEICCC004, WEIDCC002
Zhu, F.	WEIDCC001

List of Authors

Institutes List

Arizona State University
Tempe, USA

- Alarcon, R.
- Blyth, D.
- Dipert, R.A.
- Ice, L.
- Randall, G.
- Thorpe, B.N.

BINP SB RAS
Novosibirsk, Russia

- Borin, V.M.
- Davidyuk, I.V.
- Deichuli, O.I.
- Dementyev, E.N.
- Dovzhenko, B.A.
- Getmanov, Ya.V.
- Gorbachev, Ya.I.
- Knyazev, B.A.
- Kolobanov, E.I.
- Kondakov, A.A.
- Kozak, V.R.
- Kozyrev, E.V.
- Krutikhin, S.A.
- Kubarev, V.V.
- Kulipanov, G.N.
- Kuper, E.A.
- Kuptsov, I.V.
- Kurkin, G.Y.
- Medvedev, L.E.
- Meshkov, O.I.
- Motygin, S.V.
- Murasev, A.A.
- Osipov, V.N.
- Ovchar, V.K.
- Petrov, V.M.
- Pilan, A.M.
- Popik, V.M.
- Repkov, V.V.
- Salikova, T.V.
- Scheglov, M.A.
- Sedlyarov, I.K.
- Serednyakov, S.S.
- Shevchenko, O.A.
- Skrinsky, A.N.
- Tararyshkin, S.V.
- Tcheskidov, V.G.
- Tribendis, A.G.
- Vinokurov, N.A.
- Vobly, P.
- Volkov, V.

BINP
Novosibirsk, Russia

- Dorokhov, V.L.

BNL
Upton, Long Island, New York, USA

- Altinbas, Z.
- Belomestnykh, S.A.
- Ben-Zvi, I.
- Berg, J.S.
- Brooks, S.J.
- Brown, K.A.
- Bruno, D.
- Brutus, J.C.B.
- Costanzo, M.R.
- Curcio, A.J.
- DeSanto, L.
- Di Lieto, A.
- Fedotov, A.V.
- Folz, C.
- Gassner, D.M.
- Gu, X.
- Hammons, L.R.
- Hao, Y.
- Harvey, M.
- Hayes, T.
- Hulsart, R.L.
- Inacker, P.
- Jamilkowski, J.P.
- Jing, Y.C.
- Kayran, D.
- Kellermann, R.
- Kewisch, J.
- Lambiase, R.F.
- Lehn, D.
- Liaw, C.J.
- Litvinenko, V.
- Liu, C.
- Mahler, G.J.
- Mapes, M.
- Méot, F.
- Mernick, K.
- Michnoff, R.J.
- Miller, T.A.
- Minty, M.G.
- Narayan, G.
- Orfin, P.
- Paniccia, M.C.
- Phillips, D.
- Pinayev, I.
- Ptitsyn, V.
- Rao, T.
- Robert-Demolaize, G.
- Roser, T.
- Sandberg, J.
- Seberg, S.K.
- Seletskiy, S.
- Sheehy, B.
- Skaritka, J.
- Smart, L.
- Smith, K.S.
- Soria, V.
- Sorrell, Z.
- Than, R.

- Theisen, C.
- Thieberger, P.
- Trbojevic, D.
- Tsoupas, N.
- Tuozzolo, J.E.
- Walsh, J.
- Wang, E.
- Wang, G.
- Weiss, D.
- Wu, Q.
- Xiao, B. P.
- Xin, T.
- Xu, C.
- Xu, W.
- Zaltsman, A.
- Zhao, Z.

CEA/DRF/IRFU
Gif-sur-Yvette, France
- Garçon, M.

CERN
Geneva, Switzerland
- Aull, S.
- Gerigk, F.
- Montesinos, E.
- Pellegrini, D.
- Schulte, D.

CNR-ISM
Trieste, Italy
- Luce, M.

Cockcroft Institute, Lancaster University
Lancaster, United Kingdom
- Burt, G.

Cornell University (CLASSE), Cornell Laboratory for Accelerator-Based Sciences and Education
Ithaca, New York, USA
- Banerjee, N.
- Bazarov, I.V.
- Crittenden, J.A.
- Dobbins, J.
- Eichhorn, R.G.
- Furuta, F.
- Ge, M.
- Hoffstaetter, G.H.
- Li, Y.
- Liepe, M.
- Mayes, C.E.
- O'Connell, T.I.
- Quigley, P.
- Sabol, D.M.
- Sears, J.
- Smith, E.N.
- Smolenski, K.W.
- Veshcherevich, V.

e-JAPAN IT Co. Ltd
Hitachi, Japan
- Kameta, Y.

Fermilab
Batavia, Illinois, USA
- Ainsworth, R.
- Checchin, M.
- Schappert, W.

Frankfurt University of Applied Sciences
Frankfurt am Main, Germany
- Eschelbach, C.
- Lösler, M.

Hampton University
Hampton, Virginia, USA
- Cao, T.
- Dongwi, B.
- Guèye, P.
- Kalantarians, N.
- Kohl, M.
- Liyanage, A.
- Nazeer, J.

HIM
Mainz, Germany
- Aulenbacher, K.
- Kürzeder, T.

HU/AdSM
Higashi-Hiroshima, Japan
- Kuriki, M.

HZB
Berlin, Germany
- Abo-Bakr, M.
- Anders, W.
- Bürkmann-Gehrlein, K.B.
- Büchel, A.B.
- Echevarria, P.
- Frahm, A.
- Glock, H.-W.
- Glöckner, F.
- Göbel, F.
- Hall, B.D.S.
- Heling, S.
- Hoberg, H.-G.
- Jankowiak, A.
- Kalus, C.
- Kamps, T.
- Klemz, G.
- Knedel, J.
- Knobloch, J.
- Kolbe, J.
- Kourkafas, G.

Institutes List

- Kühn, J.
- Kuske, B.C.
- Kuske, P.
- Kuszynski, J.
- Malyutin, D.
- Matveenko, A.N.
- McAteer, M.
- Meseck, A.
- Metzger-Kraus, C.J.
- Müller, R.
- Neumann, A.
- Ohm, N.
- Ott, K.
- Panofski, E.
- Pflocksch, F.
- Rahn, J.
- Schmeißer, M.
- Schüler, O.
- Schuster, M.
- Ullrich, J.
- Ushakov, A.
- Völker, J.

HZDR
Dresden, Germany
- Arnold, A.
- Evtushenko, P.E.
- Freitag, M.
- Lu, P.N.
- Murcek, P.
- Teichert, J.
- Vennekate, H.
- Xiang, R.

IHEP
Beijing, People's Republic of China
- Chi, Y.L.
- Li, X.P.
- Pei, S.
- Wang, J.Q.
- Zhai, J.Y.

IKP
Mainz, Germany
- Aulenbacher, K.
- Bechthold, V.
- Dehn, M.A.
- Fichtner, F.
- Friederich, S.
- Hein, L.M.
- Hug, F.
- Ledroit, B.
- Matejcek, C.
- Simon, D.
- Stoll, C.P.

Insititue of High Energy Physics (IHEP)
People's Republic of China

- Xu, J.Q.

Institut Theorie Elektromagnetischer Felder, TU Darmstadt
Darmstadt, Germany
- Boine-Frankenheim, O.
- Khan, A.

ISM-CNR
Rome, Italy
- Cricenti, A.

JAI
Oxford, United Kingdom
- Konoplev, I.V.
- Lancaster, A.J.
- Metodiev, K.
- Seryi, A.

JLab
Newport News, Virginia, USA
- Benson, S.V.
- Bevins, M.E.
- Bogacz, S.A.
- Boyce, J.R.
- Ciovati, G.
- Coleman, J.L.
- Douglas, D.
- Dubbé, C.J.
- Frierson, S.L.
- Gubeli, J.
- Hernandez-Garcia, C.
- Hutton, A.
- Jordan, K.
- Keith, C.
- Kneisel, P.
- Legg, R.A.
- Li, R.
- Marhauser, F.
- McCaughan, M.D.
- Michalski, T.J.
- Roblin, Y.
- Satogata, T.
- Spata, M. F.
- Tennant, C.
- Tiefenback, M.G.
- Turlington, L.
- Zhang, S.

KEK
Ibaraki, Japan
- Arakawa, D.A.
- Aryshev, A.
- Egi, M.
- Enami, K.
- Furuya, T.
- Honda, Y.
- Jin, X.J.

- Kako, E.
- Katagiri, H.
- Kawata, H.
- Kobayashi, Y.
- Konomi, T.
- Matsumoto, T.
- Michizono, S.
- Miura, T.
- Miyajima, T.
- Nakamura, N.
- Obina, T.
- Qiu, F.
- Ryukou, R.
- Sakai, H.
- Shimada, M.
- Takai, R.
- Tanaka, O.
- Uchiyama, T.
- Umemori, K.
- Yamaguchi, S.
- Yamamoto, M.
- Yamamoto, N.
- Yokoya, K.

LAL
Orsay, France
- Kaabi, W.
- Stocchi, A.

MHI-MS
Kobe, Japan
- Yanagisawa, T.

MIB
Manchester, United Kingdom
- Gardner, P.
- Pilling, M.J.

Mitsubishi Heavy Industries Ltd. (MHI)
Takasago, Japan
- Matsuda, R.

MIT
Cambridge, Massachusetts, USA
- Balewski, J.
- Bernauer, J.C.
- Bessuille, J.C.
- Corliss, R.
- Cowan, R.F.
- Epstein, C.
- Fisher, P.F.
- Friščić, I.
- Hasell, D.K.
- Ihloff, E.
- Kelsey, J.
- Lee, S.
- Milner, R.

- Moran, P.
- Palumbo, D.
- Steadman, S.
- Tschalär, C.
- Vidal, C.
- Wang, Y.

NSTU
Novosibirsk, Russia
- Tribendis, A.G.

NSU
Novosibirsk, Russia
- Davidyuk, I.V.
- Getmanov, Ya.V.
- Knyazev, B.A.
- Kozyrev, E.V.
- Serednyakov, S.S.
- Vinokurov, N.A.

ODU
Norfolk, Virginia, USA
- De Silva, S.U.
- Delayen, J.R.
- Park, H.
- Sweat, L.

PKU
Beijing, People's Republic of China
- Cheng, W.
- Feng, L.W.
- Hao, J.K.
- Huang, S.
- Lin, L.
- Liu, K.X.
- Qin, W.
- Quan, S.W.
- Wang, F.
- Xie, H.M.
- Zhu, F.

QST
Tokai, Japan
- Hajima, R.
- Nagai, R.
- Nishimori, N.
- Sawamura, M.

SBU
Stony Brook, New York, USA
- Shih, K.

SINAP
Shanghai, People's Republic of China
- Gu, Q.
- Jiang, Z.G.
- Li, X.D.

Institutes List

SLAC
Menlo Park, California, USA
- Gonnella, D.
- Tsai, C.-Y.

Sokendai
Ibaraki, Japan
- Hotei, T.
- Liu, N.

STFC/DL/ASTeC
Daresbury, Warrington, Cheshire, United Kingdom
- Beaver, T.S.
- Dunning, D.J.
- Jones, L.B.
- McIntosh, P.A.
- Militsyn, B.L.
- Noakes, T.C.Q.
- Saveliev, Y.M.
- Thompson, N.
- Valizadeh, R.
- Williams, P.H.

STFC/DL/SRD
Warrington, Cheshire, United Kingdom
- Surman, M.

STFC/DL
Daresbury, Warrington, Cheshire, United Kingdom
- Mistry, S.

Stony Brook University
Stony Brook, USA
- Cervantes, R.
- Deshpande, A.
- Feege, N.
- Mihara, K.

SUNY SB
Stony Brook, New York, USA
- Dehmelt, K.
- Petrushina, I.

TEMF, TU Darmstadt
Darmstadt, Germany
- Domont-Yankulova, D.
- Klingbeil, H.
- Orth, S.

Temple University
Philadelphia, USA
- Surrow, B.

The University of Liverpool
Liverpool, United Kingdom
- Craig, T.
- Harrison, P.
- Ingham, J.
- Siggel-King, M.R.F.
- Smith, C.
- Weightman, P.

Tohoku University, Research Center for Electron Photon Science
Sendai, Japan
- Nishimori, N.

Toshiba
Yokohama, Japan
- Kawasaki, T.
- Osaki, K.

TRIUMF
Vancouver, Canada
- Laxdal, R.E.

TU Darmstadt
Darmstadt, Germany
- Arnold, M.
- Burandt, C.
- Pforr, J.
- Pietralla, N.

University of Liverpool
Liverpool, United Kingdom
- Williams, R.L.